ADVANCED FUNCTIONAL MATERIALS
www.afm-journal.de

Ferromagnetic Elements in Two-Dimensional Materials: 2D Magnets and Beyond

Anastasios V. Papavasileiou, Melita Menelaou, Kalyan J. Sarkar, Zdenek Sofer, Lakshminarayana Polavarapu,* and Stefanos Mourdikoudis**

Ferromagnetism in 2D materials has attracted tremendous interest from the scientific community thanks to its potential for the design of magnetic materials with unique properties. The presence of a ferromagnetic element in a 2D material can improve the existing properties and offer new ones, giving rise to the development of manifold applications. This review focuses on recent advances and perspectives of 2D materials that bear at least one ferromagnetic element (iron, cobalt, nickel) as i) structural constituent, ii) dopant atom, or iii) adjacent atom through proximity effect. By describing in detail the magnetic properties that have emerged so far, their potential to form next-generation 2D magnets is discussed. Moreover, the contribution of such 2D materials is analyzed in various applications (electrochemical, photochemical, optical, and electronic), aiming to explore further functionalities and capabilities of ferromagnetic elements, apart from their magnetic nature. Special attention is given to gadolinium and other rare earth elements that display a ferromagnetic order even at ultra-low temperatures and form part of 2D structured materials, with particularly appealing properties deriving from their 4f electrons.

1. Introduction

In the effort to discover new and enhanced properties in materials science, 2D materials have been drawing a large interest.[1] Their unique shape and high surface area enable them to possess attractive physical and chemical properties.[2] For instance, the unprecedented properties of graphene inspired further investigation toward novel 2D materials aiming for equivalent or even better performance.[3,4] Anisotropy, in combination with low thickness, bestows excellent mechanical, electrical, optical, and chemical properties on 2D materials outshining their 3D counterparts.[5] Thanks to these qualities, 2D materials hold great potential for the development of novel applications associated with energy storage,[6,7] catalysis,[8] electrocatalytic[9,10] and photocatalytic[11] water splitting, drug delivery,[12,13] nanomedicine,[14] electroanalysis[15] and sensing.[16]

The concomitant discovery of CrI_3[17] and $Cr_2Ge_2Te_6$[18] in 2017 as the first 2D materials exhibiting ferromagnetism paved the way for the exploration of magnetic properties in low dimensionality and allowed its full exploitation in spintronics.[19] Spintronics is a technology that takes advantage of the spin and charge of a single electron and nowadays it has become increasingly popular in memory, logic, and optoelectronic devices.[20] 2D materials are ideal candidates for spintronics due to the highly homogeneous atomic control over their thickness that facilitates spin manipulation.[21,22] Furthermore, they can

A. V. Papavasileiou, K. J. Sarkar, Z. Sofer, S. Mourdikoudis
Department of Inorganic Chemistry
University of Chemistry and Technology Prague
Technicka 5, Prague 6 16628, Czech Republic
E-mail: soferz@vscht.cz; mourdikt@vscht.cz

M. Menelaou
Department of Chemical Engineering
Faculty of Geotechnical Sciences and Environmental Management
Cyprus University of Technology
Limassol 3036, Cyprus

L. Polavarapu
CINBIO
Universidade de Vigo
Materials Chemistry and Physics
Department of Physical Chemistry
Campus Universitario Lagoas Marcosende
Vigo 36310, Spain
E-mail: lakshmi@uvigo.es

S. Mourdikoudis
Separation and Conversion Technology
Flemish Institute for Technological Research (VITO)
Boeretang 200, Mol 2400, Belgium

The ORCID identification number(s) for the author(s) of this article can be found under https://doi.org/10.1002/adfm.202309046

DOI: 10.1002/adfm.202309046

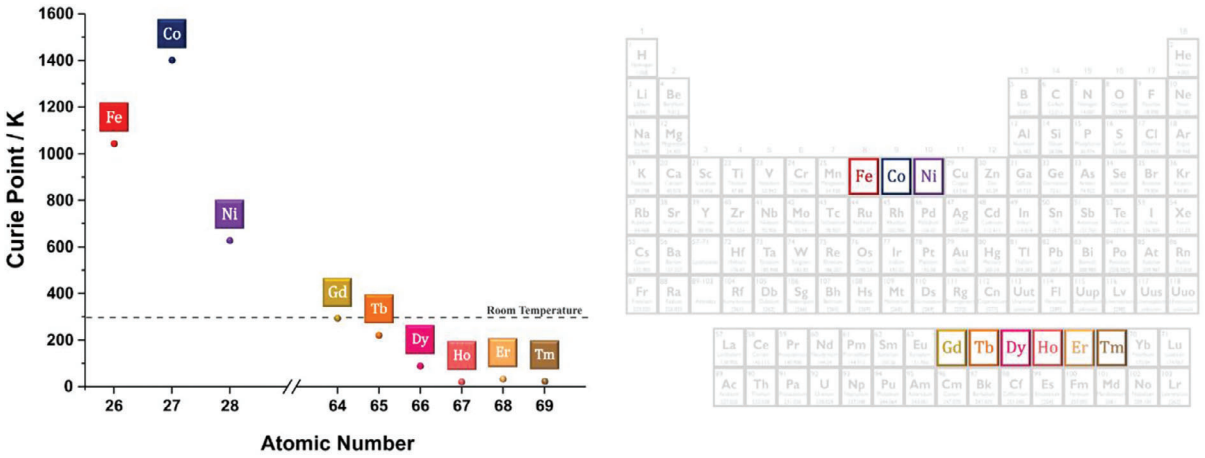

Figure 1. Chemical elements exhibiting ferromagnetic order classified based on their atomic number and their Curie point (left) and the periodic table highlighting the elements with ferromagnetic behavior (right).

combine ferromagnetic and semiconducting properties, which are coveted and concurrently elusive abilities because of the crystal structure and chemical bonding differences.[23]

During the last decade, several groups found out that magnetic features can be altered in reduced dimensionality. Materials of 2D do not necessarily inherit the magnetic properties of their bulk counterparts; thus, the magnetic order of a certain bulk pristine material does not guarantee its presence in the 2D limit.[24] Accordingly, the Curie point (T_C) of a 2D material is usually lower than that of its bulk form, and as the material becomes thinner, the T_C normally decreases.[25,26] Even so, it is possible to obtain a ferromagnetic 2D material from a paramagnetic bulk pristine material.[27]

Up to date, numerous research endeavors have attempted to induce ferromagnetism or improve the existing magnetic properties in 2D materials. However, most of them rely on defect engineering,[28] surface functionalization,[29] doping,[30] or alloying,[31] which are either tentative or rather inappropriate solutions as they cannot ensure the presence of long-range ferromagnetic order without affecting other essential properties, such as conductivity.[32,33] Therefore, it is of immense interest to produce 2D materials with intrinsic magnetic properties with the desired characteristics.[34] Most newly discovered 2D magnets exhibit inherent ferromagnetic order only at low temperatures, which is a limiting parameter for their integration into future technologies. As a result, finding 2D ferromagnetic materials with a T_C above room temperature remains a cumbersome challenge.[35] Surprisingly, in most cases, these 2D ferromagnets do not contain any of the known ferromagnetic elements (Fe, Co, Ni, Gd).[18,27,36,37] Nevertheless, a number of studies suggest that ferromagnetic elements can boost the T_C, contribute to the magnetic moment, and favor the exchange interactions in the crystal lattice of the material.[38] After all, it is fairly established that all commercial permanent magnets have at least one ferromagnetic element in their structure.[39]

It is well known that iron, cobalt, and nickel display ferromagnetic order in temperatures much higher than room temperature; therefore, they are established as the standard ferromagnetic elements of the periodic table.[40] However, other elements can exhibit ferromagnetic order as well, exclusively at lower temperatures dictated by their Curie point (**Figure 1**). In particular, gadolinium with a near room temperature Curie point, followed by other rare earth elements, namely terbium, dysprosium, erbium, holmium, and thulium with much lower Curie points, exhibit ferromagnetic ordering in certain temperature ranges.[41–43] Apart from their magnetic properties that make them noteworthy, each one of the above-mentioned elements has a unique electron configuration and can form compounds with different behaviors and materials of various morphologies for diverse applications.[44,45] The presence of these elements in a variety of coordination compounds and oxides is already known, but they also form part of 2D materials either as a main component or as a dopant: in this manner, they are able to affect the properties of the resulting material as well as endow it with new ones.[46,47]

The topic of 2D ferromagnetism has been extensively studied and revisited after discovering the aforementioned 2D ferromagnetic materials. However, reports on the potential of 2D materials based on ferromagnetic elements to generate 2D ferromagnets with even better magnetic properties are scarce. Thus, it is timely to investigate their magnetic and other types of properties as well as their potential to form next-generation 2D magnets. In this way, such materials will be strong candidates for use in numerous application fields. This review focuses on the impact of the presence of ferromagnetic elements in 2D materials and their role as i) structural constituents, ii) dopants, or iii) adjacent atoms (**Figure 2**), aiming to explore the range of versatile characteristics that the ferromagnetic elements can offer, apart from their magnetic properties. Special attention is given to 2D materials incorporating gadolinium and other ferromagnetic rare earth elements, whilst examples of non-ferromagnetic rare earth elements are also presented for the sake of completion.

2. Two-Dimensional Ferromagnets

The discovery of ferromagnetic order in two-dimensional materials called into question the Mermin-Wagner theorem,[48] which dictates the lack of magnetic order in two dimensions due to thermal fluctuations under the isotropic Heisenberg model.[49]

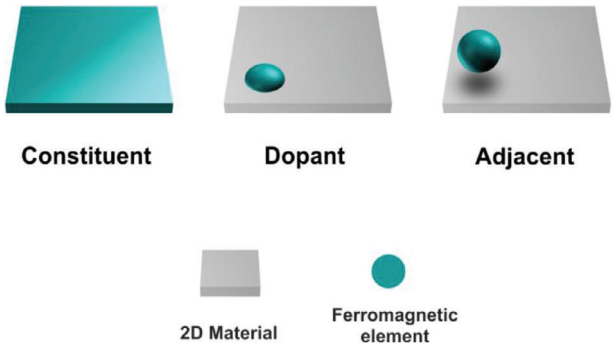

Figure 2. The mode of the presence of a ferromagnetic element in a 2D material.

At the same time, certain theories support that exchange interaction alone is not sufficient to provide magnetic order.[50] However, magnetic anisotropy lifts those restrictions by allowing spin-orbit coupling (SOC) interaction in a 2D Ising model and unlocks the possibility of discovering a broader number of 2D magnets with enhanced properties.[51,52] This highlights the complexity of the 2D systems and emphasizes the influence of thermal fluctuations in the spin dimensionality and, thus, its magnetic long-range order.

The dimensionality of the spin (n) is determined by physical parameters such as the presence and strength of magnetic anisotropy and it is described by three different models i) the Ising model for n = 1, ii) the XY model for n = 2, and iii) the isotropic Heisenberg model for n = 3. A visual representation of the models is shown in **Figure 3**, where it is clear that the Ising model has a strong uniaxial anisotropy, the XY model has an easy-plane anisotropy, while the isotropic Heisenberg model has no constrain on the spin direction.[34]

So far, a handful of 2D materials own an intrinsic ferromagnetic order. Many of them have a van der Waals (vdW) structure and are often acquired through mechanical exfoliation.[17,18,25,53,54] Several studies support that ferromagnetic order depends on the thickness of the material;[17] the Curie point is highly dependent on the thickness and the number of layers of a given material. **Figure 4** demonstrates the correlation between the number of layers and T_C for some of the newly discovered 2D ferromagnets. Based on the behavior of the T_C as a function of the layer number, we can highlight three different trends for three different classes of materials: i) chromium trihalides ($CrCl_3$, $CrBr_3$, CrI_3) – these materials possess a very low T_C in the 2D scale, which is slightly higher in their bulk form,

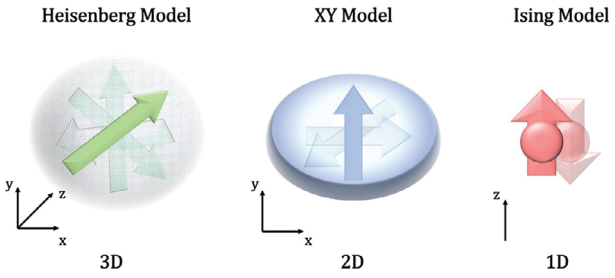

Figure 3. Schematic illustration of the spin dimensionality models.

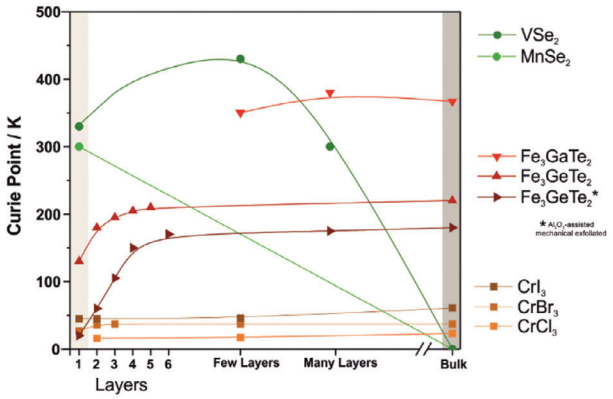

Figure 4. Curie point dependence of layer number for newly discovered 2D ferromagnets. Data obtained from literature as follows: VSe_2,[54] $MnSe_2$,[36] Fe_3GaTe_2,[56] Fe_3GeTe_2 (mechanically exfoliated, assisted by SiO_2/Si[53] or Al_2O_3[25]), and CrI_3, $CrBr_3$, $CrCl_3$.[55]

without reaching room temperature in any case;[55] ii) iron-based transition metal tellurides (Fe_3GeTe_2, Fe_3GaTe_2) – they exhibit a small increase in the Curie point from the bulk to multi-layer structures and then a decrease to the monolayer.[25,53,56] Interestingly, Fe_3GeTe_2 crystals which underwent mechanical exfoliation assisted by Al_2O_3,[25] exhibited lower T_C in their 2D form compared to a SiO_2/Si-assisted exfoliated Fe_3GeTe_2[53] but they kept following the same trend. Finally, iii) transition metal selenides ($MnSe_2$ and VSe_2), contrary to most 2D ferromagnets that derive their magnetic properties from their bulk crystals, exhibit room temperature ferromagnetism in low dimensionality even though their bulk crystals are not ferromagnetic.[27,36,54] In particular, ultrathin 2D VSe_2 is an unprecedented example of a 2D material with room-temperature intrinsic ferromagnetism, despite the fact that its pristine bulk material is paramagnetic. In that case, the origin of the magnetic properties is attributed to the magnetic anisotropy arising from the structural inversion symmetry.[27,54]

The discovery of room-temperature ferromagnetic properties in the 2D scale is a crucial and demanding task, while achieving and maintaining ferromagnetism in monolayered 2D materials poses an even greater complexity. On top of that, monolayered materials often lack air stability due to their high reactivity.[54,57] The combination of low Curie points along with their instability in air, limits the suitability of these materials in practical applications. Therefore, the synthesis of new ultrathin 2D ferromagnets with intrinsic ferromagnetic order at room temperature and good stability in environmental conditions is of paramount importance.[19]

It is well known that ferromagnetic elements contribute to the increase of Curie point in the materials they constitute.[38] Even so, only a few 2D magnets contain at least one ferromagnetic element in their chemical structure.[25,38,53,56,58]

The most studied 2D material based on a ferromagnetic element exhibiting intrinsic ferromagnetism is Fe_3GeTe_2. Zhuang et al. predicted the inherent ferromagnetic order in monolayered Fe_3GeTe_2, along with a significant uniaxial magnetocrystalline anisotropy originating from spin orbit-coupling. Furthermore, DFT (Density Functional Theory) calculations revealed that Fe 3d orbitals dominate the band structure around the Fermi

level leading to Stoner criterion fulfillment and, thus, to itinerant ferromagnetism.[59] Liu et al. grew Fe_3GeTe_2 thin films by molecular beam epitaxy and managed to control the thickness of the film through in-situ reflection high-energy electron diffraction (RHEED) oscillations. In an attempt to tailor the magnetic properties of Fe_3GeTe_2 films, they studied the impact of Fe composition on the Curie point and revealed that with increasing Fe composition, the T_C rises significantly.[38]

Based on the above-mentioned theoretical calculations and experimental results, Fe presence is a critical parameter not only for fulfilling the Stoner criterion and possessing itinerant ferromagnetism but also for achieving a higher Curie point that will allow Fe_3GeTe_2 thin films to be applicable in different domains.

In addition, Fe_3GeTe_2 exhibited an interesting correlation between the number of layers and its ferromagnetic properties: more specifically, Fei et al. mechanically exfoliated bulk Fe_3GeTe_2 down to monolayer and observed a decline of T_C from 207 to 130 K. Reflective magnetic circular dichroism (RMCD) studies on the dependence of the T_C on the number of layers (flakes up to five layers) illustrated the monotonic decrease of T_C from 3D to 2D, with the T_C of the four and five layered material being very close to the bulk. Additionally, the hysteresis behavior of an atomically thin Fe_3GeTe_2 flake (3.2 nm) revealed single-domain, highly anisotropic out-of-plane ferromagnetic order at all temperatures below its T_C, while a much thicker flake (48 nm) behaved differently, as it loses its hysteresis at an intermediate temperature and not at the T_C as expected.[53] Deng et al. developed an Al_2O_3-assisted mechanical exfoliation method to facilitate the isolation of monolayers out of bulk Fe_3GeTe_2. This exfoliation method led to more stable monolayers but with a T_C lower than 50 K, which was much lower than the one reported by Fei et al.; the T_C dependence on the thickness was analogous. Deng et al. in their study took advantage of the tunability of the monolayered Fe_3GeTe_2 and via the use of an ionic gate, managed to boost T_C to reach room temperature.[25]

Fe_3GeTe_2 holds many promising properties like i) metallic nature, ii) air stability, iii) relatively high T_C, and iv) high uniaxial magnetocrystalline anisotropy and its magnetic properties can be manipulated by i) altering the Fe composition, ii) proximity with an antiferromagnetic substrate (MnTe), iii) gate tunneling and iv) adjusting the number of layers. These characteristics render Fe_3GeTe_2 the chameleon of 2D ferromagnets and make it an ideal candidate for the development of spintronic devices with high accuracy and efficiency.[25,53]

Nonetheless, there are analogous structural materials with intriguing properties belonging to the Fe_nGeTe_2 series. The study of the Fe_nGeTe_2 can reveal the role of Fe and how its stoichiometry affects the magnetic properties of the materials. Mondal et al. synthesized Fe_4GeTe_2 single crystals via the chemical transport method by adding a relative excess of Fe precursor. Fe_4GeTe_2 has a T_C at 270 K, while at 120 K, a spin-reorientation phenomenon occurs, leading to larger out-of-plane magnetization than the in-plane-magnetization. The magnetic behavior of Fe_4GeTe_2 is isotropic with a small magnetic anisotropy, which makes the Ising model not feasible, while the dimensionality of the magnetic network is less than 3D: this leads to a magnetism of a quasi-2D nature and exchange interactions. Further, the Rhodes-Wohlfarth ratio (RWR) was found to be 2.53, which is lower than Fe_3GeTe_2, and this evidences that the itinerant character of the Fe_nGeTe_2 system is suppressed with the increase in Fe concentration. At the same time, Fe_4GeTe_2 shows a 3 times smaller uniaxial magnetic anisotropy than Fe_3GeTe_2, highlighting the detrimental role of Fe in the magnetic exchange mechanism and its nature.[60] Similarly, Li et al. studied Fe_5GeTe_2 synthesized via chemical vapor transport and reported a T_C of 273 K with a weak magnetic anisotropy. The dimensionality of the spin (n) and the model applied in this material was estimated to be between the 3D Heisenberg model (n = 3) and the XY model (n = 2).[61]

Even though Fe atoms are the source of ferromagnetism in these materials, the combining elements and the exchange interactions with Fe are crucial for several magnetic properties. Gallium is another element that can participate in iron-based transition metal tellurides. Zhang et al. synthesized Fe_3GaTe_2 via a self-flux method involving mechanical exfoliation and reported on intrinsic ferromagnetism with Curie point reaching 350 K in the 2D limit, together with a robust perpendicular magnetic anisotropy (PMA). The authors also demonstrated that T_C depends on the thickness; from 380 K in a 112 nm (multi-layer) nanosheet, T_C decreases to 350 K in a 9.5 nm (few-layer) nanosheet. Even so, the few-layer nanosheet possesses a 3.2 times higher coercive field (H_c) than the multi-layer nanosheet. Moreover, Fe_3GaTe_2 exhibited different types of magnetic domains as a function of their thickness; thicker nanosheets have a multi-stripe domain structure, while the thinner ones (up to 28 nm) possess a single domain structure.[56]

Generally, ferromagnetism in low dimensionality is a quite intricate topic and involves various parameters. The properties of a 2D material are greatly affected by temperature conditions and thermal fluctuations. Curie point dictates the behavior of every material and can be modulated by modifying i) the thickness, ii) the magnetic element composition, ii) the structural or morphological characteristics, and iv) the preparation method of the material. Altering any of these parameters can cause a pronounced effect on the rest of them. For instance, preparation methods play a significant role in determining material thickness, with bottom-up methods offering better control aiming for thinner materials, whereas top-down approaches often lead to thicker structures with varying amounts of defects. So far, mechanical exfoliation has been one of the most commonly used top-down methods for fabrication of ferromagnetic 2D materials. Nevertheless, applying mechanical exfoliation on the same pristine material under different experimental conditions cannot ensure identical magnetic behaviors, even if the resulting materials have the same thickness.

3. 2D Materials Based On Ferromagnetic Elements

In this section, we chose to classify the 2D materials that include a ferromagnetic element in their structure according to the different types of the destined applications: in this way, we aim to highlight the influence of ferromagnetic constituents on material characteristics and, subsequently, their impact on the efficiency of the respective applications. Additionally, structural characteristics of representative materials are demonstrated in **Figure 5** while the performance of the discussed materials is presented in the **Table 1** at the end of section 3 according to the destined application.

Table 1. Summarization of the use and performance of 2D materials based on ferromagnetic elements in manifold applications.

Molecular type	Morphology	Application	Performance	Reference
		Spintronics		
Fe_3GeTe_2	Thin flakes	Spin-orbit torque	Magnetization switch at 2.5×10^{11} A m^{-2} current density at 180 K	[64]
Fe_3GeTe_2	Thin flakes	Magnetic tunnel junction	MR 41% under applied bias of 0.1 μA at 10 K	[70]
Fe_3GaTe_2	Thin flakes	Magnetic tunnel junction	TMR ratio up to 213% with a spin polarization of 72% at 10 K	[75]
		Electrocatalysis	$\eta 10^*$ [mV] (Tafel slope [mV dec^{-1}]) / electrolyte	
Fe_3GeTe_2	Nanosheets	HER	590 (109.0) / 0.5 M H_2SO_4	[110]
		HER	630 (174.5) / 1.0 M KOH	
		OER	1110 (296.5) / 1.0 M KOH	
Ni_3GeTe_2	Nanosheets	HER	490 (75.6) / 0.5 M H_2SO_4	[110]
		HER	780 (147.5) / 1.0 M KOH	
		OER	1090 (330.4) / 1.0 M KOH	
Ni-BDC/Fe_3O_4	Nanosheets	OER	295 (47.8) / 1.0 M KOH	[111]
Ni-BDC/$Ni(OH)_2$	Nanosheets	OER	320 (41.0) / 1.0 M KOH	[112]
FePc@2D Ni-MOF	Nanosheets	HER	334 (72.1) / 1.0 M KOH	[113]
CoP/Co-BDC	Nanosheets	HER	52 (49.0) / 0.5 M H_2SO_4	[115]
		HER	26 (53.0) / 1.0 M KOH	
$NiCoP_xS_y$	Nanosheets	HER	61 (44.5) / 1.0 M KOH	[116]
$NiFeP_xS_y$	Nanosheets	OER	242 (38.0) / 1.0 M KOH	[116]
$NiCoP_xS_y$/$NiFeP_xS_y$		OWS*	1540 / 1.0 M KOH	[116]
CoS_2/CC	Nanosheets	HER	90 (48.0) / 1.0 M KOH	[117]
		OER	220 (92.0) / 1.0 M KOH	
		OWS	1580 / 1.0 M KOH	
FeCoNiP@C/NF	Nanosheets	HER	71 (75.4) / 1.0 M KOH	[94]
		OER	227 at 100 mA cm^{-2} (85.6) / 1.0 M KOH	
		OWS	1600 at 100 mA cm^{-2} / 1.0 M KOH	
Benchmark Catalysts				
Pt/C 20 wt%		HER	35 (30.0) / 1.0 M KOH	[117]
IrO_2		OER	300 (53.0) / 1.0 M KOH	[117]
		Sensing	Detection range [μM] (LOD [μM])/ Sample	
BNPNS	Nanosheets	H_2O_2	0.05 – 100 / living cells	[123]
NiCoP/GF	Nanosheets	H_2O_2	0.2-1.8, 1.8-10.8, 10.8-9330 (0.028) / B6 melanoma cells	[124]
VCo-$Co(OH)_2$	Nanosheets	Glucose	0.4 – 8230 (0.295) / blood serum	[125]
		L-cysteine	0.2 – 1940 (0.0765)/ blood serum	
2D NiCo phosphate	Nanosheets	Glucose	2-4470 (0.4) / human serum	[126]
CoSe/Ni_3B	Nanosheets	5-Nitroquinoline	0.2-378 (0.042)/ aquatic	[127]
FeS	Nanoflakes	Hg (II)	0.01-10 (0.004) / aquatic	[128]
Ni-MOF	Nanosheets	Ni (II)	10-10^5 (2.7) / saliva, sweat, aquatic	[129]
		Energy Storage	Specific capacity [mA h g^{-1}]	
Co_2GeO	Hexagonal nanosheets	Li-ion battery	1026 at 0.22 A g^{-1}	[130]
$FePS_3$	Nanosheets	Li-ion batt./	1046 at 0.05 A g^{-1}/	
		Na-ion batt.	754 at 0.05 A g^{-1}	
$CoPS_3$	Nanosheets	Li-ion batt.	1086 at 0.05 A g^{-1}	
		Na-ion batt.	846 at 0.05 A g^{-1}	
$NiPS_3$	Nanosheets	Li-ion batt.	1026 at 0.05 A g^{-1}	[131]
		Na-ion batt.	910 at 0.05 A g^{-1}	

(*Continued*)

Table 1. (Continued).

		Energy Storage	Specific capacity [mA h g^{-1}]	
α-$Ni(OH)_2$ /rGO	Nanosheets	Energy storage/supercapacitor	2220 F g^{-1} at 3.2 A g^{-1}	[132]
Ni-BDC	Nanosheets	Batter.-supercap. or hybrid	(Power density: 55.8 W h kg^{-1})	[133]
		Photocatalysis	Performance rate [mmol g^{-1} h^{-1}]	
RuNi/g-C_3N_4	Nanosheets	H_2 evolution	35.1	[137]
Ni-BDC	Nanosheets	CO_2 reduction	104	[140]
ZnCo-BMOF	Nanosheets	CO_2 reduction	0.130	[143]
		EW Shielding	EABmax*[GHz] (RL*[dB])	
2D C/Ni NP composites	Nanosheets	EW Shielding	9.68 (−39.46) at thickness 2.3 mm	[154]
2D organic α-$Co(OH)_2$	Nanosheets	EW Shielding	6.5 (−64) at thickness 2.5 mm	[155]
Fe_3GeTe_2	Nanosheets	EW Shielding	2.8 (−44.43) at thickness 1.45 mm	[160]
		Adsorption	Adsorption capacity [mg g^{-1}], (equilibrium time [h])	
2D α-$Ni(OH)_2$	Nanosheets	Congo red adsorption	259.74 (2 h)	[169]
$(Fe_7(PO_4)_6)$	Nanosheets	adsorption	704.23 (24 h)	[171]
		Other		
$CoTe_2$	Atomically thin sheets	Piezo-triboelectric nanogenerator	Generate 5 V under 1 N force	[176]
2D Ni NDA on ITO	Nanodot	Plasmonic devices	Localized surface plasmon resonance (LSPR) peak at 400 nm	[179]

η10, overpotential at an absolute current density of 10 mA cm^{-2}; OWS, overall water splitting; EABmax, maximum effective absorption bandwidth; RL, reflexion loss.

3.1. Spintronics

Any conventional device technology primarily relies on electrical transport process, in which charge carriers like electrons and holes are controlled in order to store and process data. Currently, with the advancement of fabrication techniques, it has become possible to scale down the devices to a size as small as the nanometer scale. It is worth considering that while reducing the size of device structures can benefit performance, it also creates physical limitations due to voltage scaling and dominating quantum effects like quantum mechanical tunneling. In consequence, gate tunnel leakage currents occur and the overall performance of the device decreases. Moreover, as the number of devices packed into a single chip increases, so does the higher density current flowing through it. This leads to a higher density of heat generation, which can be challenging for the achievement of heat dissipation efficiently.[62] Conventional technologies are struggling to keep up with these challenges, and finding ways to mitigate these issues is crucial for improving the efficiency and sustainability of electronic devices in the long run.

Spintronics is a promising field in electronics beyond complementary metal-oxide semiconductors (CMOS). It offers a unique approach to significantly reduce energy consumption while potentially utilizing quantum effects for information storage, logic, sensing, and data processing in a single device.[63] Here, the fundamental building blocks for the logic operation are governed by the manipulation of the spin of electrons. Spin polarization and spin current direction, such as spin-up (ON) and spin-down (OFF), are the foundations of spintronic logic. This is favorable because it requires orders of magnitude less energy to switch a spin state than it does to rearrange charge carriers. The two main spintronic phenomena that explain the operation principles of these devices are the giant magnetoresistance (GMR) effect and the tunneling magnetoresistance (TMR) effect.[63]

The use of 2D materials has enabled spintronics to conduct experiments and investigate magnetism theories that were quite challenging previously. The extensive research into the rapidly expanding family of 2D materials and associated heterostructures can give rise to multiple developments in novel spintronic devices like spin valves, spin-orbit torque, magnetoresistive random access memory (MRAM) and magnetic tunnel junction (MTJ), among others.

The electrical manipulation of magnetization was observed in exfoliated Fe_3GeTe_2 through the use of spin-orbit torque (SOT). The fabricated device consists of an exfoliated Fe_3GeTe_2 layer with a thickness 15–23 nm and a sputtered platinum (Pt) metal layer of a 5 nm thickness.[64] Pulsed current switching and second harmonic Hall measurements were performed to validate the SOT efficiency and magnetization switching. Damping torque was dominated in the heterostructure, which causes magnetization switching at $\approx 2.5\times10^{11}$ A m^{-2}. High SOT efficiency, magnetization switching, and low power consumption are essential for high-performance SOT devices. The SOT efficiency is comparable or even higher than conventional systems such as

CoFeB/Pt.[65] However, it is unclear why Fe_3GeTe_2/Pt has such a superior SOT efficiency. The authors assumed that the atomically flat Fe_3GeTe_2 makes an excellent interface that plays a significant role here; as a result, the high SOT efficiency may also be present in heterostructures composed of other vdW ferromagnets. A similar approach has also been employed to study the SOT-driven magnetization with few Fe_3GeTe_2 and Pt/Ta layers.[66] As the temperature rises, it was noticed that switching current and satugration magnetization decreased. The authors believe that the oxidation of Fe_3GeTe_2 in the interface could be thei reason behind this trend. To prevent the risk of oxidation, Zhang et al. fabricated the whole heterostructure in a glovebox with Fe_3GeTe_2 and Pt/IrMn.[67] They reported a low-temperature exchange bias of up to 895 Oe, which is currently the highest value among the vdWs-based bilayers. A high switching ratio of up to 60% was also reported for the perpendicular magnetization of the Fe_3GeTe_2/Pt heterostructure.

SOT switching has also been expanded with the atomically sharp interface of all-vdW heterostructure between WTe_2/Fe_3GeTe_2.[68,69] Formation of Te-rich interfacial layer of single atomic thickness (≈ 0.3 nm) has been reported with one order lower switching current density compared to previous reports with Fe_3GeTe_2/Pt; the authors predicted that a coupling between Te-rich interfacial layer with Te termination atoms of WTe_2 and Te termination layer of Fe_3GeTe_2 could be the possible reason for the low spin loss and scattering through this heterostructure.[69]

Fe_3GeTe_2-based Magnetic Tunnel Junctions (MTJs) have also been widely reported with different 2D semiconductor or insulator barrier layers such as Fe_3GeTe_2/h-BN/Fe_3GeTe_2, $Fe_3GeTe_2/WSe_2/Fe_3GeTe_2$, and Fe_3GeTe_2/InSe/Fe_3GeTe_2 (**Figure 6**).[70–72] These devices display TMRas high as 300% at low temperatures. Unfortunately, none of the TMRs were preserved because of the low Curie temperature of Fe_3GeTe_2, which is a real challenge for the implementation of these devices in practical applications. In line with this, Zhang et al. reported a record-high above-room-temperature Curie temperature (Tc, ≈350—380 K) for the Fe_3GaTe_2 system.[56] The PMA value from thickness-dependent hall transport measurements was 4.79×10^5 J m^{-3} for bulk crystals and ≈3.88×10^5 J m^{-3} for 9.5 nm thick flakes. The achieved values are comparable or even better than those of conventional magnetic thin film devices, e.g., CoFeB[73] and Co_2FeAl,[74] which renders Fe_3GaTe_2 an ideal candidate for room-temperature spintronics.

Jin et al. reported tunable TMR with Fe_3GaTe_2-based all vdW heterojunctions using WS_2 as a barrier with different thicknesses (Figure 6).[75] A maximum TMR ratio of 213% was calculated with barrier thickness of 3.5 nm at 10 K. By increasing the barrier thickness to 8 nm, the TMR ratio drops to 14%, and interestingly, by even further increasing to 16 nm, TMR ratio lowers down to 3.2%. It would be exciting to study barrier thickness optimization aiming toward a better TMR ratio. Furthermore, TMR ratio drops as the temperature rises, but it maintains its value up to 11% at ambient temperature. The spin-filtering effect is observed in the artificial polarity modulation of the TMR, which can vary from +213% to 9% with increasing bias. An elevated spin polarization of 72% was also reported, which is much higher in comparison with conventional FM electrodes, e.g., Co/graphene/Co[76] and NiFe/MoS_2/NiFe.[77] In another report, Zhu et al. demonstrated large room temperature TMR with WSe_2 as a barrier layer and Fe_3GeTe_2 as a top and bottom electrode.[78] Considering the perpendicular anisotropy of Fe_3GeTe_2, Zheng et al. also reported a spin-filtering effect by sandwiching the WSe_2 layer.[72]

Lin et al. developed a novel SOT-MRAM with Fe_3GeTe_2/MgO/Fe_3GeTe_2 heterostructure (Figure 6).[79] Verilog-A MRAM model and the commercial Cadence software with a foundry's 55 nm process design kit (PDK) were used to explore the device performance. The TMR ratio of the heterostructure was calculated to be 252%, improving the reading reliability of SOT-MRAM compared to the traditional CoFeB-based MTJ. In that work, a 3-transistor-2-MTJ (3T2M) memory cell was also presented for efficient sensing margin of the read value "0" from 26% to 132.6% and the read value of "1" from 29.8% to 67.2%. Finally, a nv-IMC circuit was also demonstrated, which performs AND/NAND and OR/NOR logic operations in sub-ns with extremely low energy consumption of 57.53 fJ and 57.86 fJ, respectively.

Both Fe_3GeTe_2 and Fe_3GaTe_2 have been used along with MoS_2 for the fabrication of all-2D vdW-based spin-valve devices with higher magnetoresistance than the conventional NiFe that has been mostly reported and used so far. In particular, $Fe_3GeTe_2/MoS_2/Fe_3GeTe_2$ and $Fe_3GaTe_2/MoS_2/Fe_3GaTe_2$ exhibited magnetoresistance of 3.1% and 11.97%, respectively, which is 8 times and 30 times correspondingly higher than NiFe/MoS_2/NiFe.[80,81]

Spin-valve devices are capable of altering the magnetic state of a material while at the same time aiming to probe spin-polarization components. In such devices, a Fe_5GeTe_2/graphene heterostructure with multi-dimensional spin polarization and

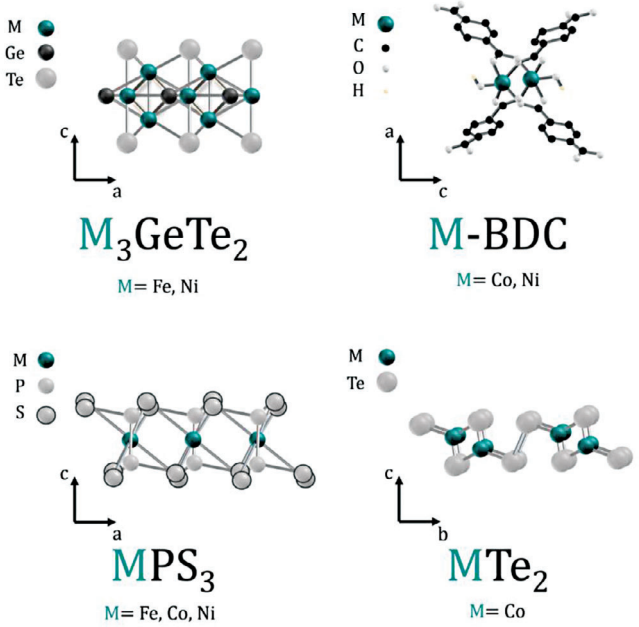

Figure 5. Graphic depiction of the crystal structure of different materials bearing ferromagnetic elements. (Top-left) ternary transition metal telluride, (top-right) metal-organic framework (MOF), (bottom-left) ternary transition metal phosphorus trichalcogenide and (bottom-right) transition metal dichalcogenide.

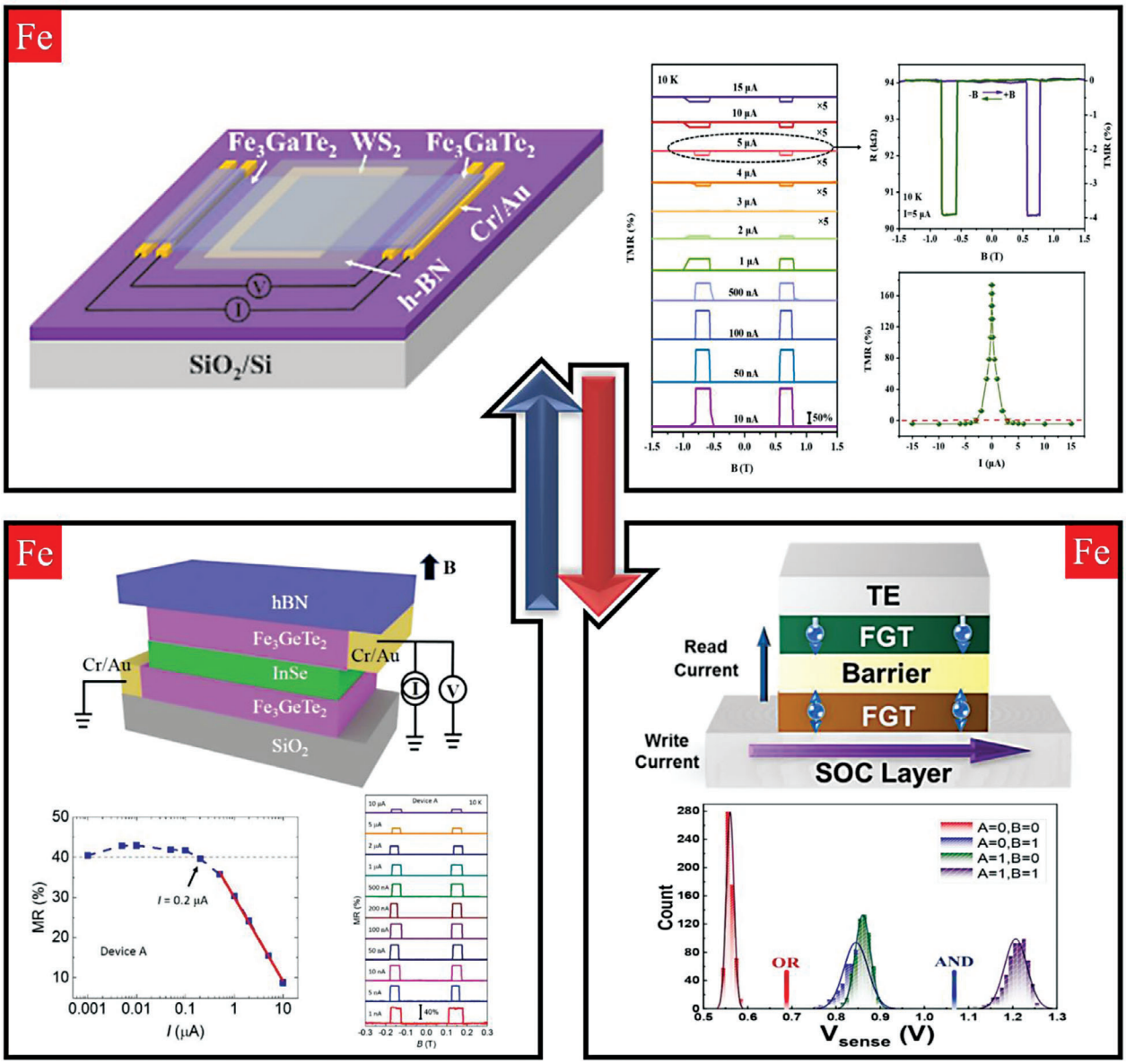

Figure 6. Spintronic devices employing 2D materials based on ferromagnetic elements. (Top) Schematic diagram of the $Fe_3GaTe_2/WS_2/Fe_3GaTe_2$ MTJ device, magneto-transport measurements at various bias currents from 10 nA to 15 μA at 10 K and the respective TMR curves. Reproduced with permission.[75] Copyright 2023, American Chemical Society. (Bottom-left) Schematic diagram of the device, MR curves and the respective extracted MR ratios as a function of bias current ranging from 1 nA to 10 μA at 10 K. Reproduced with permission.[70] Copyright 2021, Wiley-VCH. (Bottom-right) schematic diagram of the MTJ device and the implication of in-memory logic computation. Reproduced with permission.[79] Published under an open access CC BY license, MDPI.

itinerant ferromagnetism at room temperature permits spin injection, transport and detection. The Fe_5GeTe_2 flakes function as a spin injector or detector, while graphene has the role of the spin transport channel. The efficiency of the spin-valve device is ascribed to the vdW heterostructure interface, which exhibits a different remanent magnetism from the bulk Fe_5GeTe_2.[82]

Unlike ferromagnets, and despite their lack of magnetization, antiferromagnetic materials have enormous potential in a variety of sectors, including data storage and SOT devices. Zhang et al. demonstrated the fabrication of two different device structures, e.g., $FePS_3/Fe_3GeTe_2$ and $FePS_3/Fe_3GeTe_2/FePS_3$.[83] The thickness of exfoliated $FePS_3$ and Fe_3GeTe_2 were 6.2 and 8.2 nm, respectively. Enhancement in transition temperature and the coercive field was noticed due to proximity coupling of Fe_3GeTe_2 with $FePS_3$ via modulation of the domain by $FePS_3$ at the junction.

Gong et al. reported an intriguing method for extracting net magnetization from 2D antiferromagnets $FePS_3$.[84] In the heterostructure of WS_2 and $FePS_3$, the spin magnetic moments can effectively pair with 2D transition metal dichalcogenides like WS_2, thanks to its out-of-plane orientation. Ferromagnetism

emerges as a result of the high Néel temperature of $FePS_3$, which sustains the high-temperature ferromagnetic phase at the interface. The enhanced Zeeman effect is made possible by the interfacial exchange fields between WS_2 and $FePS_3$, which assists the magnetization of the system. This discovery opens the door for novel applications of emergent ferromagnetism in spintronics.

Wang et al. reported a fast, reliable, and non-destructive approach to determine Néel vector orientation and spin properties of bulk and trilayer $NiPS_3$ via spin-induced photoluminescence polarization.[85] They reported a distinct peak at 1.476 eV for bulk and trilayer samples. Manipulation of the photoluminescence polarization was conducted by adding an in-plane magnetic field. Temperature- and magnetic-field-dependent spectroscopic study confirms the linear polarization of the sharp emission, which is associated with the $NiPS_3$ Néel vector orientation. This study provides concepts for the construction of opto-spintronics in 2D systems. It allows a fast read of the spin characteristics in bulk and atomically thin $NiPS_3$ flakes using simple steady-state spectroscopy. Large interfacial spin-orbit torque was observed between the bilayer ferromagnet ($Ni_{80}Fe_{20}$; Py) and $NiPS_3$.[86] Due to large in-plane damping-like interfacial torque, very high torque conductivity was measured at room temperature. Further, out-of-plane field-like torque was also observed in the interface, indicating spin-orbit coupling in the system.

Liu et al. reported paramagnetic to antiferromagnetic phase transition in exfoliated monolayer $CoPS_3$ by using polarization-resolved Raman spectroscopy.[87] The phonon mode splitting of Co-atom-related vibration in Raman spectra indicates a structural change. The phase transition temperature was found to be at 100 K for mono to quadlayer, indicating the magnetostrictive effect in the presence of quasi-long-range ordering below transition temperature for a 2D XY-type antiferromagnet. This finding will assist in removing specific barriers to the production of future antiferromagnetic storage devices and provide insight into the underlying mechanism of the magnetostrictive effect in 2D materials. In another study, Wang et al. reported modulation of magnetism by spin transfer torque (STT) in Weyl semimetal $Co_3Sn_2S_2$.[88] The magnetic moments depend on torques when a spin-polarized current flows through a non-uniform magnetic pattern or domain walls, which might result in an STT. Direct current was employed to modify the coercivity of $Co_3Sn_2S_2$ flakes at low current densities which is carried out using STT-assisted domain wall propagation and helps in the magnetization reversal procedure. The current density for driving the domains was 5.1×10^5 A cm^{-2} and 1.5×10^5 A cm^{-2} with zero and moderate external field (0.2 kOe), respectively. The maximum STT field was found to be 2.4–5.6 kOe MA^{-1} cm^2 at 150 K.

After years of investigating basic principles of spintronics and fabricating proof-of-concept devices, significant advancement has been made in 2D spintronics research. However, there are still several scientific and practical challenges that need be resolved in order to fully develop real-world spin memory and logic devices. While room-temperature magnetic heterostructures and tunable TMR have been demonstrated, their coercive fields are found to be very low. To increase the robustness and stability of these devices, it is essential to develop materials or heterostructures with sufficient coercive fields. This emphasizes the requirement for additional study and progress in this area to address this critical issue. In addition, aiming to optimize the functionality of magnetic heterostructures, interface quality should be improved in the junction. It has been observed that vacuum fabrication of Fe_3GeTe_2 boosts overall device performance. Devices with 2D ferromagnets exhibit magnetization switching by electrical modulation with high STT, as well as SOT efficiency at low temperatures, which opens an enormous scope for low-power spintronics. Finally, scaling of the vdW materials at a wafer scale is still a rather challenging goal, when envisaging a high suitability for practical applications. Currently, lab-scale state-of-the-art devices are being prepared through mechanical exfoliation, which complicates the achievement of a well-advanced integration with present CMOS technology.

3.2. Electrocatalysis

Nowadays, environmental crises and global warming impose the replacement of fossil fuels with renewable alternatives. Hydrogen can be a promising energy carrier thanks to its eco-friendly characteristics and cost-effective production through the electrocatalytic water splitting reaction.[89,90] Hydrogen evolution reaction (HER) at the cathode and oxygen evolution reaction (OER) at the anode are the two half-reactions leading to water splitting. Noble-metal electrocatalysts have been extensively studied for these reactions, thanks to their outstanding performance.[91,92] Nonetheless, their low abundance and high cost necessitate the exploration of new non-precious electrocatalysts for HER and OER with similar or even better performances.[93] Common ferromagnetic elements (Fe, Co, Ni) are favorable candidates for forming non-noble metal electrocatalysts and easing hydrogen production.[94–96]

Recent research has demonstrated that magnetic properties and magnetic fields can have a positive impact on electrochemical reactions through various possible effects, including the magnetothermal effect, magnetohydrodynamic effect, spin selectivity effect, Maxwell stress effect, and Kelvin force effect. These effects often function jointly and influence various aspects of the reaction mechanism, such as i) mass transfer and spin orientation of paramagnetic species, ii) charge transfer resistance, iii) shape and size of the droplets and bubbles on the electrode/electrolyte interface, iv) electrochemical double-layer capacitance, improving every type of electrocatalytic reaction (e.g. HER, OER) in a different extent.[97–101]

Monzon et al. compared the performance of zinc, iron and cobalt deposited on polyaniline-coated gold electrodes toward the electrocatalytic oxygen reduction reaction (ORR) along with the effect of a magnetic field. The presence of a permanent magnet inducing 360 mT enhanced the performance of all three metals in a different manner and to varying degrees. Such enhancement was lower for Zn compared to the other two metals and it was attributed to the magnetohydrodynamic flows caused by the interaction between the magnet and the local current density, which is driven by Lorentz force. In the case of Fe and Co elements, the external magnetic field not only created a magnetohydrodynamic flow but also magnetized the metal particles, generating a non-uniform stray field in their vicinity. This attracted molecular O_2 toward the surface, which is paramagnetic, further boosting their performance.[102]

Furthermore, Wang and co-workers investigated the magnetic enhancement of electrocatalytic HER by introducing ferromagnetic properties to MoS_2 flakes and applying an external magnetic field. Their impedimetric results revealed that the ferromagnetic MoS_2 showed lower electron transfer resistance in the presence of the perpendicularly applied external field, resulting in an improved electron hopping efficiency and thus ameliorated HER performance. Interestingly, the parallel applied external field did not have the same impact on the electron transfer resistance, highlighting the importance of the orientation of the applied magnetic field. Meanwhile, the non-magnetic bilayer MoS_2 remained largely unaffected in the presence of both perpendicular and parallel magnetic fields.[103]

Therefore, the design of intrinsically magnetic materials that are able to induce the above-mentioned magnetic phenomena is promising to enhance electrocatalytic properties, providing a possible alternative to traditional catalysts with improved efficiency. Additionally, investigating materials with distinct magnetic properties (ferromagnetic, antiferromagnetic, paramagnetic) can offer a better understanding of magnetic field-enhanced electrocatalysis, paving the way for discovering new, advanced electrocatalysts.[98]

2D structures, thanks to their large surface area, provide abundant exposed active sites that catalyze the reaction, boost the catalytic activity, and lead to lower reaction overpotential.[104] In light of that, several studies report on 2D materials incorporating ferromagnetic elements with high electrocatalytic activity towards either HER or OER or even both of them, rendering the material an efficient bifunctional electrocatalyst.[105,106]

Zhao et al. revealed through DFT calculations that the basal plane of Fe_3GeTe_2 exhibits high electrocatalytic activity toward OER, suggesting a new mechanism in OER reaction in which surface hydroxyl undergoes a self-reduction into water. So instead of forming OOH* in the catalytic site as the classical pathway suggests,[107] the authors proposed the formation of O* and OH* in the catalytic site. Among them, OH* will be favorable to experience self-reduction resulting in water formation. The alternative pathway affects the rate-determining step, lowering the reaction overpotential from 0.86 to 0.30 V.[108] Theoretical calculations on metal sulfides (MS) suggest that 2D FeS monolayer is a good electrocatalyst toward HER in comparison with VS and MnS and provides three symmetrical sites to hold the hydrogen atom, the top site of S and the top site of Fe as well as a hollow site which is the more stable one. Different transition metals lead to distinct hydrogen coverage, thus to a modified HER activity.[109]

Oliveira et al. compared the efficiency of Fe_3GeTe_2 and Ni_3GeTe_2 in their bulk form and shear force exfoliated form, highlighting the use of different ferromagnetic elements towards HER and OER in acidic, neutral, and alkaline conditions. Fe_3GeTe_2 and Ni_3GeTe_2 exhibited ferromagnetic and antiferromagnetic behavior in their bulk form, respectively. They performed similarly towards HER in acidic and alkaline conditions, while in neutral conditions (0.1 M PBS pH 7), bulk Ni_3GeTe_2 exhibited two times lower overpotential than Fe_3GeTe_2. The exfoliated forms of these two materials exhibited the same trend but not with such a big difference between them. As for the OER, the explored materials performed similarly, displaying insignificant differences from each other. This study demonstrated that in ternary transition metal tellurides, the metal properties are more critical than the material form (bulk or exfoliated) in what concerns the resulting activity in water-splitting electrocatalysis.[110]

Two-dimensional metal-organic framework (MOF) Ni-BDC (BDC = 1,4- benzenedicarboxylate) exhibits a promising electrocatalytic performance toward OER with an overpotential of 360 mV and a Tafel slope of 60 mV dec^{-1} but suffers from the aggregation of its 2D nanosheets, thus restricting its use as OER electrocatalyst. In order to address the risk of aggregation and enhance its electrocatalytic activity towards OER, Ni-BDC was successfully combined with other materials, leading to the creation of heterostructures with better performance. In particular, Fe_3O_4[111] and $Ni(OH)_2$[112] in two different studies were incorporated in the 2D Ni-BDC structure, and as a result, the overpotential of the heterostructures was 295 and 320 mV, with Tafel slopes being 47.8 and 41 mV dec^{-1}, respectively. Both studies attributed this enhancement both to the prevention of aggregation of Ni-BDC and to the higher oxidation states of Fe and Ni atoms in Fe_3O_4 and $Ni(OH)_2$, correspondingly. Surprisingly, Fe_3O_4 on its own is a poor electrocatalyst toward OER, but it positively affects Ni-BDC upon their combination. Material preparation and the electrocatalytic performance towards OER of Ni-BDC/$Ni(OH)_2$ heterostructure is demonstrated in **Figure 7**.

Zhang et al. also tested 2D Ni-BDC for HER, but this time iron phthalocyanine (FePc) was the material anchored on the ultrathin structure of the MOF (Figure 7). In that study, FePc@bulk-BDC was also investigated for comparison purposes. The 2D material and the bulk counterpart exhibited η_{10} overpotential (for current of 10 mA cm^{-2}) of 334 and 495 mV, with the Tafel slope being 72.1 and 90.2 mV dec^{-1}, respectively.[113]

The aforementioned studies on 2D Ni-BDC pave the way for further investigation of the potential of 2D Ni-BDC heterostructures to achieve a remarkable electrocatalytic activity in HER and OER, thus becoming highly sought bifunctional electrocatalysts for the overall water-splitting reaction.[114] Li et al. employed a partial phosphorization method for the synthesis of 2D CoP/Co-BDC heterostructure nanosheets on carbon fibers. The produced composites were evaluated for HER as self-supported electrocatalysts (Figure 7). As the carbon paper substrate is considered electrochemically inert for HER, the electrocatalytic activity identified was attributed only to the 2D CoP/Co-BDC. Therefore, in acidic, neutral, and alkaline conditions, it showed Tafel slopes of 49, 89, and 53 mV dec^{-1}, respectively. Impressively, the performance of the studied material outperforms the Pt/C in alkaline conditions. The exceptional electrocatalytic activity of 2D CoP/CoMOF is ascribed to the presence of nanoholes which are associated with the generation of a plethora of accessible active sites for catalysis.[115]

Jeung et al. prepared 2D Ni-based metal phosphide-sulfide ($NiMP_xS_y$, M = Co, Fe) by co-ion exchange method. On the one hand, the electrocatalytic performance of NiCoPS in HER in alkaline conditions was superior to NiCoP and NiCoS with an overpotential η_{10} of 61 mV versus 75 mV and 66 mV, respectively, and a Tafel slope of 44.5 mV dec^{-1}. On the other hand, NiFePS exhibited a lower overpotential η_{10} toward OER in alkaline conditions with a value of 242 mV and a Tafel slope of 38 mV dec^{-1}, while NiFeP and NiFeS exhibited slightly higher overpotentials η_{10} with values 250 and 260 mV, respectively. In the next step, overall water electrolysis was performed with NiCoPS serving as the cathode

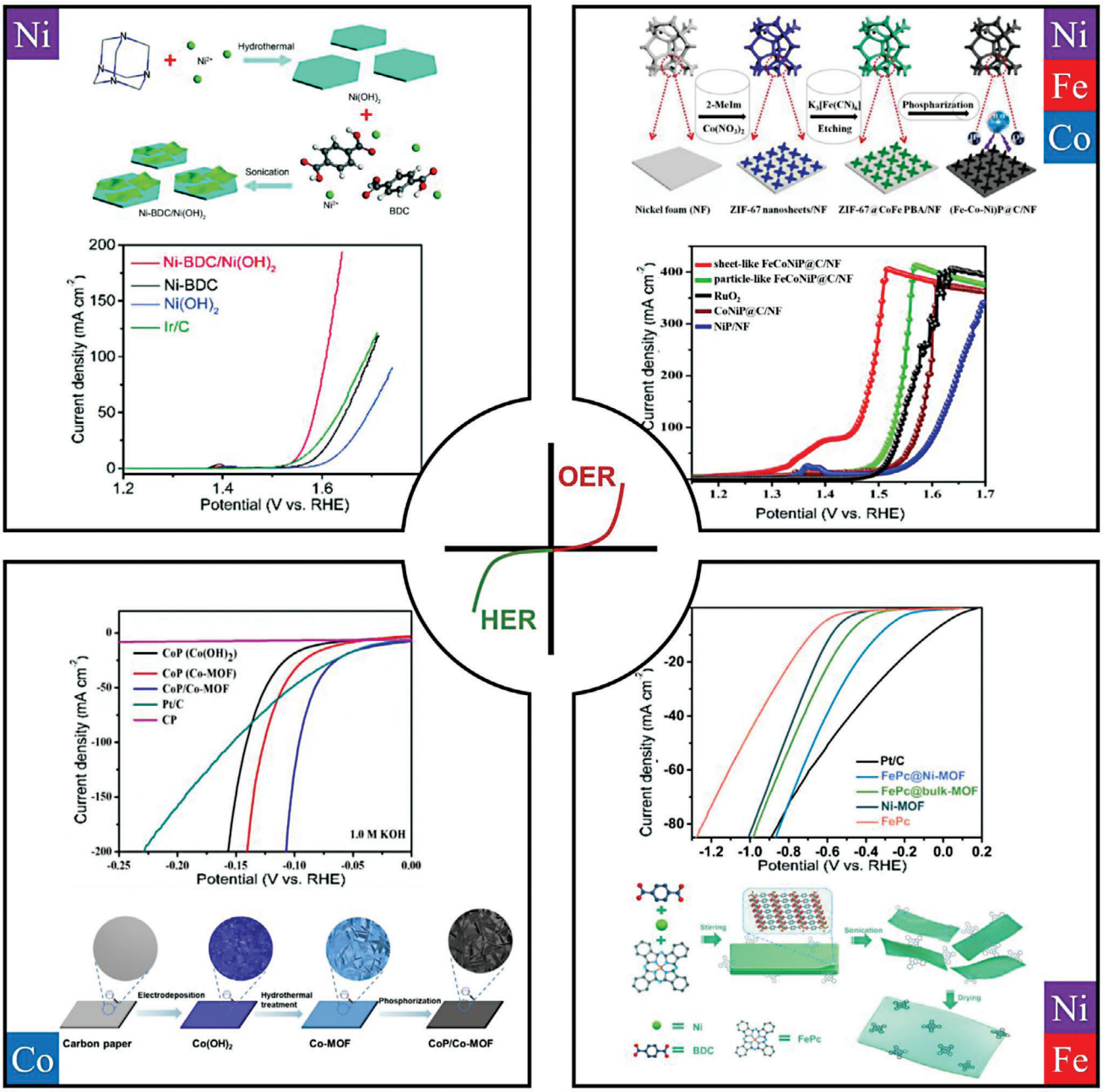

Figure 7. 2D materials based on ferromagnetic elements as electrocatalysts toward OER and HER in alkaline conditions (1.0 M KOH). For every case a scheme is demonstrated illustrating the material preparation procedure and a Linear Sweep Voltammetry (LSV) polarization curve displaying electrocatalytic performance. (Top-left) Ni-BDC/$Ni(OH)_2$ heterostructure for OER. Reproduced with permission.[112] Copyright 2019, Royal Society of Chemistry. (Top-right) 2D Ni-based metal phosphide-sulfide (NiMPS, M = Co, Fe) for OER. Reproduced with permission.[94] Copyright 2021, Elsevier. (Bottom-left) 2D CoP/Co-BDC heterostructure nanosheets for HER. Reproduced with permission.[115] Copyright 2021, Elsevier. (Bottom-right) FePc@2D Ni-MOF for HER. Reproduced with permission.[113] Copyright 2021, American Chemical Society.

(HER) and NiFePS acting as the anode (OER); the catalyst system had a low overpotential of 310 mV and a high stability.[116] Yao et al. prepared 2D CoS_2 nanosheets by vulcanizing well-aligned MOF-array precursors. The nanosheets were grown on carbon cloth and were interconnected to form an open 3D hierarchical architecture. The produced material exhibited good electrocatalytic activity toward both HER and OER, thus being a bifunctional electrocatalyst toward the overall water-splitting reaction. Specifically, the Tafel slopes for HER and OER are 48 and 92 mV dec^{-1} respectively, while the whole water splitting reaction can be achieved in a low cell voltage of 1.58 V at the current density of 10 mA cm^{-2} with long-term stability: almost no degradation was observed after continuous electrolysis for 80000 s.[117]

Zhang et al. synthesized mixed metal phosphide nanosheets via a high-temperature phosphorization strategy onto a nickel foam (FeCoNiP@C/NF) and tested their electrocatalytic performance. As a result, the sheet-like catalyst outperforms the particle-like and RuO_2 both in HER and OER (Figure 7) with an overpotential of 136 and 227 mV at a current density of 100 mA cm^{-2} in alkaline conditions. The material was therefore utilized both as anode and cathode in full cell overall water splitting, and only 1.6 V was needed to reach 100 mA cm^{-2}, demonstrating its suitability as a promising bifunctional electrocatalyst.[94]

To summarize this sub-section, it is worth noting that ferromagnetic elements offer a cost-effective alternative to noble metals in electrocatalysis, providing abundant metallic active sites that benefit the water-splitting reaction. They may also induce a range of magnetism-related effects which can be beneficial for electrochemical activity, especially in the presence of a suitably applied external magnetic field. Studies have shown that the 2D form of these materials is more effective in electrocatalysis thanks to its larger surface area compared to its bulk form. Regarding experimental conditions, the majority of these materials perform adequately under acidic conditions; in alkaline conditions, though, they display a superb activity, sometimes even outperforming benchmark materials like Pt/C for HER and IrO_2 for OER (**Table 1**).

3.3. Sensing

Besides the significant electrocatalytic properties toward water splitting reaction, 2D materials with a ferromagnetic metal as a constituent can also ease the redox reaction of other electroactive species for the development of sensing applications promoting their fast and facile determination in samples of medicinal, food, or environmental interest.[118,119] In addition, the combination of such materials with magnetic electrodes could possibly lead to an outstanding performance thanks to spin orientation and improved modification that the magnetic attraction offers.[97,120,121] An appropriate magnetic field can enhance the charge transfer ability of a material, which in turn improves its sensing capabilities and sensitivity.[103,122] In the case of paramagnetic species, the presence of a magnetic field can introduce a new mechanism for selective chemical analysis by sorting diamagnetic and paramagnetic species in a complex sample.

Tong et al. presented the fabrication of biphasic nickel phosphide nanosheet (BNPNS) electrocatalysts through a direct phosphidation of nickel foam. This electrocatalyst was applied for the amperometric determination of H_2O_2 at a constant potential of −0.71 V (vs Ag/AgCl) with a detection range of 0.05 to 100 µM, fully covering the physiological conditions (0.05–50 µM) of a human body. As a result, the authors successfully utilized the sensor for the determination of H_2O_2 in human blood and in continuously releasing H_2O_2 living cells.[123] Additionally, a 2D layered nickel cobalt phosphide (NiCoP) nanosheet confined by 3D graphene frameworks (GF) served as a non-noble metal electrocatalyst for H_2O_2 determination, resulting in a much lower overpotential of −0.3 V (vs Ag/AgCl). A wide detection range was observed; more specifically, three linear response concentration ranges starting from 0.2 to 1.8 µM, from 1.8 to 10.8 µM, and from 10.8 to 9330 µM were confirmed, and the limit of detection was calculated to be as low as 0.028 µM. These thin NiCoP/GF nanosheets were successfully applied for real-time detection of H_2O_2 released from B16 melanoma cells.[124]

Balasubramanian et al. reported on defect-engineered 2D cobalt hydroxide nanosheets VCo-Co$(OH)_2$ with good electrocatalytic oxidation performance toward glucose and L-cysteine reaching a limit of detection of 295 nM and 76.5 nM, respectively. A comparison between the defect engineered and the defect-free 2D material revealed that defects induced in the 2D material led to abundant cobalt vacancies, and therefore to enriched electroactive sites and charge transfer rates. The resulting screen-printed electrode modified with VCo-Co$(OH)_2$ is a low-cost, disposable and easily fabricated sensor that can be applied for the determination of analytes in human blood serum.[125] Furthermore, for glucose determination, ultrathin 2D nickel-cobalt phosphate nanosheets were isolated by a one-step hydrothermal method. The nanomaterial composition influenced the electrochemical performance, as a Ni/Co ratio of 2:5 exhibited higher electrocatalytic activity for glucose oxidation than a Ni/Co ratio of 4:5 or only Co. The material was dispersed in a 1% Nafion solution (in EtOH) and drop-casted onto a glassy carbon electrode. The 2D NiCo/GC showed a linear range of detection of 2–4470 µM and a detection limit of 0.4 µM. The optimized sensor was applied to a human serum sample.[126]

Sukanya et al. prepared chemically reduced nickel boride (Ni_3B) nanoparticles anchored on 2D layered cobalt selenide (CoSe) nanosheets using hydrazine assisted hydrothermal method. A strong synergistic effect between the different components allowed the improvement of the electrocatalytic activity of the 2D CoSe/Ni_3B heterostructure toward the reduction of 5-nitroquinoline, which is a water pollutant (**Figure 8**). A 6 mg ml^{-1} suspension of the heterostructure was drop-casted on a screen-printed electrode, and the material showed a linear range of detection in the range 0.2-378 µM with a limit of detection of 0.042 µM for 5-nitroquinoline. Following an optimization and interference study of the sensor, the heterostructure was successfully used for real-time monitoring of 5-nitroquinoline in tap, rain, and lake waters of the city of Daegu in South Korea. The reliability of the sensor was corroborated by recovery experiments, with results ranging between 95–102%, with a standard deviation being almost 3%.[127]

Wang et al. reported the preparation of 2D FeS nanoflakes by a solvothermal method. The product was used as a glassy carbon electrode modifier for the detection of Hg^{2+} ions (Figure 8). These polycrystalline nanoflakes consisting of many small crystals exhibited linearity in what concerns the relation between oxidation peak current and logarithm of Hg^{2+} concentration, over the concentration range of 0.01 – 10 µM. The detection limit was as low as 4 nM. The proposed detection mechanism of FeS nanoflakes relies on the ability of Hg^{2+} to form stable HgS, which is measured through cyclic voltammetry as it converts into Hg_2S. The sensor was applied for tap and river water analysis.[128] Furthermore, a 2D Ni-BDC (MOF) nanosheet was utilized in a wearable sensor for the potentiometric detection of Ni^{2+} ions (Figure 8). The 2D Ni-MOF operated as the electroactive material in highly porous carbon cloth doped with nitrogen and decorated with spherical porous carbon nanoparticles as a self-standing substrate. The flexibility

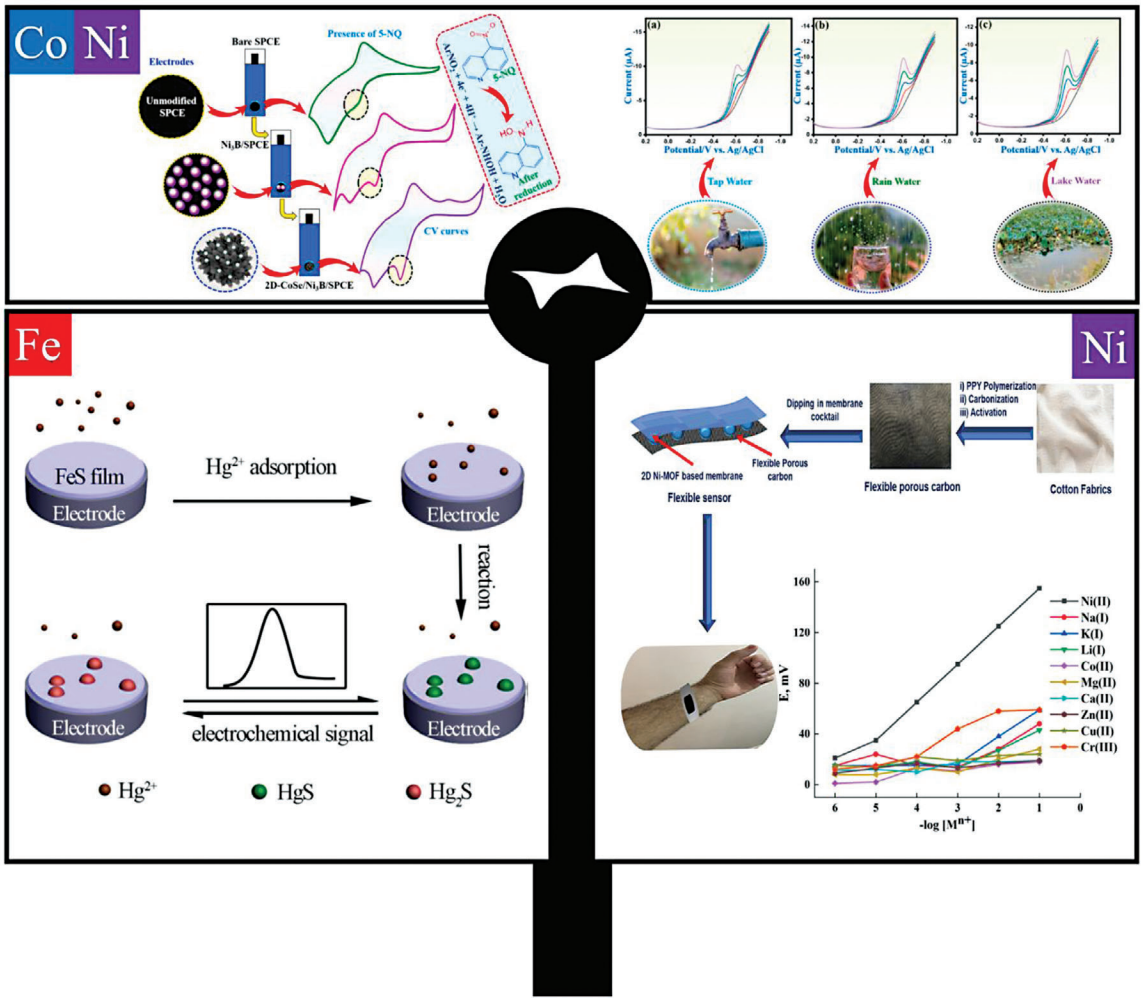

Figure 8. Electrochemical sensors based on 2D materials incorporating ferromagnetic elements; (top) demonstration of electrocatalytic activity, reaction mechanism, and real sample analysis of 5-nitroquinoline with screen-printed sensors modified with 2D CoSe/Ni_3B heterostructure. Reproduced with permission.[127] Copyright 2023, Elsevier; (bottom-left) schematic illustration of the sensing strategy of 2D FeS nanoflakes for the detection of Hg^{2+} ion. Reproduced with permission.[128] Copyright 2015, Springer; (bottom-right) demonstration of fabrication procedure and selectivity test of a potentiometric wearable sensor based on 2D Ni-BDC for Ni^{2+} detection. Reproduced with permission.[129] Copyright 2022, Elsevier.

of the sensor did not affect the stable and accurate response of Ni^{2+} over the concentration range of 10 µM to 0.1 M, with the limit of detection being 2.7 µM. The sensor was tested for biological (saliva and sweat) and environmental (tap water) samples.[129]

As a conclusion for this sub-section, it is noted that ferromagnetic element-based 2D materials offer attractive detection capabilities for non-enzymatic determination of H_2O_2 and glucose. This category of materials has the potential to provide excellent sensing features for various analytes. The sensor performance can be influenced by the i) synergistic effect of metallic centers, ii) concentration ratio of the different metallic centers, iii) morphological characteristics and the possible structural defects that may be present in the materials and iv) presence of an appropriate applied magnetic field. Combining these materials with innovative technologies such as magnetic electrodes and wearables can benefit their use in point-of-care applications.

3.4. Energy Storage

Materials of 2D incorporating ferromagnetic elements have been used for energy storage and conversion applications such as batteries and supercapacitors. A 2D Co_2GeO nanosheet prepared by a simple hydrothermal method operated as a lithium-ion battery (LIB) anode, presenting a notable electrochemical performance thanks to its large surface area, as shown by its ultrathin structure (thickness lower than 10 nm) and its atomically metallic matrix. It was found that Co_2GeO decomposed into Ge nanoparticles with a 5 nm diameter that gradually migrated together during the cycling but did not aggregate in the sheet plane. After the second cycle, the Co_2GeO anode exhibited a stable cycling performance with a coulombic efficiency of 98%; the recorded capacity on the 150th cycle was 1026 mA hg^{-1}, indicating high capacity retention.[130]

Liang et al. reported on 2D ternary layered metal phosphorus trichalcogenide (MPS_3, M = Fe, Co, Ni) and investigated the

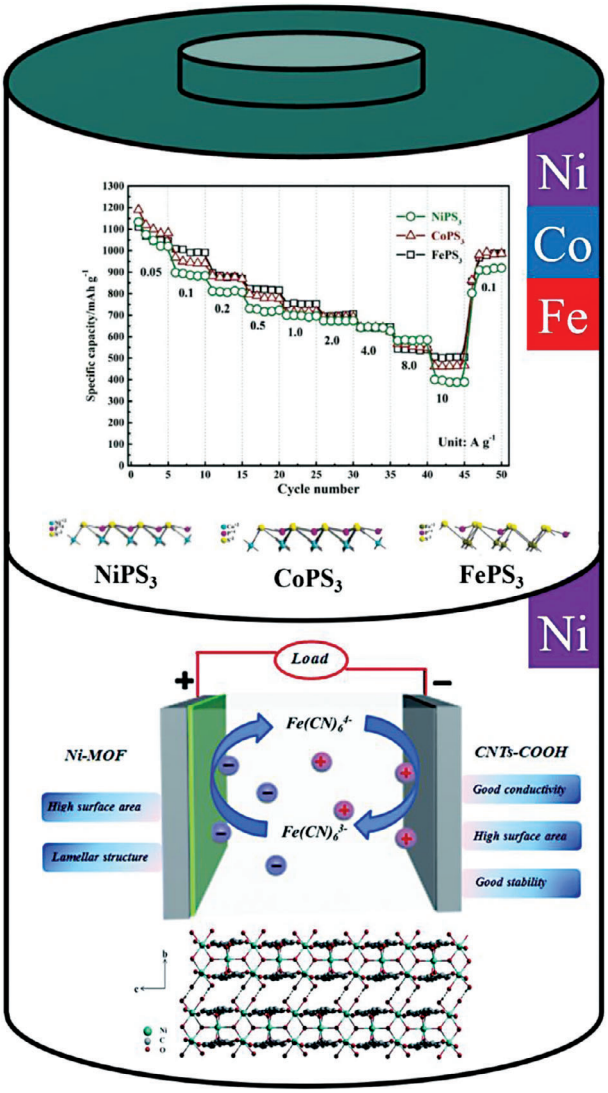

Figure 9. Batteries utilizing 2D materials based on ferromagnetic elements; (top) demonstration of specific capacities in correlation with current densities and cycle number for 2D ternary layered metal phosphorus trichalcogenide (MPS_3, M = Fe, Co, Ni) in lithium-ion batteries. Reproduced with permission.[131] Copyright 2017, Wiley-VCH; (bottom) schematic illustration of an alkaline battery-supercapacitor hybrid device utilizing Ni-BDC as an anode. Reproduced with permission.[133] Copyright 2016, Royal Society of Chemistry.

tuning of Li/Na storage properties based on the metal center alteration. The MPS_3 nanosheets had a thickness of less than 20 nm and an average lateral size of 200 nm. At a current density of 0.05 A g^{-1}, the specific capacity of LIBs was 1026, 1086, and 1046 mA h g^{-1} in $NiPS_3$, $CoPS_3$ and $FePS_3$, while for sodium-ion batteries (SIBs) at the same current density, it was 910, 846, and 754 mA h g^{-1}, respectively. The changes in the specific capacities as a function of current densities for LIBs are demonstrated in **Figure 9**.[131]

Ma et al. reported on a 2D composite α-$Ni(OH)_2$ monolayer and reduced graphene oxide as an electrode material for use as supercapacitor. The 2D nanostructure allowed the fast transfer of electrolyte ions minimizing the effect of the diffusion process, while the intercalated rGO lowered the internal resistance of α-$Ni(OH)_2$ and prevented agglomeration. The specific capacitance of the composite was in the range of 2676-1040 F g^{-1} for scan rates of 5–100 mV s^{-1}, which has higher values than that of α-$Ni(OH)_2$ or the mixture of α-$Ni(OH)_2$ and rGO.[132] In another report, Ni-BDC (Ni-MOF) was once again investigated for an electrochemical application; in that case, the material under discussion was utilized as an anode for an alkaline battery-supercapacitor hybrid device where carboxylic acid functionalized carbon nanotubes (CNTs-COOH) served as the cathode; in that work, the authors employed $KOH/K_4Fe(CN)_6$ as the electrolyte. The synergistic effect of Ni-MOF and $Fe(CN)_6^{4-}/Fe(CN)_6^{3-}$ redox couple enhanced both the energy density and power density of the device (Figure 9). This device exhibited at the same time an energy density comparable to lithium-ion batteries and a power density approaching supercapacitors.[133]

It is highlighted that ferromagnetic elements can participate in energy storage applications as part of the electrode material or/and the electrolyte, facilitating the charge transport ability of the device. When used as electrode material, the performance and the stability of the device are strongly affected by the alteration of the elemental composition of the material.

3.5. Photocatalysis

In the attempt to discover alternative renewable energy sources, photocatalysis has attracted a lot of attention. The development of suitable photocatalytic materials will permit the production of H_2 or CO_2 by the mere utilization of visible light.[134] A material is considered an effective photocatalyst for water splitting/H_2 production when its conductive properties allow it to possess a high photon-harvesting capacity. Most often, 2D materials are more efficient photocatalysts than their bulk counterparts; low dimensional materials offer shorter transport paths on the surface for photoexcited holes and electrons to react, leading to a low electron-hole pair recombination, which is highly desirable for a good photocatalyst. In addition, the good durability, excellent conductivity, and large surface area with highly exposed active sites render 2D materials promising candidates for photocatalytic applications.[135]

Among 2D photocatalysts, graphitic carbon nitride (g-C_3N_4) stands out as an inexpensive and highly efficient photocatalyst. In combination with other semiconducting materials, the photocatalytic properties can be enhanced.[136] One of the cases concerns the matching of g-C_3N_4 with a 2D bimetallic RuNi alloy prepared hydrothermally that acts as a co-catalyst (**Figure 10**). It provided more reaction sites and, thus, exhibited better H_2 absorbing and desorbing performance. RuNi/g-C_3N_4 composites had a higher photocatalytic activity compared to g-C_3N_4 nanosheets, but an excessive loading of RuNi led to the opposite result due to optical shielding and lower absorption of photons. Even though Ru content was critical for the photocatalytic performance of the material, the ameliorated photocatalytic performance was attributed to the synergy effect of Ru and Ni in the bimetallic alloy. This was supported by the fact that Ru/g-C_3N_4, with the same Ru content

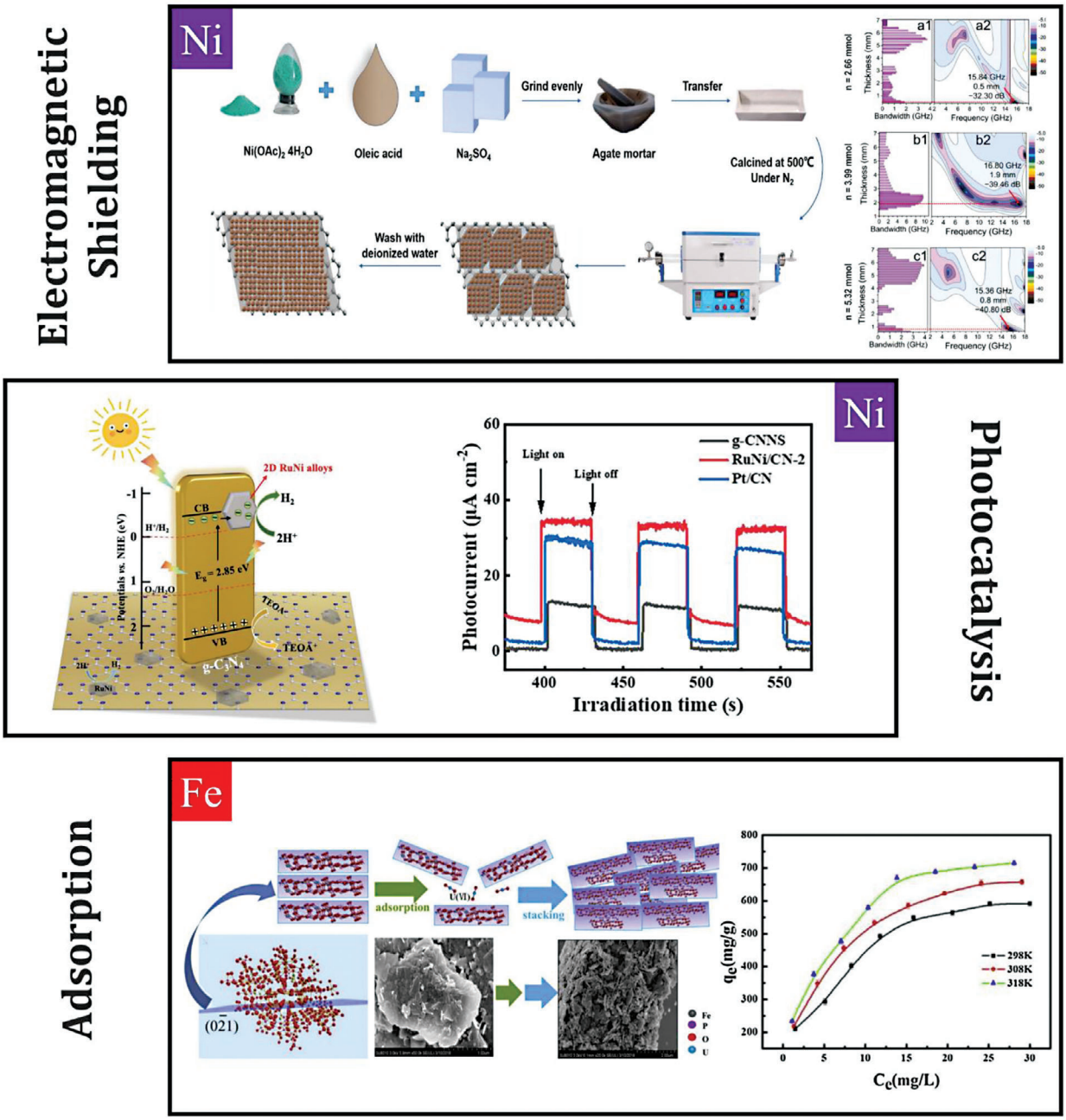

Figure 10. (Top) schematic illustration of the formation mechanism of 2D C/Ni nanoparticle composite and its frequency characteristics (effective bandwidth and 2D projective images) for various amounts of nickel acetate precursor (n = 2.99, n = 3.99, n = 5.32 mmol). Reproduced with permission.[154] Copyright 2022, Elsevier; (middle) schematic representation of the proposed pathway of the photocatalytic H_2 generation mechanism in 2D RuNi/g-C_3N_4 photocatalysts and their transient photocurrent response. Reproduced with permission.[137] Copyright 2021, Elsevier; (bottom) scheme illustrating the mechanism of U(VI) adsorption, morphological changes, and adsorption isotherms at different temperatures (Langmuir model). Reproduced with permission.[171] Copyright 2019, Elsevier.

as RuNi/g-C_3N_4, exhibited 3 times lower photocatalytic performance, highlighting the importance of Ni presence.[137]

In the case of photocatalytic reduction of CO_2, due to its inertness, it is very challenging to develop photocatalysts that are able to capture and activate CO_2 at the same time.[138] Ni-based MOFs exhibit high CO_2 adsorption thanks to the strong binding between CO_2 and open Ni sites.[139] A Ni-BDC MOF, with the molecular type $[Ni_3(OH)_2(1,4\text{-}BDC)_2\text{-}(H_2O)_4]\cdot 2H_2O$, transformed from 3D bulk to 2D single-layer after the breaking of the interlayer hydrogen bonds by CO_2 molecules. CO_2 contributed to the exposure of the active sites of the 2D Ni-BDC, enhancing the photocatalytic activity. In particular, the efficiency of the reduction of CO_2 into CO was 96.8%, and the quantum yield was 1.75%. Intriguingly, CO_2 participated

in the preparation of the photocatalyst, which enabled its own reduction.[140]

Computational studies helped to shed light on the photocatalytic properties of chemically modified 2D cobalt porphyrin-based MOFs (PMOFs) through DFT calculations. It was shown that the CoO-modified cluster outperforms the ones modified with ZnO and ZrO, rendering Co-PMOF a superior catalyst for photocatalytic CO_2 reduction. This was ascribed to the collaborative contribution of CoO and cobalt porphyrin. PDOS (projected density of states) revealed that Co 3d states of CoO and cobalt porphyrin are contributing to the conduction band and valence band, respectively, which is favorable for electron transfer.[141] From the mechanistic point of view, during the photocatalytic process, cobalt is reduced from Co(II) to Co(I), and CO_2 binds to the Co(I) oxidation state of the porphyrin.[142]

Later on, a ZnCo-porphyrin MOF nanosheet with atomically dispersed cobalt sites was synthesized, and it appeared to be a more efficient photocatalyst for CO_2 reduction than a mixture of Zn-MOF and Co-MOF. This was assigned to the enhanced charge transfer capacity and the increased lifetime of the photogenerated electron-hole pair. DFT calculations revealed that cobalt sites are favorable for receiving electrons from Zn porphyrin.[143]

Therefore, the utilization of nickel-based or cobalt-based 2D materials in photocatalytic applications is not only attributed to the beneficial conductive properties and to the strong binding energy with H_2 and CO_2, but also to the synergy with other metals; in this way, the overall photocatalytic performance of the materials can be enhanced. At the same time, the low dimensionality offers a shorter charge transport path and boosts light harvesting ability.

3.6. Electromagnetic Wave Shielding

The combination of ferromagnetic elements (M) with diamagnetic carbon has attracted a lot of interest. The ease of tuning both conductivity and magnetic properties by adjusting the M/C ratio renders these materials ideal candidates for electromagnetic wave (EW) absorption.[144–152] The technological progress and advancement of electronic devices are accompanied by electromagnetic waves that are a potential threat to human life and health. Therefore it is important to develop suitable materials for the absorption of electromagnetic waves and the attenuation of electromagnetic energy. These materials have to interact both with the electric and the magnetic field of the electromagnetic wave, as well as to deplete the energy of the wave and transform it into thermal energy.[153]

Aiming to enhance electromagnetic wave absorption, Liu et al. studied the effect of size and composition control of 2D layered C/Ni composites synthesized via a one-step calcination process. Strong electromagnetic wave attenuation property was granted by a combination of C with suitable amounts of Ni nanoparticles; in that report, nickel acetate was used as a precursor. Changing the amount of the Ni precursor can modulate the enhancement of the electromagnetic wave absorption performance (EMWAPs) of the C/Ni composite (Figure 10). As the amount increased, EMWAPs got enhanced until reaching the optimal result in n = 3.99 mmol; further increase did not have any positive effect on the maximum effective absorption bandwidth (EAB_{max}). Moreover, calcination temperature can affect the carbon content due to oxidation that may occur in higher temperatures; however, EMWAPs did not show any correlation with calcination temperature. In particular, the optimal calcination temperature is 600 °C, with 400 °C also yielding excellent results, while 500 and 700 °C are associated with extremely poor EMWAPs with a narrow EAB. This is attributed to different resulting sizes and compositions of the 2D C/N NP composites.[154] Similarly, 2D organic α-$Co(OH)_2$ exhibited good absorption properties, and it can be used as a precursor for Co/C composites as well. Those materials possess the same absorption properties and additional corrosion resistance together with wetting effect characteristics, which are very important for environmental applications.[155]

Among other features, dielectric loss, magnetic loss, and good impedance matching are required for good EW absorption properties. In the case of ferromagnetic elements, the 2D flake morphology improves magnetic anisotropy leading to enhancement of magnetic loss, thus to a desirable EW absorption.[156–159] 2D sponge-like Ni/derivatives prepared at 600 °C under hydrogen flow[157] and Co nanoflakes generated by low-temperature hydrothermal method[156] reinforce the above-mentioned observation and open the way for exploration of new EW absorption materials in 2D nanostructures composed of ferromagnetic elements. On top of that, Ji et al. investigated the capability of Fe_3GeTe_2 with ferromagnetism up to 230 K to absorb electromagnetic waves and alleviate microwave pollution and radiation. Even though Fe_3GeTe_2 fulfilled most of the requirements for EW absorption, it exhibited poor impedance matching. This drawback was tackled by introducing graphene nanosheets to the structure leading to a composite with significant microwave absorption performance.[160]

As a summary of this part, 2D materials based on ferromagnetic elements exhibit certain promising features for electromagnetic wave absorption. Still, their activity can be strengthened once they are integrated with carbon-based materials to form composites. The ratio between the ferromagnetic material and the carbon is a key aspect for controlling the conductivity and the magnetic properties of the composite: as a result, it can also affect the electromagnetic wave absorption performance. The morphology and thickness of the material have also a direct impact on its implementation as an electromagnetic wave absorbent.

3.7. Adsorption

Materials with a high specific surface area, such as 2D materials, are suitable for adsorption applications.[161] Recently, adsorption applications tend to use magnetic nanoparticles for water remediation, thanks to the ease of removal with the use of an external magnetic field.[162] Pollutants can be selectively attached onto magnetic materials, and the latter materials can be then magnetically separated, recycled and reused in industrial processes, effectively preventing the release of hazardous contaminants into the environment.[163] Consequently, the combination of ferromagnetic properties and 2D structures is anticipated to lead to adsorbents with enhanced capabilities and facile manipulation and removal by means of magnetic separation.

Materials of 2D and particularly metal oxides, are excellent candidates for adsorbing pollutants and dyes for water remediation

due to the high specific surface area along with the large number of active sites they can provide for adsorption.[164,165] Most of the time, calcination has a positive effect on their properties, while different calcination temperatures give rise to structurally different materials with varying specific surface areas, hence modified adsorption performances.[166,167] Studies suggest that calcination can improve material properties, but high calcination temperatures can lead to unwanted results. In 2D materials, high calcination temperatures cause the loss of the 2D structure and all the beneficial characteristics originating from it.[168] Galvani et al. fabricated 2D α-$Ni(OH)_2$ nanosheets via a microwave-assisted solvothermal method and converted them to NiO by calcination in a range of temperatures. Calcination up to 400 °C preserved the 2D morphology leading to NiO nanosheets, while 500 and 600 °C resulted in denser nanoparticles due to the collapse and agglomeration of the initial structure. Interestingly, calcination at 300 °C resulted in increased surface area and porosity accompanied by a better performance in Congo red adsorption, confirming that calcination temperature can affect both the morphology and adsorption capacity. Higher calcination temperature can cause pore widening, destroy the desired 2D structure and worsen adsorption properties.[169]

In the field of radioactive adsorption, many 2D materials have been successfully utilized.[170] 2D iron phosphate ($Fe_7(PO_4)_6$) was investigated by Wang et al. in three different forms, i.e., nanosheets, disks, and octahedrons for adsorption of hexavalent uranium (Figure 10). The nanosheets exhibited the largest surface area and thus better adsorption performance confirming that the two-dimensional morphology had a positive impact on the applicability of such materials on adsorption application. In addition, that study revealed that the active site of the material played a more critical role in the adsorption than its pores, contrary to expectations. It seems that U(VI) is trapped during the adsorption between the stacked and reorganized nanosheets. This phenomenon was named by the authors as Monolayer Surface Complexation and Stacking mode (MSCS-Mode).[171]

It is not the first time that the phosphate group[172–174] or 2D morphologies[174,175] have been used for U(VI) adsorption; nevertheless, 2D Fe phosphate stands out based on its adsorption performance by demonstrating 27 times better adsorption capacity than its 3D counterpart[173] and 2 times better capacity than phosphate functionalized graphene oxide,[174] confirming that 2D morphology and Fe presence are critical parameters in U(VI) adsorption performance.[171]

Overall, the low dimensionality of a given 2D material is the most critical parameter in what concerns its adsorption capability, followed by the nature of the metallic center and its morphology. Calcination temperature during material preparation can influence both dimensionality and morphology, affecting the resulting performance of the material.

3.8. Other Applications

2D materials based on ferromagnetic elements are also participating in other noteworthy applications. Such a case is cobalt telluride ($CoTe_2$) synthesized by vacuum induction melting and exfoliated by sonication-assisted liquid exfoliation method to obtain 2D sheets. The bulk material with 1T metallic phase transformed to a 2D sheet 1H semiconductor phase with the lateral dimension of the sheet being rectangular, ranging from 100 to 200 nm. The 2D $CoTe_2$, besides the flexibility and the high surface-to-volume ratio endowed by its 2D structure, exhibited a temperature-dependent behavior as well as piezoelectric and triboelectric properties; these factors can improve energy conversion of a piezo-triboelectric nanogenerator (PTNG) (**Figure 11**). In particular, the authors demonstrated the capability of this material to harvest waste-heat energy from an electronic device such as a laptop by attaching it underneath, where the overheating occurs. The fabricated PTNG, as a response to the elevated temperature being present under the laptop, increased the output voltage with a linear correlation. Based on that, the PTNG device can also be used for temperature monitoring in electronic devices, taking into consideration the device weight due to the observed PTNG sensitivity to the weight of the laptop.[176]

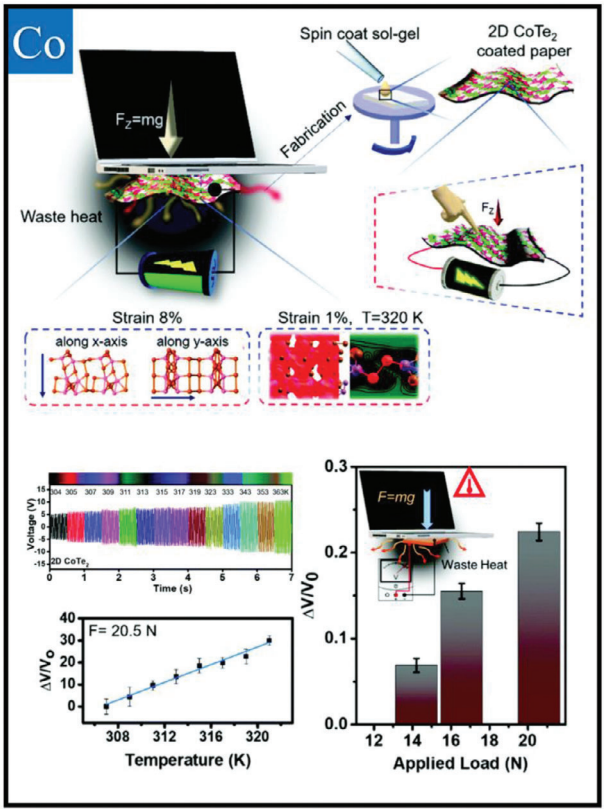

Figure 11. Schematic representation of the energy harvesting concept of piezo-tribo generator utilizing 2D $CoTe_2$. Graphs depicting: open circuit voltage response as a function of temperature, relative voltage changes of the $CoTe_2$ cell at various temperatures, and relative voltage changes of the cell in relation to the applied load for sensing the temperature of the laptop. Reproduced with permission.[176] Copyright 2022, Royal Society of Chemistry.

Furthermore, 2D materials are interesting candidates for plasmonic devices thanks to the variety of physical, chemical and structural properties they hold and their ease of being adjusted depending on the desired application.[177] Even more intriguing is the use of 2D magnetic materials, which enable light manipulation by applying an external magnetic field.[178] Comparison of Ni films with 2D Ni nanodot arrays on indium tin oxide (ITO)

substrate demonstrated UV–vis spectra with a maximum of 437 and 400 nm, respectively. Ni nanodot arrays were deemed suitable for plasmonic devices, with the results suggesting that the localized surface plasmon resonance (LSPR) maximum peak is not sensitive to the size of the Ni nanodots.[179]

4. 2D Materials Doped With Ferromagnetic Elements

In the efforts to obtain 2D materials with distinctive optical and electrical properties, approaches such as doping, strain, and chemical functionalization have been utilized aiming to tune the band alignments of the materials. Doping, which is the intentional introduction of foreign elements into a material, plays a significant role in functionalizing 2D materials by changing the intrinsic properties of pristine atomic layers. Examples include, among others, the ferromagnetic atom (e.g., Fe, Co, and Ni)-doped 2D TMDs referred as 2D-diluted magnetic semiconductors (DMS), whereas many of these materials have been predicted to exhibit ferromagnetic behavior at room temperature.[180]

In the last few years, the magnetic properties of pure 2D materials and magnetic element-doped 2D materials have been extensively investigated both theoretically and experimentally. Doping with a single element into low-dimensional materials has proven to promote room-temperature ferromagnetism, which is also supported by theoretical investigations.

Martinez and co-workers explored the impact of doping with the common ferromagnetic elements and manganese which is an antiferromagnetic element in low temperatures. In particular, these researchers studied the magnetic and electrocatalytic properties of hydrothermally grown transition metal-doped (10% of Co, Ni, Fe, and Mn) 2H-MoS_2 nanocrystals (NCs) with a particle size of 25–30 nm. Pristine 2H-MoS_2 NCs showed a mixture of antiferromagnetic and ferromagnetic behavior. While Co, Ni, and Fe-doped MoS_2 nanocrystals demonstrated room-temperature ferromagnetism, Mn-doped MoS_2 NCs displayed a paramagnetic behavior at room temperature. This indicated that magnetic properties were strongly dependent on the nature of the dopant while the magnetic order-disorder transition varied with dopant type (Co- and Ni-doping produced stronger ferromagnetic behavior than Fe- and Mn-doping). In order to study electrocatalytic performance for hydrogen evolution reaction, polarization curves were measured for undoped and doped MoS_2 NCs. At an overpotential of $\eta = -300$ mV, the current densities were $FeMoS_2$ > $CoMoS_2$ > MoS_2 > $NiMoS_2$ > $MnMoS_2$ and the catalytic activity based on Tafel slopes was $CoMoS_2$ > MoS_2 > $NiMoS_2$ > $FeMoS_2$ > $MnMoS_2$. The authors believe that the increasing number of catalytically active sites in $CoMoS_2$ NCs might be responsible for their superior electrocatalytic activity. Thus, the catalytic activity can be modulated by choosing suitable dopants in NCs of 2D materials.[181]

4.1. Fe-Doping

Xia and co-workers produced 2D MoS_2 nanosheets doped with Fe ions via a hydrothermal method. Magnetic hysteresis (M-H) curves measured under different temperatures suggested that robust ferromagnetism occurred in the Fe-doped MoS_2 nanosheets, which exhibited a high Curie point (>930 K). The magnetic moment mainly arose from the Fe atoms, while ferromagnetism can be effectively adjusted by changing the Fe-doping concentration. In this way, potential applications of Fe-doped MoS_2 nanosheets in spintronic devices were envisaged (**Figure 12**).[182]

Fu et al. performed an in situ substitutional Fe-doping into MoS_2 monolayers via low-pressure chemical vapor deposition (CVD). Iron atoms substituted molybdenum sites in MoS_2, as confirmed by TEM and Raman. The authors uncovered a Fe-related spectral transition of Fe:MoS_2 monolayers that appears at 2.28 eV above the pristine band gap and displayed pronounced ferromagnetic hysteresis. The microscopic origin was further corroborated by DFT calculations of dipole-allowed transitions in Fe:MoS_2. Also, by using spatially integrating magnetization measurements and spatially resolving nitrogen-vacancy center magnetometry, the authors showed that Fe:MoS_2 monolayers remained magnetized even at ambient conditions, manifesting room-temperature ferromagnetism (Figure 12).[183]

Wang and co-workers prepared undoped and Fe-doped MoS_2 layered crystals via a chemical vapor transport method. Optical behaviors of carrier transitions were observed successfully in both undoped and Fe-doped MoS_2 samples using reflectance and piezo-reflectance. The Fe-doped MoS_2 sample was evaluated by frequency-dependent photoconductivity measurements, revealing an additional Fe doping level and a longer carrier lifetime compared to the undoped sample. Hall measurements for both samples indicated that the doped sample exhibited a higher carrier concentration and lower mobility due to the Fe dopants. Both samples were confirmed to have n-type carriers.[184] Kang et al. showed that substitutional Fe-doping of MoS_2 and WS_2 monolayers induces different magnetic properties. Fe-doped monolayers were directly synthesized via CVD. While both Fe:MoS_2 and Fe:WS_2 showed photoluminescence quenching and n-type doping, Fe dopants in WS_2 monolayers were found to assume deep-level trap states, in contrast to Fe:MoS_2, where the states were identified as shallow. Using μm- and mm- precision local (nitrogen-vacancy) NV-magnetometry and (superconducting quantum interference device) SQUID magnetometer, the authors revealed that, unlike MoS_2 monolayers, WS_2 monolayers did not experience a magnetic phase transition to ferromagnetism upon Fe-doping. The absence of ferromagnetism in Fe:WS_2 was corroborated using DFT calculations.[185]

Li et al. developed a Fe-doped SnS_2 monolayer exfoliated using a micromechanical cleavage method. Fe atoms were doped at the Sn atom site (Fe contents were ≈2.1%, 1.5%, and 1.1%). Field-effect transistors based on the $Fe_{0.021}Sn_{0.979}S_2$ monolayer showed n-type behavior and exhibited high optoelectronic performance. Magnetic measurements illustrated that pure SnS_2 was diamagnetic, whereas $Fe_{0.021}Sn_{0.979}S_2$ exhibited ferromagnetic behavior with a perpendicular anisotropy at 2 K and a T_C of ≈31 K. DFT calculations showed that long-range ferromagnetic ordering in the doped sample was energetically stable, and the estimated T_C agreed well with experimental findings suggesting that Fe-doped SnS_2 sample will have excellent performance for optoelectronic devices.[180] Hu et al. synthesized few-layer VSe_2 nanosheets with room-temperature ferromagnetism by a high-temperature organic solution-phase method. To further improve the magnetic properties, Fe was used and doped into the VSe_2, leading to the formation of $V_{1-x}Fe_xSe_2$ nanosheets with enhanced

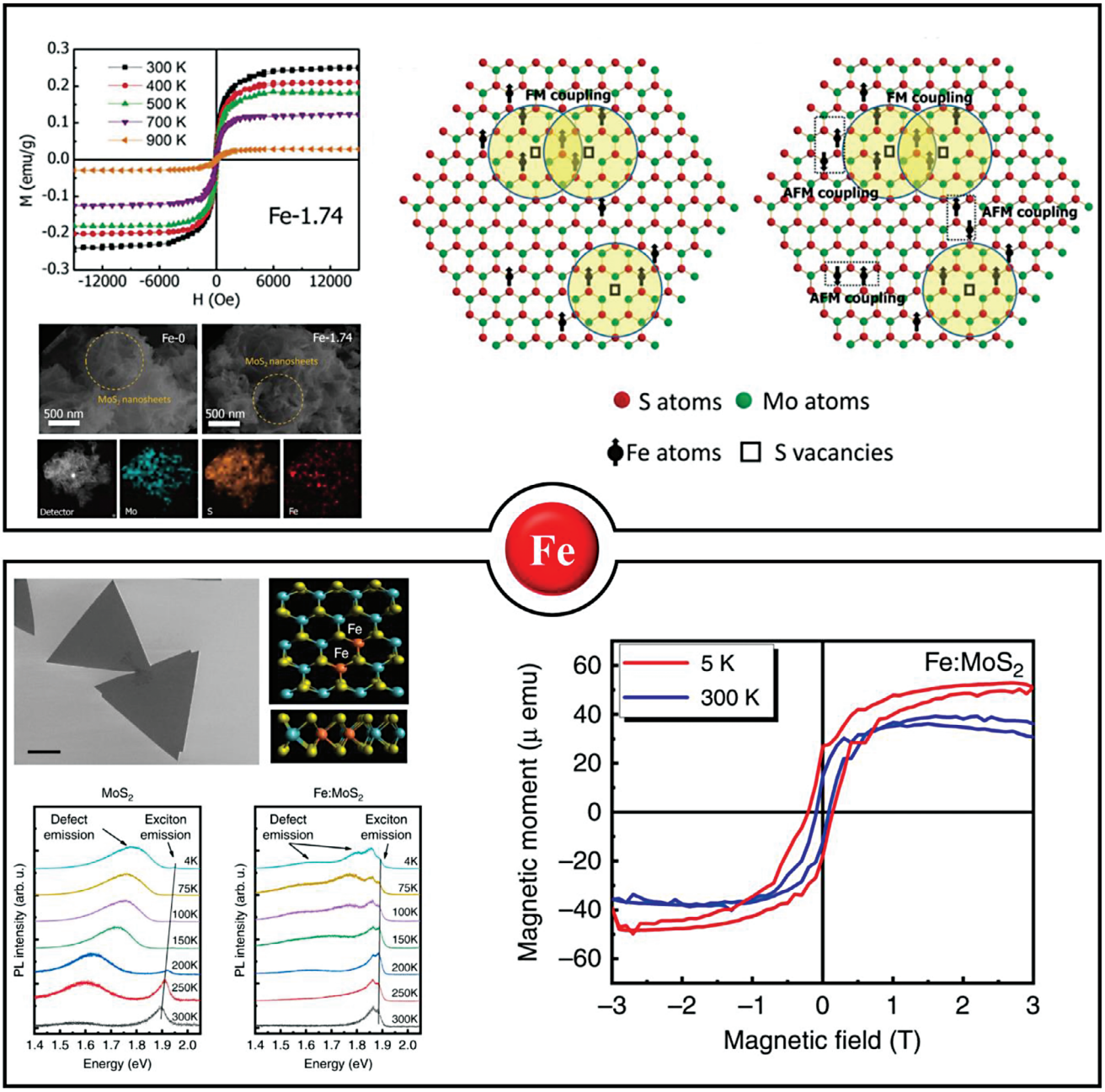

Figure 12. (Top) hysteresis loops for Fe-doped MoS_2 measured at 300-900 K, SEM images depicting the morphology of undoped MoS_2 (Fe-0) and Fe-doped (Fe-1.74) and EDS mapping of the Fe-doped MoS_2, schematic illustration of bound magnetic polarons (BMPs) in Fe-doped MoS_2, emphasizing on ferromagnetic coupling (left) and antiferromagnetic coupling that occurs in high doping concentrations (right). Reproduced with permission.[182] Copyright 2017, The Japan Society of Applied Physics; (bottom) SEM images of as-grown Fe:MoS_2 monolayer and schematic top view of the monolayer (yellow spheres are sulfur and blue spheres represent molybdenum), temperature-dependent photoluminescent spectra for MoS_2 and Fe:MoS_2 and hysteresis loops (M-H) of Fe:MoS_2 in cryogenic and room temperature conditions. Reproduced with permission.[183] Copyright 2020, Nature Communications.

room temperature coercivity and magnetization without damaging the layered structure. This enhancement was attributed to the coupling interaction of 3d orbitals between V and Fe atoms, while higher Fe concentrations improved coercivity due to the formation of a second phase, Fe_3Se_4.[186]

Nazir et al. prepared antiferromagnetic $MnSe_2$ nanosheets through hydrothermal synthesis and studied the effect of Fe and Co doping on the magnetic and optical properties. The strong antiferromagnetic behavior of $MnSe_2$ was decreased in the case of the Fe and Co-doped nanosheets, rendering the material more suitable for spintronic applications. As for the optical properties, a band gap narrowing was observed in the doped materials, which will benefit their use in photocatalysis or photovoltaics.[187]

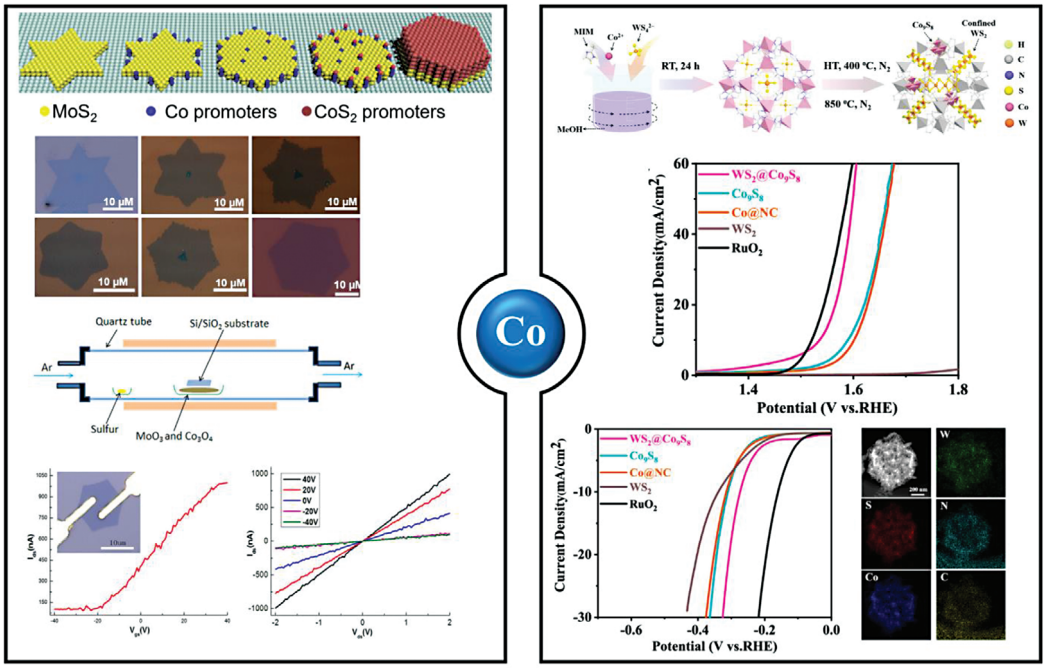

Figure 13. (Left) simulation and optical images demonstrating the effect of sulfur on the morphology of $Co_xMo_{1-x}S_2$, schematic illustration of the setup configuration for the material preparation, electrical transport properties of $Co_xMo_{1-x}S_2$ nanosheetsfield effect transistor (FET) devices with 2 V applied bias voltage and current-voltage curves at varied back gate voltage (V_{gs}). Reproduced with permission.[190] Copyright 2015, American Chemical Society; (right) schematic illustration of the synthesis process of $WS_2@Co_9S_8$, LSV polarization curves exhibiting electrocatalytic performance of the material in 1 M KOH towards OER and HER and STEM image along with STEM elemental mapping images. Reproduced with permission.[191] Copyright 2022, American Chemical Society.

In another study, Sun et al. reported on the Fe-doped $(Ti_{1-x}\ Fe_x)_3AlC_2$ (x = 0, 0.025, 0.05, 0.075) MAX phase with ferromagnetic state at low temperature, which turns into paramagnetic after exfoliation and delamination in the $(Ti_{1-x}\ Fe_x)_3C_2T_\delta$ 2D MXene counterparts. This behavior was attributed to the broken exchange coupling along the c-axis resulting from the etching away of the Al layer. Nevertheless, the 2D MXene counterpart after Fe doping (x = 0.025) demonstrated a good electromagnetic shielding performance in the wide frequency range of 5.8-26.5 GHz, thanks to the improvement of intrinsic conductivity that Fe offers to the MXene.[188]

Based on the above-mentioned studies, doping with Fe has the potential to i) introduce long-range ferromagnetism in non-magnetic materials like MoS_2, as well as ii) enhance the ferromagnetic properties of already magnetic 2D materials, such as VSe_2, while iii) increasing their Curie point. The concentration of Fe-doping proved to be a critical parameter in adjusting magnetic properties, with an elevated concentration being favorable. Additionally, Fe-doping can improve the electrocatalytic, optical, and conductive properties of 2D materials.

4.2. Co-Doping

Due to its distinctive layer structure and electronic properties, the inorganic fullerene-like structure of MS_2 (where M = Mo, W) has been attracting considerable attention in what concerns both its nanoscale and bulk form. Such materials have been investigated extensively for various applications. In particular, WS_2 and MoS_2 nanomaterials find applications in fields such as scanning probe microscopy (SPM), solid-state lubricants, heterogeneous catalysis, and electrochemical hydrogen storage. As important 2D-DMS, Co-doped monolayer, Fe-doped monolayer, and bilayer/multilayer MoS_2, among others, have been studied by theoretical calculations.[189]

Li and co-workers synthesized large-scale 2D $Co_xMo_{1-x}S_2$ (x = 0.16) hexagonal bilayer nanosheets using the CVD method (**Figure 13**). As the initial loading of the sulfur increased, the morphology of the $Co_xMo_{1-x}S_2$ ($0 < x < 1$) nanosheets turned step by step from David-star's shape to hexagons at 680 °C. Co atoms were mainly distributed at the edge of nanosheets. At 750 °C, high-quality cubic pyrite-type crystal structure CoS_2 grew on the surface of the $Co_xMo_{1-x}S_2$ nanosheet, and a hexagonal film was formed, which was induced by the presence of the nanosheet. Electrical transport measurements on nanosheets confirmed the typical n-type transport behavior. CoS_2 film exhibited a half-metallic behavior with a conductivity of about 8×10^4 s m^{-1}. These findings strengthen the idea that $Co_xMo_{1-x}S_2$ nanosheets can find potential applications in tunable optoelectronics.[190]

In another work, Xiang et al. synthesized MoS_2 nanosheets via a hydrothermal approach with varying Co-dopant concentrations (0, 3, and 7%). The thickness and flatness of the nanosheets increased by enhancing the cobalt concentration. Magnetization measurements showed that the values of the magnetic moment decreased with the increase of the Co-dopant concentration, an evidence that was corroborrated by DFT calculations as well. Change of the magnetic moment involves two main factors in

the nanosheets: i) the reduced moment upon substitution of one Mo on the Mo edge by Co, which can be attributed to the coupling of the Co moment to the edge state, and ii) ferromagnetism possibly originating from a decrease of zigzag edges, with associated magnetism at grain boundaries.[192]

Xia and co-workers proposed a simple and efficient method for the synthesis of few-layered WS_2 nanosheets anchored on a Co, N-doped carbon hollow polyhedron (namely, Co-based zeolite imidazole framework (ZIF-67)) (Figure 13). A coordinated bifunctional catalyst of $WS_2@Co_9S_8$ exposing a large number of active sites was obtained by one-pot mixing and subsequent calcination. As Co_9S_8 tends to agglomerate at high temperatures, a few-layered WS_2 grown on the surface of Co_9S_8 was obtained. Therefore, the combination of the hollow nanopore structure of the MOF and the active metal center with the WS_2 nanosheet helped to achieve a uniform functionalization of the MOF surface; as a result, the catalytic activity for OER and HER was significantly boosted. Therefore, the robust catalyst ($WS_2@Co_9S_8$) prepared by a simple and efficient synthesis method in this work can serve as a highly promising bifunctional catalyst.[191] Additionally, 2D cobalt/nitrogen (Co/N) co-doped porous carbon nanosheets were prepared by Hou et al. as catalysts for ORR in both basic and acidic conditions by employing cobalt porphyrin-based 2D conjugated microporous polymer as a precursor, using functionalized graphene as a 2D template by direct pyrolysis. The as-prepared nanosheets exhibited typical 2D morphology, high specific surface areas and uniform Co/N co-doping feature. Benefiting from these characteristics, the prepared nanosheets displayed a remarkable electrocatalytic performance for ORR in basic conditions (0.1 M KOH, $E_{1/2} = -0.146$ V versus Ag/AgCl and four-electron transfer mechanism) as well as in acidic ones (0.5 M H_2SO_4, $E_{1/2} = 0.54$ V versus Ag/AgCl). The authors attributed this behavior to the high activity of CoN_x active sites among the conjugated microporous polymer nanosheets. They also claim that such materials can find promising applications in fuel cells and metal-air batteries and open up new avenues for metal/heteroatom co-doped porous carbon materials with promising performance for energy storage and conversion.[193] Shao et al. synthesized Co-doped BiOBr (010) by a hydrothermal route and studied it through DFT calculations. Cobalt doping led to an enhanced charge separation efficiency and an expanded light absorption region, with the theoretical calculations revealing an additional energy level inserted into the band gap of Co-doped BiOBr. Its conduction band bottom (CBM) and valence band top (VBM) shifted toward lower energy regions. The photocatalytic performance of the material was tested over the photocatalytic degradation of tetracycline hydrochloride with results revealing an 83% degradation within 30 min.[194] Later on, Wang et al. exploited the photocatalytic features deriving from Co doping by constructing a thiourea-modified 2D/2D cobalt-doped $(BiO)_2CO_3$/BiOCl heterojunction (Co-$(BC/BL)_{Tu}$) by a one-pot hydrothermal method. The produced composite displayed an excellent photocurrent response and an enhanced charge separation efficiency that benefitted its use in photocatalytic applications. The Co-$(BC/BL)_{Tu}$ was also applied in the visible-light driven photodegradation of tetracycline hydrochloride, with the results revealing an outstanding performance as illustrated by the photodegradation rate constant being 5.2 times higher than $(BiO)_2CO_3$. The cobalt doping combined with the 2D/2D structure and the type II heterostructures contribute to enhanced photocatalytic performance and suggest a promising strategy for constructing a highly effective photocatalytic system.[195]

Kadam et al. synthesized a WS_2/WO_3 composite doped with 5% Fe, Co, and Ni by a colloidal method and studied the effect of the doping elements in the catalytic performance in HER. The doped materials maintained the flower-like morphology of the pristine material, which provides multiple interfaces and abundant edges in the composite rendering it a promising electrocatalyst. Among the ferromagnetic elements tested, the Co-doping led to improved HER performance for the resulting material with an overpotential at 10 mA cm^{-2} of 321 and 337 mV in acidic and alkaline media, respectively. The Ni-doped counterpart had an overpotential of 354 and 364 mV, whereas the Fe-doped material exhibited an overpotential of 357 and 410 mV in acidic and alkaline conditions at the aforementioned current density.[196]

Furthermore, Chen et al. constructed cobalt-doped 2D graphene-coupled hyper-crosslinked porous polymer nanosheets (Co-GHCP) using a nucleophilic substitution reaction prepared via reversible addition fragmentation chain-transfer (RAFT) emulsion polymerization with the macromolecular chain-transfer agent of GO-DDAT. Co-GHCP transformed into cobalt-doped porous carbon nanosheets (Co-GPC) through direct pyrolysis treatment possessing a typical 2D morphology with a high specific surface area. These intriguing properties of transition metal-doping, high conductivity, and porous structure endow the Co-GPC with great potential applications in energy storage and conversion.[197]

In the case of Co-doping, its impact on magnetic properties is lower than that of Fe, but it certainly cannot be neglected. Moreover, cobalt atoms at the edges of the 2D materials introduce additional metallic active sites that enhance electrocatalytic and photocatalytic properties, thus rendering the doped material ideal for energy applications. It has to be noted that Co-doping can affect the thickness and/or morphology of a given material, by controlling the growth rate of the material in different directions.

4.3. Ni-Doping

Materials of combined ferromagnetic and semiconducting nature, preferably at room temperature, are of great interest. Nickel (Ni^{2+}), due to its exceptional chemical stability, is also recognized as one of the most efficient doping elements to improve and/or tune the electrical properties of different materials.

Han et al. prepared Ni-doped vanadium selenide by in-situ growth on reduced graphene oxide (rGO) via a one-pot solvothermal route. The formed 2D composite Ni-VSe_2/rGO exhibits high conductivity and improved adsorbing and catalytic activity, which benefit its use in energy storage applications. In particular, this material served as a modified functional separator in lithium-sulfur (Li-S) batteries thanks to its significantly improved adsorbability to soluble lithium polysulfides (LiPSs) and the increased electrocatalytic activity toward sulfur conversion reactions. As a result, the Li-S cell with the Ni-VSe_2/rGO modified separator has a high specific capacity of 510.3 mA h g^{-1} after 1190 cycles at 0.5 C.[198]

Wei et al. synthesized 2D Ni-doped MoS_2 nanosheets via a one-step electrochemical exfoliation strategy with high electrical

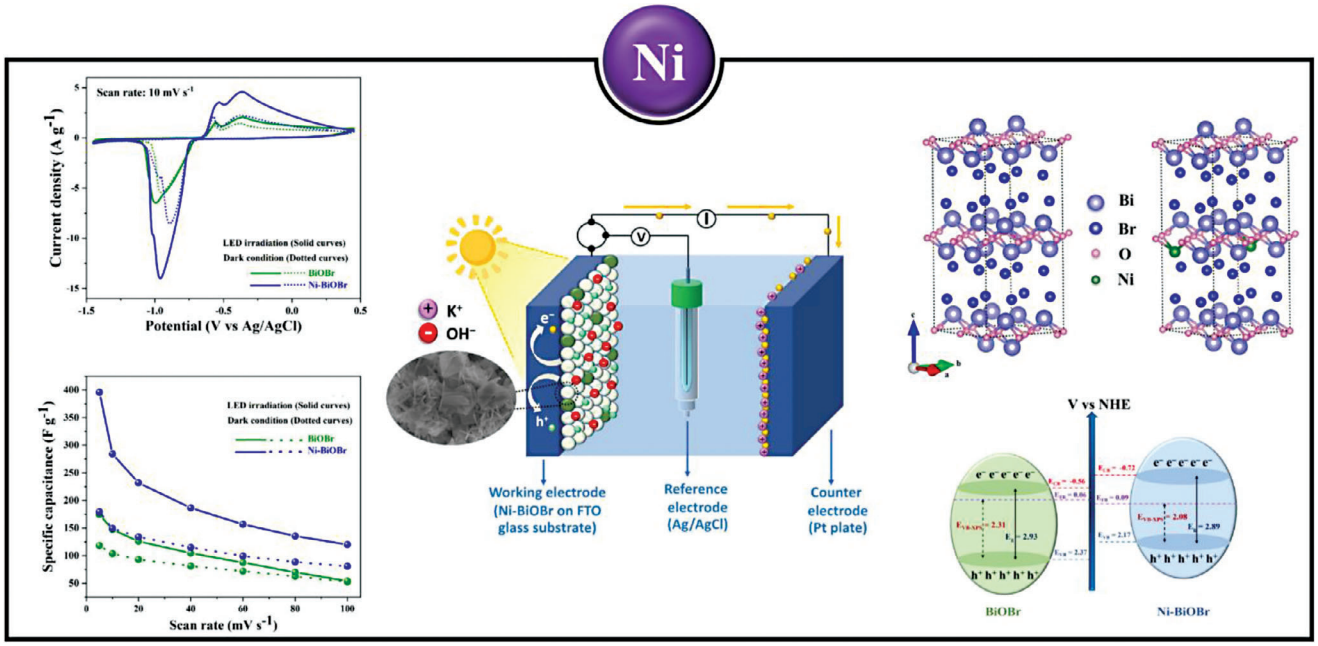

Figure 14. Graphs depicting cyclic voltammetry (CV) curves, and specific capacitance as a function of scan rate of BiOBr and Ni-BiOBr with and without LED irradiation. Schematic mechanism of the electron-hole pairs under LED for energy storage of Ni-BiOBr, crystal structure models and band structure diagrams of BiOBr and Ni-BiOBr. Reproduced with permission.[202] Copyright 2023, Elsevier.

conductivity and abundant exposed active sites deriving from the formation of stable 1T/2H phase-MoS_2 heterojunction. The 2D Ni-doped MoS_2 was utilized as a HER electrocatalyst in alkaline media with a low overpotential of 145 mV at 10 mA cm^{-2} and a Tafel slope of 89 mV dec^{-1}. It was also employed as cathode for Zn-H_2O battery displaying a high power density of 3.3 mW cm^{-2} with excellent stability. XPS before and after HER process revealed an increase in the binding energy of Ni 2p implying a higher valence state of Ni species in the Ni-doped MoS_2; at the same time, Ni 2p had a positive shift of 0.5 eV which is indicative of electrons transferred from the Ni center to the adjacent H_2 molecules; thus, Ni species served as the main active center for HER.[199]

Wang et al. designed and fabricated a 2D/2D Ni-doped $CsPbBr_3/Bi_3O_4Br$ Z-scheme heterojunction through an electrostatic self-assembly strategy and studied the photocatalytic CO_2 conversion performance. Both experimental results and theoretical calculations confirmed that Ni doping in $CsPbBr_3$ efficiently expands spectral response, while it is at the same time favorable for the adsorption and activation of CO_2. The Ni-doped $CsPbBr_3/Bi_3O_4Br$ exhibited superior CO evolution performance under CO_2 atmosphere with a yield of 387.57 μmol g^{-1}, which is about 12.3 and 3.7 times higher than the pure $CsPbBr_3$ and Bi_3O_4Br, respectively.[200] Kumar et al. fabricated few layered Ni-doped MoS_2 nanosheets by liquid phase exfoliation and deposited the product onto CdS nanorods. The Ni-doped MoS_2 upgraded the photocatalytic activity of CdS for hydrogen production leading to a yield of 249 mmol h^{-1} g^{-1} which is 70 times higher than pure CdS. The presence of metal doping, such as Ni, had positive effects on conductivity, surface area, and the presence of active sites. At the same time, the Ni and Mo sites in Ni-MoS_2 are able to enhance the kinetics of the catalytic reaction, as evidenced by their strong water dissociation activity and constant hydrogen adsorption ability.[201]

Khampunbut et al. fabricated Ni-BiOBr nanosheets through one-step precipitation at ambient conditions. The designed BiOBr lattice with Ni^{2+} insertion resulted in a decrement in band gap energy, expecting that Ni-BiOBr can increase visible light absorption and enhance the supercapacitor performance (**Figure 14**). Once illuminated under UV light, Ni-BiOBr photoelectrode delivered the highest specific capacitance (362.73 F g^{-1} at 0.5 A g^{-1}), which is 1.45 times larger than that of dark condition. In addition, the asymmetric supercapacitors of Ni-BiOBr/reduced graphene oxide (rGO) offered an energy density of 39.95 Wh kg^{-1} at a power density of 725 W kg^{-1} and maintained 68% capacitance retention at 5 A g^{-1} after 1000 cycles under light irradiation. Thus, this work presents a class of materials for photo-assisted charging supercapacitors, utilizing solar energy to enhance storage capacity.[202] Azor et al. reported a synthetic pathway of high oxidation state lamellar cobalt oxides with thicknesses of only a few atom layers. The nanosheets preserved high oxidation states Co^{3+} and Co^{4+} which are of high interest for electrocatalysis of the OER. By combining a high Co oxidation state, surface-to-volume ratio and optimized Ni substitution, the nickel-doped sodium cobaltite 2D nanomaterials exhibited high OER electrocatalytic activity and stability in alkaline aqueous electrolyte comparable to standard materials obtained in harsh thermal conditions.[203]

In a similar manner to cobalt, the insertion of Ni-doping brings about metallic active sites that benefit adsorption and catalytic properties. It has been observed that 2D materials doped with Ni exhibit higher electrical conductivity and improved electrocatalytic performance. Consequently, the utilization of such materi-

als in supercapacitors and other energy storage devices is considered to be highly advantageous.

5. Proximity Effect Of Ferromagnetic Elements

The existence of intrinsic magnetism in organic materials has been very controversial, with the purity of the material being critical. Even though several studies claim that graphite or other forms of carbon have inherent ferromagnetic properties, in most cases, these properties were attributed to ferromagnetic impurities.[204–206] It is well known that magnetic moments have their origin in the presence of unpaired d and f electrons, while graphene, similar to every carbon system with sp, sp^2, and sp^3 hybridization, lacks unpaired electrons.[207–209] Therefore, due to the lack of unpaired electrons, graphene is known as a pure diamagnet.[210,211] Nevertheless, there is a need for the induction of ferromagnetism to become applicable in the domain of spintronics.[20,212]

Some studies suggest that the presence of structural defects,[213–215] epoxy groups,[216] or the mixed sp^2-sp^3 hybridization[217] can lead to intrinsic ferromagnetism in carbon-based materials such as graphene oxide,[218] without the presence of modifications or the need of fluorination.[219] In one way or another, the great electrical properties of graphene are negatively affected. To surpass this main drawback, scientists induced ferromagnetism in graphene by attaching it to magnetic materials and demonstrating the quantum anomalous Hall effect.[220] This effect originates from the exchange interaction and spin-orbit coupling between the magnetic and the non-magnetic material.[221]

The induced ferromagnetism into an intrinsically non-magnetic material such as graphene caused by an adjacent ferromagnet is called the proximity effect or proximity-induced ferromagnetism.[221] The atomic scale thickness of graphene and other 2D materials favors the proximity effect.[222]

The proximity effect arises from either a continuous ferromagnetic insulator layer[221,223,224] or a discontinuous magnetic structure, like magnetic nanoparticles,[225,226] without much difference in exchange coupling. Interestingly, proximity-induced ferromagnetism is capable of modulating the spin current by controlling the direction of the exchange field, while the externally applied field alone cannot cause significant spin precession.[227]

Graphene has zero band gap and unsaturated p_z orbitals; both properties are important for electronic interaction with 3d orbitals. The hybridization in carbon p_z and ferromagnet d_z orbitals is very strong due to symmetry matching and their spatial overlap (**Figure 15**). Additionally, d_{zx} and d_{zy} orbitals can also interact with p_z because they have an out-of-plane component that overlaps with p_z.[224] These interactions between different orbitals of adatoms and graphene can induce spin-polarization and, thus, magnetic moment.[221]

Many scientists took advantage of the proximity effect and studied the magnetic properties of carbon induced by adjacent ferromagnetic atoms. In particular, multiwall carbon nanotubes in contact with a flat cobalt-substrate lead to a spin transfer of 0.1 μB per carbon atom,[228] and the Fe presence in the C/Fe multilayer system induces a magnetic moment of 0.05 μB in carbon atoms.[229] Both cases of carbon magnetism are influenced by the adjacent ferromagnetic atom and are related to the strong chemical interaction involving $3d_z^2$ and C p_z electrons and the spin polarization of the C p_z orbitals.[230] Later on, Weser et al. confirmed the induced magnetism in carbon atoms at a 2D graphene layer on a nickel (111) substrate and estimated the magnetic moment of carbon atoms somewhere between 0.05 and 0.1 μB[231] based on the aforementioned examples.[228,229]

Cobalt atoms in the graphene interface can induce ferromagnetism due to charge transfer, with the observed coercivity being 516 Oe in a temperature as low as 2 K. As the temperature increases, the coercivity of graphene decreases to 8 Oe at 50 K.[232] However, in the presence of nitrogen, cobalt atoms are attached better in graphene lattice and enhance the conductivity of the systems because of the additional p electron N possesses. Therefore, nitrogen not only assists Co-N_4 moiety-doped graphene to reach the Stoner criterion but also maintains a stable ferromagnetic ordering in graphene with a Curie point of ≈400 K.[233,234]

Diamagnetic multilayer graphene demonstrated enhanced magnetic properties after coating with cobalt ferrite ($CoFe_2O_4$) nanoparticles due to the proximity effect. In particular, the saturation magnetization of the composite increased in comparison with pure $CoFe_2O_4$, while the coercivity field decreased. Additionally, magnetic force microscopy (MFM) images revealed larger magnetic domains in the composite than in the $CoFe_2O_4$ due to the uniform size distribution of the nanoparticles.[235]

The Co-rGO nanohybrid demonstrates increased remanent magnetization and coercivity in comparison with Co nanoparticles but lower saturation magnetization. This is due to the strong electronic interaction and charge transfer between rGO and Co.[226]

Abtew et al. studied the effect of a single layer of graphene adsorbed on nickel (111) and cobalt (111) surfaces with various layers/thicknesses (Figure 15). When graphene was adsorbed on a single metallic layer of Ni and Co, the charge transfer was calculated to be 0.035e per C atom and 0.040e per C atom, respectively. Interestingly, the interfacial interactions are not limited only to the first layer, so in a 12-layer Ni and Co surface, charge transfer increased to 0.07 e and 0.05 e per C atom, respectively. Accordingly, as the layers of the ferromagnetic substrate increase, the induced magnetic moments in graphene-Ni (111) increase from 0.54 to 0.72 μB per atom, and graphene-Co (111) increase from 1.59 to 1.81 μB per atom. Concomitantly, the magnetic moments of the top ferromagnetic layer decrease by ≈20% for Ni and 10% for Co. This effect has been proven that is not relative to the thickness and cannot affect the inner layers of the substrate.[224]

Theoretical studies compared the various metal adatoms adsorbed on graphene by ab initio calculations; as an outcome, it turns out that probably the ferromagnetic elements (Fe, Co, Ni) have higher charge transfer and stronger adatom-graphene bonds relative to other elements, but both the magnetic moment of the system and of the isolated atoms is lower than the antiferromagnetic elements (Cr, Mn).[236] Surprisingly the magnetic moment of the Ni-graphene system was calculated to be zero, contradictory with studies showing that the graphene-nickel system has a non-zero magnetic moment.[224]

Graphene/ferromagnet systems are highly applicable in any kind of spintronic device because of their electronic, magnetic, and interfacial properties.[237] Even more importantly, they open up new possibilities through the design of

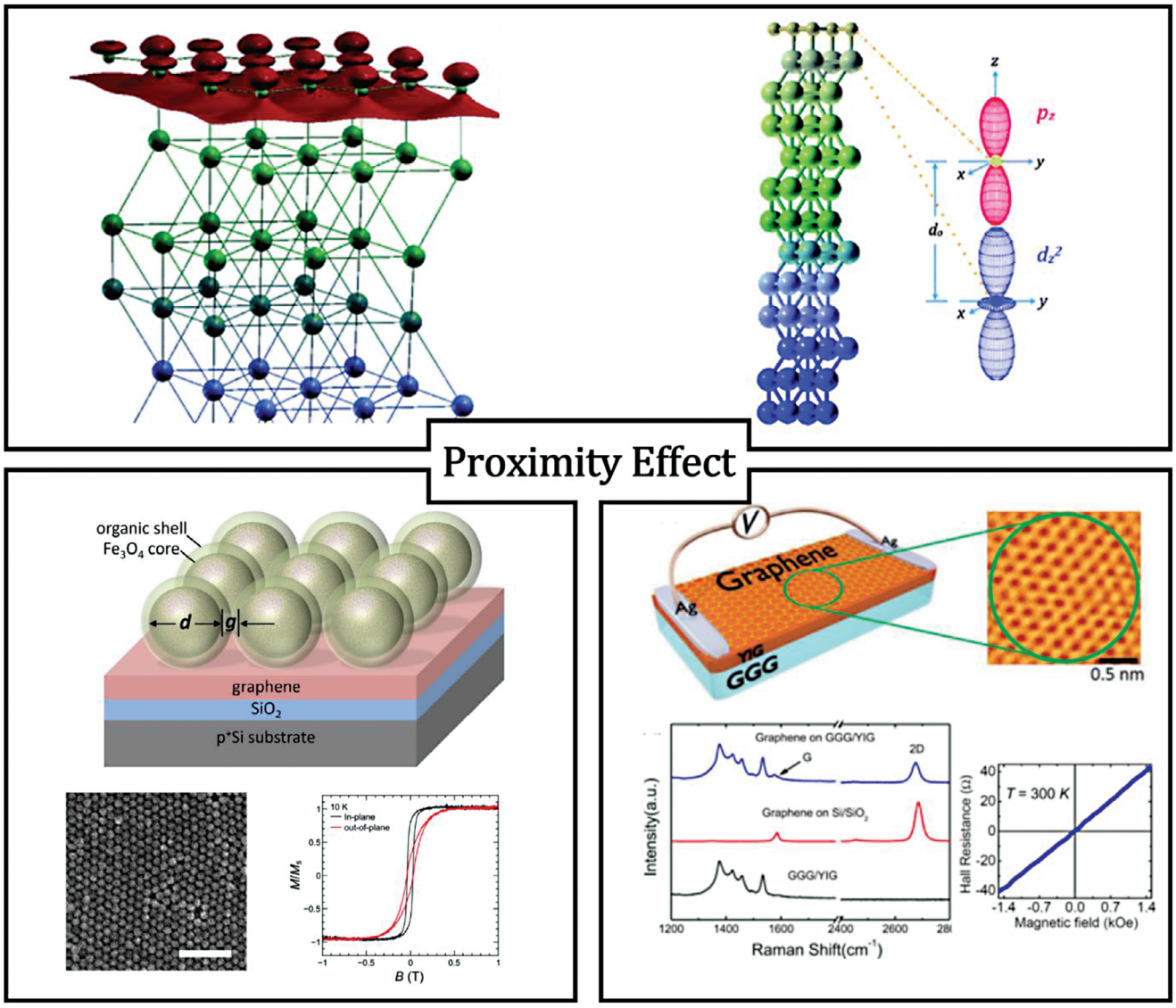

Figure 15. (Top) schematic illustration of isosurface plot of the charge density difference between graphene and Ni, schematics of the out-of-plane C-p_z and transition metals d_z^2 orbitals, where d_0 is the interlayer spacing between the C atom and the top Ni (Co) atom. Reproduced with permission.[224] Copyright 2013, The Royal Society of Chemistry; (bottom-left) schematic illustration of proximity effect of graphene with magnetic nanoparticles, SEM image of close-pack magnetic nanoparticles and hysteresis loop B-H for in-plane and out-of-plane directions of the sample. Reproduced with permission.[225] Copyright 2019, American Chemical Society; (bottom-right) scheme representing the YIG/graphene structures and the configuration used for dc voltage measurements, STM image showing the surface detail. Raman spectra of GGG/YIG, SiO_2/graphene, and GGG/YIG/graphene and low magnetic field dependence of the Hall resistance at room temperature. Reproduced with permission.[221] Copyright 2019, American Physical Society.

desirable properties by modifying the thickness of the ferromagnetic substrate[224] or the direction of the exchange field.[227]

Chau et al. exploited the proximity effect to detect two-dimensional ferromagnetism. In particular, they coupled monolayer graphene with 2D ferromagnet $Cr_2Ge_2Te_6$ (CGT) and monitored the modification of the graphene properties arising from the magnetic-proximity effect of CGT. These results indicated that graphene could sense the magnetic phase transition of the CGT layer and foresee the development of electrical platforms based on graphene heterostructures exploring various phases in magnetic insulators.[238]

Based on the above-mentioned examples, proximity-induced ferromagnetism has been extensively studied in graphene. However, it does not constitute an exclusive property of graphene derivatives as there are several examples evidencing that the proximity effect is favorable in 2D materials in a broader extent. Ferromagnetism can be induced to 2D VSe_2 at room temperature after coupling with ferromagnetic Co[239] or Fe[240] thin film, with the induced magnetic moment being about 0.3 μB and 0.16 μB per V atom at room temperature, respectively.[239,240]

Also, MoS_2, due to coupling effects with ferromagnetic $CoFe_2O_4$ thin films, generated magnetoresistance. Jie et al.

reported that this phenomenon was thickness-dependent as it enhanced dramatically in the case of a monolayer. The presence of $CoFe_2O_4$ thin film was critical for the coupling, while in the case of SiO_2/Si or MgO, the magnetoresistance effect was not observed.[241]

Interestingly, there is evidence that a type of reverse phenomenon of proximity effect can occur. It has been found that the presence of 2D materials (graphene, h-BN, and WSe_2) can affect magnetic properties and specifically increase the anisotropy field in a Co thin film. These 2D materials are able to induce antisymmetric exchange known as Dzyaloshinskii-Moriya interaction (DMI). Cobalt film in contact with the graphene is vanishing almost completely the d_z^2 contribution to the magnetic anisotropy, while the d_{xz}-d_{yz} and d_{xy}-d_x^2-$_y^2$ are not affected, leading to a selective quenching in anisotropy.[242,243]

6. 2D Materials With 4f Elements

Hitherto, elements with 3d electrons hold the lion's share of ferromagnetic materials and have monopolized the interest of the scientific community. Rare earth elements begin to gain ground, thanks to the unpaired f electrons. The 4f electrons are internal in the atomic structure of rare earth elements and engage with other electrons only with weak interactions. Despite that, f-block elements have more unpaired electrons than d-block elements, thus providing a higher magnetic moment in the compounds they are taking part. Additionally, 4f electrons are capable of stronger spin-orbit coupling to 2D materials.[244,245]

Among lanthanides, gadolinium (Gd) is one of the most prominent candidates to form 2D materials with fascinating physical properties because of the near-room temperature ferromagnetism it possesses. Similarly, lanthanides with more than half-filled f orbital (Tb, Dy, Ho, Er, Tm) but not fully filled (Yb, Lu) have a reported Curie point; hence they exhibit ferromagnetism even at an ultralow temperature (Figure 1).

In the following section, 2D materials based on gadolinium and gadolinium-doped will be analyzed, while lanthanides with a reported Curie point (Tb, Dy, Ho, Er, Tm) or contribution in a 2D magnet (Eu) will be included. For the sake of completion and comparison, non-magnetic lanthanides, which form part of 2D materials, will be briefly mentioned as well.

6.1. Gadolinium

Gadolinium stands out thanks to its near-room temperature ferromagnetic behavior. Its electron configuration [Xe $4f^7$ $5d^1$ $6s^2$] renders it the element with the higher number of unpaired electrons; thus, an extremely high magnetic moment appears, reaching even 8 μB per atom in the chemical compounds it forms. Europium has a very similar configuration to Gd, with the only difference in the absence of the d-electron, which is crucial for the properties of this element. Theoretical studies emphasize the importance of the d electron for the occurrence of hybridization, the exchange interactions, and even a high Curie point. The 4f electrons of Gd occupy spin-up orbitals, leaving spin-down orbitals empty, leading to a narrow and high-density distribution. Therefore, 4f electrons are highly localized and are not participating directly in the magnetic exchange interactions.[246,247] In that case, the 5d electron acting as a bridge facilitates the coupling of 4f localized electrons.[245]

Gadolinium tungstate,[248] besides its excellent electrical conductivity, high chemical and thermal stability and good transport properties, stands out from other rare earth metal tungstates[249,250] thanks to its low toxicity and excellent ferroelectricity.[251]

Gadolinium tungstate ($Gd_2(WO_4)_3$) nanoflakes of 2D were synthesized via a coprecipitation method and revealed promising features in the analysis and photodegradation of carbendazim (**Figure 16**). Gadolinium tungstate 2D nanoflakes can be stimulated to produce electron-hole pairs under visible light, which can lead to degrade and mineralize 98 and 74% of carbendazim, respectively. Moreover, its good electrocatalytic properties with a significant selectivity in carbendazim resulted in a LOD as low as 0.005 μM with the linear range response being from 0.02 to 40 μM. Therefore, 2D $Gd_2(WO_4)_3$ can be a favorable candidate for catalytic and sustainable environmental applications.[248]

Besides gadolinium, the whole class of lanthanides is attracting much interest in searching for new magnetic materials with low dimensionality for modern spintronic applications. Europium does not exhibit ferromagnetic order at any temperature, but its structural similarity with gadolinium can highlight the importance of the d electron (present in Gd).

Storchak group has extensively studied the potential of Eu heterostructures to form 2D magnets. By utilizing carbon and graphitic form,[253–255] silicon,[256] or germanium,[252,257,258] they highlight the importance of Eu presence and its contribution to the magnetic properties of the produced 2D heterostructures. Moreover, they provide interesting insights regarding the transition of the 3D antiferromagnetism to 2D ferromagnetism for lanthanide metalloxenes and offer a comparison between Gd and Eu coupled with Si or Ge network.[252,256] In the case of germanium, the two $LnGe_2$ (where Ln = Eu, Gd) compounds are quite similar in terms of magnetism, with Eu ions exhibiting a weak ferromagnetic coupling in their bulk form[259] that leads to a higher magnetic moment for the respective 2D $EuGe_2$; in fact, its magnetization can even reach a value which is an order of magnitude higher than that of $GdGe_2$ (Figure 16).[252] In the case of Si, the 2D $EuSi_2$ and $GdSi_2$ own a similar magnetic moment with a value slightly lower than 1 μB per formula unit at saturation. In $LnSi_2$ and $LnGe_2$, a decrease in the thickness and dimensionality leads to a transition from antiferromagnetism to ferromagnetism, with the magnetic moments favoring an in-plane orientation.[252,256]

Theoretical calculations predicted intrinsic ferromagnetism in EuBr/graphene heterojunctions with a magnetic moment as high as 7 μB per Eu atom. T_C varies between 2 and 10 K depending on the external strain. The presence of graphene contributed to the stability of the EuBr monolayer crystal, while the magnetic properties were attributed to the Eu 4f electrons.[260] Even though EuBr/graphene was not studied experimentally but only theoretically, Tan et al. claim that its synthesis could be quick and facile without demanding the use of molecular beam epitaxy that has already been used in the synthesis of some of the aforementioned materials.[253,254]

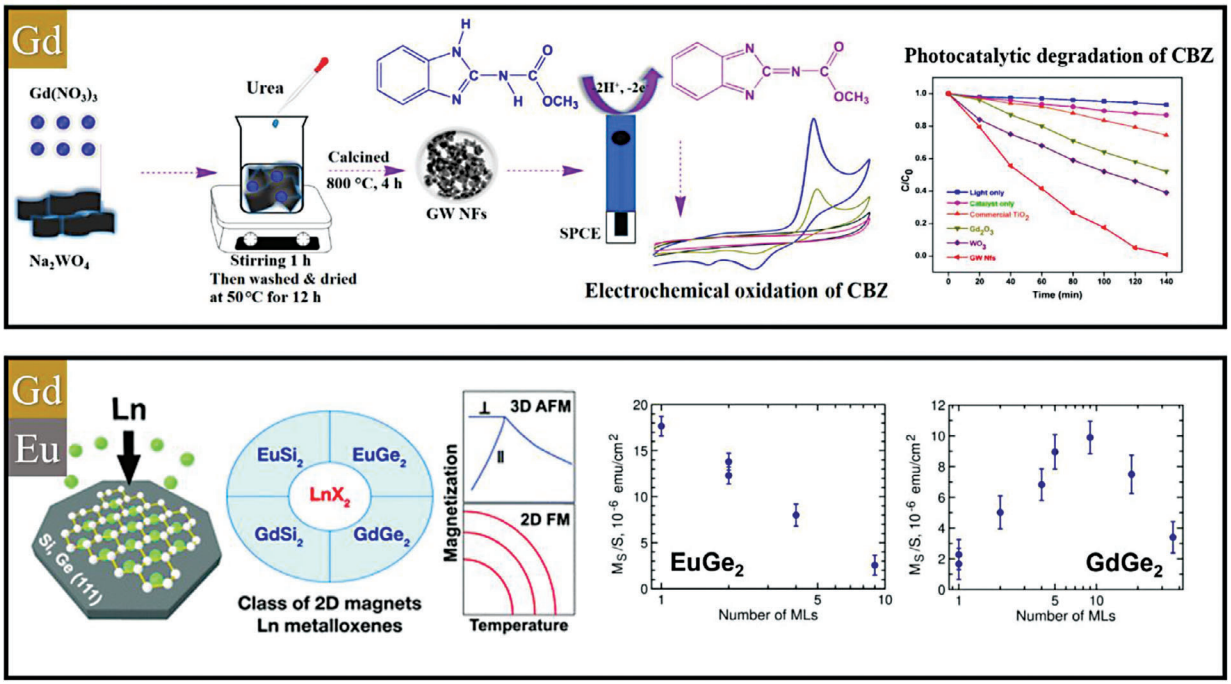

Figure 16. (Top) schematic illustration of 2D $Gd_2(WO_4)_3$ material preparation, graphs depicting electrocatalytic activity toward carbendazim (CBZ) oxidation and photocatalytic degradation of CBZ. Reproduced with permission.[248] Copyright 2019, American Chemical Society; (bottom) scheme presenting Ln metalloxenes and temperature-magnetization correlation of 3D antiferromagnetism and 2D ferromagnetism. Graphs depicting the dependence of saturation magnetization from the number of layers for $EuGe_2$ and $GdGe_2$. Reproduced with permission.[252] Copyright 2019, The Royal Society of Chemistry.

6.2. Gd-Doping

Based on the ability of Gd^{3+} ions to capture and release electrons, a Gd-doped 2D Bi_2MoO_6 nanosheet photocatalyst for nitrogen reduction with an in-built Gd^{3+} redox center was designed and prepared by Li et al. (**Figure 17**). Results showed that Gd-doping increased the number of reaction sites by enhancing the specific surface area of 2D Bi_2MoO_6 and promoted the separation and transfer of photogenerated carriers by forming in-built Gd^{3+} redox centers. The visible-light-driven nitrogen reduction performance of Gd-Bi_2MoO_6 was improved, and the average yield of NH_3 was 300.15 μmol g^{-1} h^{-1} (≈5.8 times bigger than pure Bi_2MoO_6). Theoretical calculations indicate that the Gd^{3+} redox centers can also control the formation of *NHNH to regulate the nitrogen reduction reaction, thus effectively accelerating the conversion of N_2 to NH_3 as a 2D catalyst.[261]

Marani et al. also managed to exfoliate gadolinium-doped cerium oxide utilizing a water-based synthetic route. In order to facilitate the exfoliation by minimizing the interfacial energetic cost, a water/ethanol medium was selected as a solvent. In particular, the authors applied sonication in the layered material in various ratios of water/ethanol for 8 h. The results indicated that the reaction temperature was a critical parameter for the formation of 2D layers from nanoparticles. The optimal product was obtained at 40 °C at volume ratios from 0.15 to 0.35. The small size, extended surface area, and homogenous distribution of Gd particles are favorable qualities for exploitation in various applications.[262]

Kang et al. doped MoS_2 and WSe_2 with gadolinium and other lanthanides through a novel DNA-based method by selecting and combining different types of positive ions on DNA structures. The newly proposed concept is referred to as Co-DNA, which is DNA functionalized by both divalent and trivalent Ln ions. The Co-DNA-doped TMDs were investigated as photodetector devices. Results showed that Eu^{3+} or Gd^{3+} doped MoS_2 devices showed a higher photoresponsivity than Tb^{3+} or Er^{3+} due to their broader depletion width and, subsequently, higher photocurrent. At the same time, in the case of WSe_2, an opposite trend was observed, with the Tb^{3+} and Er^{3+} doped devices exhibiting higher photoresponsivity. Then, p-doping of MoS_2 by Gd^{3+}-based Co-DNA and n-doping of WSe_2 by Tb^{3+}-based Co-DNA resulted in a better optoelectronic performance at 785 and 850 nm as compared to the control devices; a radically improved performance was observed at 655 nm in the devices doped by Tb^{3+}-based Co-DNA, but not in the case of Gd^{3+}-based Co-DNA. This was attributed to the excellent emission and absorption properties of Tb^{3+}-based Co-DNA around 655 nm through photoluminescence analysis. In contrast, Gd^{3+} ions generally show emitting and absorbing properties in the wavelength range between 250–312 nm.[263]

Zhang et al. predicted that Gd doping in monolayer MoS_2 can produce a p-type semiconductor and display ferromagnetism depending on the relative position of the gadolinium atoms. Ferromagnetism is mediated by coupling between Gd 5d and Mo 4d and intra-atomic d-f exchange interaction, emphasizing once more the importance of 5d electrons in gadolinium configuration.[264] Theoretical studies reporting ferromagnetic

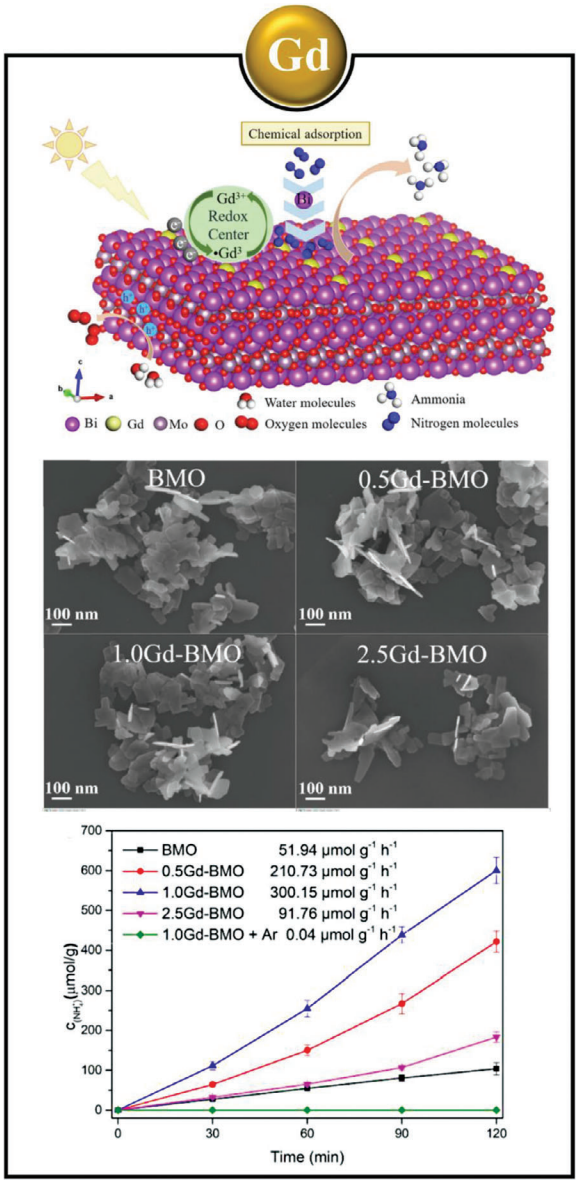

Figure 17. (Top) schematic illustration of Gd-BMO catalyst for photocatalytic nitrogen reduction under visible light irradiation; (middle) SEM images of Gd-BMO for various Gd concentrations and (bottom) performance of Gd-BMO with various Gd concentrations for photocatalytic nitrogen reduction over time. Reproduced with permission.[261] Copyright 2022, Elsevier.

behavior emerging from Gd doping highlight the importance of further investigation of 2D materials doped with gadolinium and their potential for utilization in spintronics.

In light of that, Rafiq et al. synthesized Gd^{3+}-doped MXene (Ti_3C_2) sheets through a co-precipitation method and studied their magnetic behavior. The Gd-doped MXene possessed a high magnetic moment and room temperature ferromagnetic hysteresis loop attributed to the Ti-3d electrons with measurable spin-density of states around Fermi level. Gd doping offers a large number of unpaired electrons in the MXene around Fermi level, promoting a soft ferromagnetic behavior. Additionally, Gd doping led to band gap reduction of undoped MXene from 2.06 to 1.93 eV; this characteristic can be combined with ferromagnetism, favoring the use of the resulting MXene composite in spintronic applications.[265]

6.3. Other Ferromagnetic 4f Elements

A 2D dysprosium-based MOF was synthesized through a microwave-assisted approach, exhibiting single ion magnet behavior and it is considered as the first 2D single molecular magnet.[266] Utilizing dysprosium as a dopant in a 2D structure can improve electrical conductivity and lithium diffusion. Furthermore, in combination with the defects introduced in the structure, Dy-doping can lead to a high rate capacity of lithium-ion batteries.[267]

Zirconium-based-MOF of 2D (Zr-BTB, BTB = 1,5,5-tri(4-carboxyphenyl)benzyne) was modified with terbium by a post-synthetic modification stage in which temperature was the critical parameter for terbium loading; higher temperatures found to increase terbium loading. Photoluminescence was amplified by higher Tb loading, thus higher modification temperature, which linearly decreased with increasing concentration of nitrite ions. Therefore, 2D Tb-Zr-MOF was successfully applied for the photoluminescent detection of nitrite with a LOD of 81.8 nM and good selectivity against common ionic interferents (**Figure 18**).[268] In addition, other studies reported that terbium presence in 2D structures could affect their properties or modification capabilities.[269,270]

Erbium doping in 2D WSe_2 nanosheets extended the luminescence emission of the initial material to (near-infrared) NIR II and exhibited photothermal conversion efficiency of 35.2%. The Er-doped WSe_2 was utilized for in vivo stimulation of pork and achieved a local temperature of 50 °C in 10 minutes of laser irradiation. The area under the irradiation did not reach a temperature higher than 32 °C, allowing efficient photothermal therapy targeting cancer cells over normal ones. The material is promising for diagnosis and therapeutics thanks to its properties that enable bioimaging and photothermal therapy (Figure 18).[271] Additionally, there are other examples of 2D materials with integrated erbium or erbium-doping that exhibit desirable photoresponsive properties such as fluorescence or photoluminescence.[272,273]

Holmium ions were successfully intercalated into 2D materials (montmorillonite (MMT), MXene, MoS_2, MOF, and GO) by soaking into $Ho(NO_3)_3$. In that case, the magnetic response can be tuned and boosted by controlling the soaking time, thus the holmium loading. The 2D structure of the material facilitates higher holmium loading by providing anisotropic confinement space, which 0D or 1D structures cannot. This effect could be reversible by rinsing with dilute acids or ion-chelating agents. Ho-intercalated 2D materials with reversible magnetic responses can be utilized for the development of magnetically responsive 2D actuators.[274] Theoretical calculations also suggest Ho as a promising dopant for MoS_2 to fabricate semiconductors with robust magnetism for spintronic applications. The T_C of the Ho-doped MoS_2 depends on the Ho ratio; when the ratio is higher than 6.25%, the T_C is much higher than room temperature. The respective MoS_2 doped with Er, Dy, or Cu presented considerably lower T_C.[275] Finally, it is noted that 2D thulium oxide (Tm_2O_3)

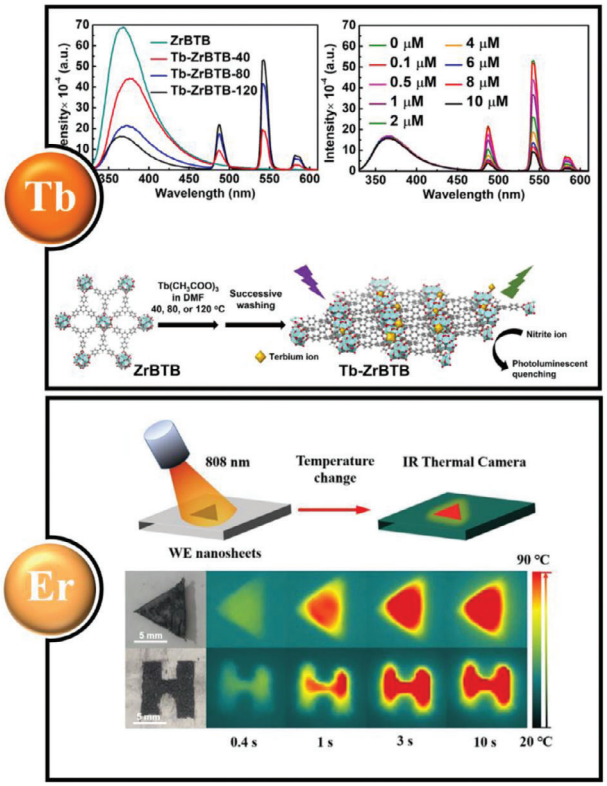

Figure 18. (Top) emission spectra of undoped and Tb-doped Zr-TBT for various activation temperatures (40, 80, 120 °C) and performance of Tb-ZrTBT120 in nitrite sensing; schematic representation of terbium introduced on a 2D ZrBTB by using post-synthetic modification for application in photoluminescence nitrite sensing. Reproduced with permission.[268] Copyright 2022, The Royal Society of Chemistry. (Bottom) Diagram of photothermal (PT) imaging process and IR images of erbium-doped WSe_2 nanosheet powders demonstrating patterned shapes of a triangle and the letter H. Reproduced with permission.[271] Copyright 2021, Elsevier.

nanosquare sheets were synthesized by a hydrothermal method, characterized structurally and spectroscopically but not tested for any applications yet.[276]

6.4. Other Non-Ferromagnetic 4f Elements

Apart from promethium (radioactive) and lutetium, which have limited contribution in the formation or doping of 2D materials, the rest lanthanides have been incorporated in 2D structures as well. Sonochemically synthesized samarium molybdate nanoplatelets were employed for electrochemical determination of insecticide oxyparathion with a limit of detection of 2 nM.[277] Moreover, samarium hydroxide attached to g-C_3N_4 nanosheets displayed good specific capacitance and was applied as an anode in an asymmetric supercapacitor device.[278]

A thin 2D Ytterbium-MOF exhibited a thickness-dependent electrochemiluminescence and was utilized for the detection of picric acid and berberine chloride form with a limit of detection reaching 81.3 nM and 36.5 nM, respectively.[279] Yb-doped perovskite nanosheets carried optimal photoluminescence quantum yields of 128% and were applied for a photodetector with dual-band detection capability.[280] A 2D Yb-TCPP MOF (where TCPP=tetra(4-carboxyphenyl) porphin) was prepared by a wet chemical method and applied in photodynamic therapy thanks to its in vitro anticancer effect.[281]

A single-atom lanthanum 2D N-doped GO showed good electrocatalytic properties toward oxygen reduction reaction and it is a bifunctional electrocatalyst. Moreover, it was utilized as a cathode in a zinc-air battery exhibiting a power density of 80.9 mW cm^{-2}.[282] Furthermore, a 2D lanthanum-cobalt hydroxide was used as an anode for supercapacitor applications, offering a high specific capacity (2162 C g^{-1}) for extended cycling tests (15 000 cycles with 96.55% capacity retention).[283]

2D CeO_2 nanoflakes synthesized by a combustion process showed good photocatalytic activity towards the degradation of the red-23 dye and electrochemical response in hydroquinone presence with a sensitivity of 2.04 μA $mμ^{-1}$ cm^{-2} and LOD of 2.9 μM.[284] Fluorine-cerium nanosheets are porous structured 2D materials with precise molecular separation ability which is useful for molecular sieving.[285]

A low symmetry structure of 2D $NdSb_2$ demonstrated an anisotropic phonon vibration and in-plane photoelectric anisotropy, and it was utilized as a broadband photodetector.[286] 2D PrOBr was predicted among many 2D rare earth materials through computational databases as a good photocatalyst and validated as such by testing toward HER and carbon dioxide reduction reaction. Indeed, ultrasonic exfoliated 2D PrOBr exhibited good photocatalytic properties outperforming common 2D photocatalysts like C_3N_4 and BiOCl.[287]

7. Summary and Outlook

In materials science, two-dimensionality is a highly desirable morphological configuration thanks to the emerging fascinating properties deriving from it. Theories supporting that ferromagnetic order could not be one of them, were disproven, and a whole new field of studies unfolded. 2D ferromagnetism paves the way for the full exploitation of 2D materials in spintronic applications by providing alternative ways to manipulate the spin effectively, with the thickness of the material playing a critical role both in ferromagnetic properties and in spin polarization.

In the quest for 2D materials with improved magnetic properties, the presence of ferromagnetic elements is of great importance. Their high magnetic moment and their abilities for spin-orbit coupling render them ideal candidates to form the next-generation 2D magnets. Nevertheless, 2D magnetism is just the fundamental characteristic among the numerous capabilities of ferromagnetic elements. The elements under discussion, either as structural constituents or as dopants, can provide several valuable properties to the 2D materials that will benefit their use in various applications in fields of catalysis, sensing, energy storage, and electromagnetic shielding, among others (**Figure 19**). For instance, ferromagnetic elements may induce a range of magnetism-related effects which can be favorable for electrochemical performance, especially when applying a suitable external magnetic field. The properties of a 2D material are largely influenced by parameters such as temperature and thermal fluctuations. Curie point determines the behavior of each material and can be adjusted by modifying i) the thickness, ii) the magnetic element composition, ii) the structural or morphological features, and iv) the preparation process of the material. Even a

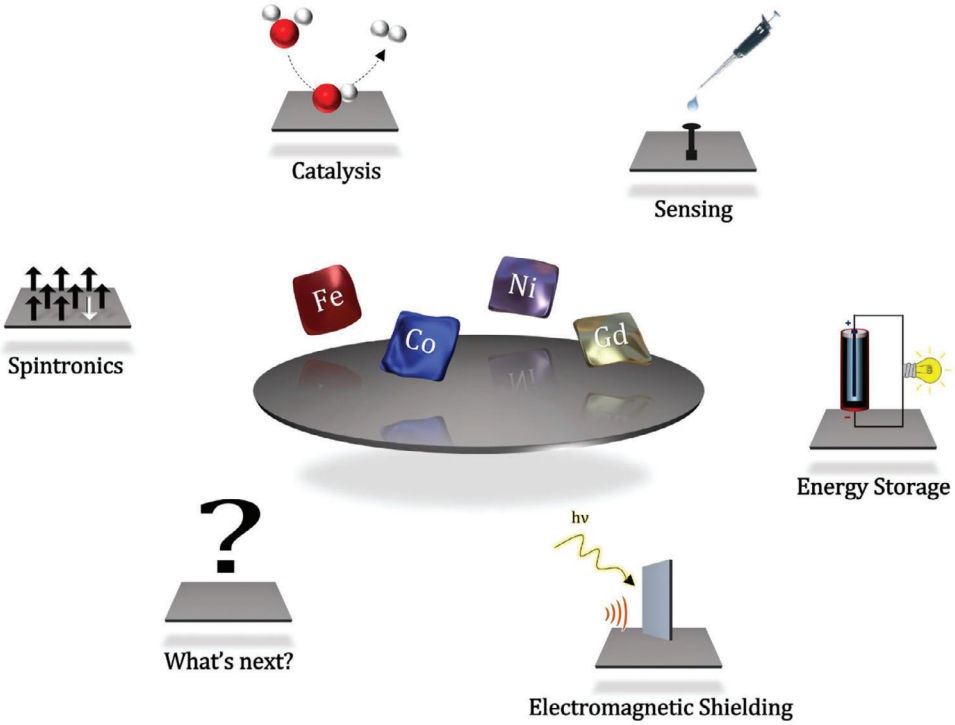

Figure 19. Applications overview of 2D materials comprising ferromagnetic elements.

seemingly subtle modification of any of these parameters might induce a considerable or even strong effect on the rest of them.

The presence of a ferromagnetic element as an adjacent atom to a 2D material can induce ferromagnetism via a phenomenon called the proximity effect. This exclusive property of ferromagnetic elements can become a promising tool to transform any "conventional" 2D material into a 2D magnet.

Besides the common ferromagnetic elements (Fe, Co, Ni), some lanthanides, with or without any reported ferromagnetic order at any temperature, can promote the appearance of high magnetic moments thanks to their f electrons and participate in the formation of 2D materials with intriguing properties. As a matter of fact, the combination of common ferromagnetic elements with lanthanides resulted in alloys (NdFeB, SmCo) with high remanence magnetism and high magnetic coercivity (i.e., high BH_{max}), making them the best permanent magnets so far. Thus, it could lead to 2D magnets with very advantageous properties.

To this end, several reported 2D materials incorporating ferromagnetic elements stand out because of their intriguing properties. Firstly, Fe_3GeTe_2 and respective materials, thanks to their metallic character, itinerant ferromagnetism and good air stability, even in monolayers, are promising candidates for spintronic devices. Additionally, Ni-BDC stands out thanks to its good electrocatalytic properties that benefit its use as a water-splitting reaction electrocatalyst, a sensing mediator, and a battery anode material. It is noted that ferromagnetic elements comprise a rather inexpensive alternative to noble metals in electrocatalysis, offering numerous metallic active sites that promote the water-splitting reaction. Studies have shown that the 2D form of these materials is more effective in electrocatalysis thanks to its larger surface area compared to its bulk form. Cobalt and iron seem to have a positive effect on MoS_2 either as an adjacent atom or as a dopant, providing MoS_2 coveted magnetic and electronic properties that will facilitate its use in spintronics.

In conclusion, ferromagnetic elements, by forming and doping 2D materials, are able to improve the already existing properties and endow new ones. At the same time, in proximity to such 2D materials, ferromagnetic elements can induce the appearance of ferromagnetic behavior and grant long-lasting magnetic properties. The materials under discussion have remarkable properties which render them suitable for a range of applications, such as electrocatalysis, energy storage, sensing and spintronics, among others. In certain cases their performance matches or is superior than that of benchmark materials, whereas in other cases it may be a bit lesser but it is still competitive, taking into account also criteria such as the cost-efficiency.

The current challenges in the field of 2D ferromagnetism have to do with the discovery of monolayered materials with i) room temperature ferromagnetic order, ii) high conductivity, and iii) good air stability that can be produced in a large scale and be implemented in practical applications. Ferromagnetic elements are anticipated to unlock these challenges and give rise to novel materials with superb properties. In this context, it would be helpful to manage the further development of more modern characterization techniques for the materials under discussion. Even minor modifications in the surface characteristics of 2D materials (e.g., population of defects) may have a considerable effect on their apparent properties and on the resulting performance in applications. In this frame, ultra-high resolution electron microscopy techniques may help to shed more light on the peculiar structural features of 2D materials, even at the atomic scale.

In this way, a better feedback can be provided to the synthetic community, which will aim to elaborate more tailored synthetic approaches, aiming to achieve the acquisition of specific morphological, structural and compositional features in order to produce 2D materials 'by design'. In situ monitoring characterization techniques can be utilized more frequently since they help to better study the growth evolution of 2D materials in real-time, thus gaining important insights on their growth mechanisms. Finally, artificial intelligence and machine learning can help to predict the best-performing 2D materials of the future, by analyzing thoroughly the existing data from the literature. As a result, valuable labor time will be saved, by directing the research endeavors of experimental scientists in well-planned avenues. The risk of a failed experiment may never disappear, but it can be at least minimized, with the help of well-focused analyses of data, simulations and computations.

Acknowledgements

A.P. was supported by the Onassis foundation – Scholarship ID: F ZS 045-1/2022-2023 and Bodossaki foundation Scholarship. L.P. acknowledges the support from the Spanish Ministerio de Ciencia e Innovación through the Ramón y Cajal grant (RYC2018-026103-I) and the Spanish State Research Agency (Grant Numbers. PID2020-117371RA-I00; TED2021-131628A-I00), as well as the grant from the Xunta de Galicia (ED431F2021/05). The authors acknowledge the Universidade de Vigo/CISUG for open access funding. Z.S. was supported by ERC-CZ program (project LL2101) from Ministry of Education Youth and Sports (MEYS) and by project reg. No. CZ.02.1.01/0.0/0.0/15_003/0000444 financed by EFRR.

Conflict of Interest

The authors declare no conflict of interest.

Keywords

2D ferromagnets, applications, doping, lanthanides, proximity effect

Received: August 29, 2023
Revised: October 31, 2023
Published online:

[1] A. S. Sarkar, E. Stratakis, *Adv. Sci.* **2020**, *7*, 2001655.
[2] V. Shanmugam, R. A. Mensah, K. Babu, S. Gawusu, A. Chanda, Y. Tu, R. E. Neisiany, M. Försth, G. Sas, O. Das, *Part. Part. Syst. Charact.* **2022**, *39*, 2200031.
[3] P. Ares, K. S. Novoselov, *Nano Mater. Sci.* **2022**, *4*, 3.
[4] A. K. Geim, K. S. Novoselov, *Nat. Mater.* **2007**, *6*, 183.
[5] R. Mas-Ballesté, C. Gómez-Navarro, J. Gómez-Herrero, F. Zamora, *Nanoscale* **2011**, *3*, 20.
[6] H. Tao, Q. Fan, T. Ma, S. Liu, H. Gysling, J. Texter, F. Guo, Z. Sun, *Prog. Mater. Sci.* **2020**, *111*, 100637.
[7] A. Khan, J. Azadmanjiri, B. Wu, L. Liping, Z. Sofer, J. Min, *Adv. Energy Mater.* **2021**, *11*, 2100451.
[8] D. Deng, K. S. Novoselov, Q. Fu, N. Zheng, Z. Tian, X. Bao, *Nat. Nanotechnol.* **2016**, *11*, 218.
[9] L. Tian, Z. Li, M. Song, J. Li, *Nanoscale* **2021**, *13*, 12088.
[10] M. P. Browne, Z. Sofer, M. Pumera, *Energy Environ. Sci.* **2019**, *12*, 41.
[11] G. S. Shanker, A. Biswas, S. Ogale, *J. Phys. Energy* **2021**, *3*, 022003.
[12] H. Zhang, T. Fan, W. Chen, Y. Li, B. Wang, *Bioact. Mater.* **2020**, *5*, 1071.
[13] M. J. Molaei, *J. Drug Deliv. Sci. Technol.* **2021**, *61*, 101830.
[14] J. Ouyang, S. Rao, R. Liu, L. Wang, W. Chen, W. Tao, N. Kong, *Adv. Drug Delivery Rev.* **2022**, *185*, 114268.
[15] G. Alarcon-Angeles, M. Palomar-Pardavé, A. Merkoçi, *Electroanalysis* **2018**, *30*, 1271.
[16] A. Ch. Lazanas, M. I. Prodromidis, *Microchim. Acta* **2021**, *188*, 6.
[17] B. Huang, G. Clark, E. Navarro-Moratalla, D. R. Klein, R. Cheng, K. L. Seyler, D. Zhong, E. Schmidgall, M. A. Mcguire, D. H. Cobden, W. Yao, D. Xiao, P. Jarillo-Herrero, X. Xu, *Nature* **2017**, *546*, 270.
[18] C. Gong, L. Li, Z. Li, H. Ji, A. Stern, Y. Xia, T. Cao, W. Bao, C. Wang, Y. Wang, Z. Q. Qiu, R. J. Cava, S. G. Louie, J. Xia, X. Zhang, *Nature* **2017**, *546*, 265.
[19] E. Elahi, G. Dastgeer, G. Nazir, S. Nisar, M. Bashir, H. Akhter Qureshi, D.-K. Kim, J. Aziz, M. Aslam, K. Hussain, M. A. Assiri, M. Imran, *Comput. Mater. Sci.* **2022**, *213*, 111670.
[20] A. Hirohata, K. Yamada, Y. Nakatani, I.-L. Prejbeanu, B. Diény, P. Pirro, B. Hillebrands, *J. Magn. Magn. Mater.* **2020**, *509*, 166711.
[21] G. Hu, B. Xiang, *Nanoscale Res. Lett.* **2020**, *15*, 226.
[22] E. C. Ahn, *npj 2D Mater. Appl.* **2020**, *4*, 17.
[23] X. Li, B. Dong, X. Sun, H. Wang, T. Yang, G. Yu, Z. Vitto Han, *J. Semicond.* **2019**, *40*, 081508.
[24] H. Li, S. Ruan, Y.-J. Zeng, *Adv. Mater.* **2019**, *31*, 1900065.
[25] Y. Deng, Y. Yu, Y. Song, J. Zhang, N. Z. Wang, Z. Sun, Y. Yi, Y. Z Wu, S. Wu, J. Zhu, J. Wang, X. H. Chen, Y. Zhang, *Nature* **2018**, *563*, 94.
[26] R. Zhang, R. F. Willis, *Phys. Rev. Lett.* **2001**, *86*, 2665.
[27] M. Bonilla, S. Kolekar, Y. Ma, H. C. Diaz, V. Kalappattil, R. Das, T. Eggers, H. R. Gutierrez, M.-H. Phan, M. Batzill, *Nat. Nanotechnol.* **2018**, *13*, 289.
[28] Q. Liang, Q. Zhang, X. Zhao, M. Liu, A. T. S. Wee, *ACS Nano* **2021**, *15*, 2165.
[29] S. N. Reed-Lingenfelter, M. Wang, N. L. Williams, J. Cha, *Adv. Mater. Interfaces* **2022**, *9*, 2100463.
[30] S. Yu, J. Tang, Y. Wang, F. Xu, X. Li, X. Wang, *Sci. Technol. Adv. Mater.* **2022**, *23*, 140.
[31] C. Huang, J. Feng, F. Wu, D. Ahmed, B. Huang, H. Xiang, K. Deng, E. Kan, *J. Am. Chem. Soc.* **2018**, *140*, 11519.
[32] M. Batzill, *Surf. Sci. Rep.* **2012**, *67*, 83.
[33] O. Cretu, A. R. Botello-Mendez, I. Janowska, C. Pham-Huu, J.-C. Charlier, F. Banhart, *Nano Lett.* **2013**, *13*, 3487.
[34] M. Gibertini, M. Koperski, A. F. Morpurgo, K. S. Novoselov, *Nat. Nanotechnol.* **2019**, *14*, 408.
[35] S. Kumari, D. K. Pradhan, N. R. Pradhan, P. D. Rack, *Emergent Mater.* **2021**, *4*, 827.
[36] D. J. O'hara, T. Zhu, A. H. Trout, A. S. Ahmed, Y. K. Luo, C. H. Lee, M. R. Brenner, S. Rajan, J. A. Gupta, D. W. Mccomb, R. K. Kawakami, *Nano Lett.* **2018**, *18*, 3125.
[37] H. Wu, W. Zhang, L. Yang, J. Wang, J. Li, L. Li, Y. Gao, L. Zhang, J. Du, H. Shu, H. Chang, *Nat. Commun.* **2021**, *12*, 5688.
[38] S. Liu, X. Yuan, Y. Zou, Y. Sheng, C. Huang, E. Zhang, J. Ling, Y. Liu, W. Wang, C. Zhang, J. Zou, K. Wang, F. Xiu, *npj 2D Mater. Appl.* **2017**, *1*, 30.
[39] R. Skomski, in *Novel Functional Magnetic Materials* (Ed: A. Zhukov), Springer, Cham **2016**, 359.
[40] M. Shimizu, *Phys. B+C* **1977**, *91*, 14.
[41] W. C. Thoburn, S. Legvold, F. H. Spedding, *Phys. Rev.* **1958**, *112*, 56.
[42] B. L. Rhodes, S. Legvold, F. H. Spedding, *Phys. Rev.* **1958**, *109*, 1547.
[43] J. F. Elliott, S. Legvold, F. H. Spedding, in *The ferromagnetic properties of the rare earth metals*, Ames Laboratory ISC Technical Reports, Iowa, USA, **1953**.

[44] A. Fujimori, A. E. Bocquet, T. Saitoh, T. Mizokawa, *J. Electron Spectros. Relat. Phenomena* **1993**, *62*, 141.
[45] K. O. Kvashnina, S. M. Butorin, P. Glatzel, *J. Anal. At. Spectrom.* **2011**, *26*, 1265.
[46] B. T. Kilbourn, *Concise Encyclopedia of Advanced Ceramic Materials*,Elsevier, Pergamon **1991**, https://doi.org/10.1016/C2009-1-28294-3.
[47] J. M. D. Coey, M. Venkatesan, H. Xu, in *Functional Metal Oxides*, Wiley-VCH Verlag GmbH & Co. KGaA, Weinheim, Germany, **2013**, p. 3.
[48] N. D. Mermin, H. Wagner, *Phys. Rev. Lett.* **1966**, *17*, 1133.
[49] S. Jenkins, L. Rózsa, U. Atxitia, R. F. L. Evans, K. S. Novoselov, E. J. G. Santos, *Nat. Commun.* **2022**, *13*, 6917.
[50] D. L. Cortie, G. L. Causer, K. C. Rule, H. Fritzsche, W. Kreuzpaintner, F. Klose, *Adv. Funct. Mater.* **2020**, *30*, 1901414.
[51] H.-J. Elmers, *Int. J. Mod. Phys. B* **1995**, *9*, 3115.
[52] X. Jiang, Q. Liu, J. Xing, N. Liu, Y. Guo, Z. Liu, J. Zhao, *Appl. Phys. Rev.* **2021**, *8*, 031305.
[53] Z. Fei, B. Huang, P. Malinowski, W. Wang, T. Song, J. Sanchez, W. Yao, D. Xiao, X. Zhu, A. F. May, W. Wu, D. H. Cobden, J.-H. Chu, X. Xu, *Nat. Mater.* **2018**, *17*, 778.
[54] X. Wang, D. Li, Z. Li, C. Wu, C.-M. Che, G. Chen, X. Cui, *ACS Nano* **2021**, *15*, 16236.
[55] H. H. Kim, B. Yang, S. Li, S. Jiang, C. Jin, Z. Tao, G. Nichols, F. Sfigakis, S. Zhong, C. Li, S. Tian, D. G. Cory, G.-X. Miao, J. Shan, K. F. Mak, H. Lei, K. Sun, L. Zhao, A. W. Tsen, *Proc. Natl. Acad. Sci. USA* **2019**, *166*, 11131.
[56] G. Zhang, F. Guo, H. Wu, X. Wen, L. Yang, W. Jin, W. Zhang, H. Chang, *Nat. Commun.* **2022**, *13*, 5067.
[57] X. Sun, W. Li, X. Wang, Q. Sui, T. Zhang, Z. Wang, L. Liu, D. Li, S. Feng, S. Zhong, H. Wang, V. Bouchiat, M. Nunez Regueiro, N. Rougemaille, J. Coraux, A. Purbawati, A. Hadj-Azzem, Z. Wang, B. Dong, X. Wu, T. Yang, G. Yu, B. Wang, Z. Han, X. Han, Z. Zhang, *Nano Res.* **2020**, *13*, 3358.
[58] J.-U. Lee, S. Lee, J. H Ryoo, S. Kang, T. Y. Kim, P. Kim, C.-H. Park, J.-G. Park, H. Cheong, *Nano Lett.* **2016**, *16*, 7433.
[59] H. L. Zhuang, P. R. C. Kent, R. G. Hennig, *Phys. Rev. B* **2016**, *93*, 134407.
[60] S. Mondal, N. Khan, S. M. Mishra, B. Satpati, P. Mandal, *Phys. Rev. B* **2021**, *104*, 094405.
[61] Z. Li, W. Xia, H. Su, Z. Yu, Y. Fu, L. Chen, X. Wang, N. Yu, Z. Zou, Y. Guo, *Sci. Rep.* **2020**, *10*, 15345.
[62] I. Zutic, J. Fabian, S. Das Sarma, *Rev. Mod. Phys.* **2004**, *76*, 323.
[63] D. D. Awschalom, M. E. Flatté, *Nat. Phys.* **2007**, *3*, 153.
[64] M. Alghamdi, M. Lohmann, J. Li, P. R. Jothi, Q. Shao, M. Aldosary, T. Su, B. P. T. Fokwa, J. Shi, *Nano Lett.* **2019**, *19*, 4400.
[65] Y.-T. Liu, T.-Y. Chen, T.-H. Lo, T. Y. Tsai, S. Y. Yang, Y.-J. Chang, J.-H. Wei, C.-F. Pai, *Phys. Rev. Appl.* **2020**, *13*, 044032.
[66] X. Wang, J. Tang, X. Xia, C. He, J. Zhang, Y. Liu, C. Wan, C. Fang, C. Guo, W. Yang, Y. Guang, X. Zhang, H. Xu, J. Wei, M. Liao, X. Lu, J. Feng, X. Li, Y. Peng, H. Wei, R. Yang, D. Shi, X. Zhang, Z. Han, Z. Zhang, G. Zhang, G. Yu, X. Han, *Sci. Adv.* **2019**, *5*, eaaw8904.
[67] Y. Zhang, H. Xu, C. Yi, X. Wang, Y. Huang, J. Tang, J. Jiang, C. He, M. Zhao, T. Ma, J. Dong, C. Guo, J. Feng, C. Wan, H. Wei, H. Du, Y. Shi, G. Yu, G. Zhang, X. Han, *Appl. Phys. Lett.* **2021**, *118*, 262406.
[68] I.-H. Kao, R. Muzzio, H. Zhang, M. Zhu, J. Gobbo, S. Yuan, D. Weber, R. Rao, J. Li, J. H. Edgar, J. E. Goldberger, J. Yan, D. G. Mandrus, J. Hwang, R. Cheng, J. Katoch, S. Singh, *Nat. Mater.* **2022**, *21*, 1029.
[69] I. Shin, W. J. Cho, E. S. An, S. Park, H.-W. Jeong, S. Jang, W. J. Baek, S. Y. Park, D.-H. Yang, J. H. Seo, G.-Y. Kim, M. N. Ali, S.-Y. Choi, H.-W. Lee, J. S. Kim, S. D. Kim, G. H. Lee, *Adv. Mater.* **2022**, *34*, 2101730.
[70] W. Zhu, H. Lin, F. Yan, C. Hu, Z. Wang, L. Zhao, Y. Deng, Z. R. Kudrynskyi, T. Zhou, Z. D. Kovalyuk, Y. Zheng, A. Patanè, I. Zutic, S. Li, H. Zheng, K. Wang, *Adv. Mater.* **2021**, *33*, 2104658.
[71] K.-H. Min, D. H. Lee, S.-J. Choi, I.-H. Lee, J. Seo, D. W. Kim, K.-T. Ko, K. Watanabe, T. Taniguchi, D. H. Ha, C. Kim, J. H Shim, J. Eom, J. S. Kim, S. Jung, *Nat. Mater.* **2022**, *21*, 1144.
[72] Y. Zheng, X. Ma, F. Yan, H. Lin, W. Zhu, Y. Ji, R. Wang, K. Wang, *npj 2D Mater. Appl.* **2022**, *6*, 62.
[73] S. Ikeda, K. Miura, H. Yamamoto, K. Mizunuma, H. D. Gan, M. Endo, S. Kanai, J. Hayakawa, F. Matsukura, H. Ohno, *Nat. Mater.* **2010**, *9*, 721.
[74] X. Li, S. Yin, Y. Liu, D. Zhang, X. Xu, J. Miao, Y. Jiang, *Appl. Phys. Express* **2011**, *4*, 043006.
[75] W. Jin, G. Zhang, H. Wu, L. Yang, W. Zhang, H. Chang, *ACS Appl. Mater. Interfaces* **2023**, *15*, 36519.
[76] J. Meng, J.-J. Chen, Y. Yan, D.-P. Yu, Z.-M. Liao, *Nanoscale* **2013**, *5*, 8894.
[77] W. Wang, A. Narayan, L. Tang, K. Dolui, Y. Liu, X. Yuan, Y. Jin, Y. Wu, I. Rungger, S. Sanvito, F. Xiu, *Nano Lett.* **2015**, *15*, 5261.
[78] W. Zhu, S. Xie, H. Lin, G. Zhang, H. Wu, T. Hu, Z. Wang, X. Zhang, J. Xu, Y. Wang, Y. Zheng, F. Yan, J. Zhang, L. Zhao, A. Patané, J. Zhang, H. Chang, K. Wang, *Chin. Phys. Lett.* **2022**, *39*, 128501.
[79] H. Lin, X. Luo, L. Liu, D. Wang, X. Zhao, Z. Wang, X. Xue, F. Zhang, G. Xing, *Micromachines* **2022**, *13*, 319.
[80] H. Lin, F. Yan, C. Hu, Q. Lv, W. Zhu, Z. Wang, Z. Wei, K. Chang, K. Wang, *ACS Appl. Mater. Interfaces* **2020**, *12*, 43921.
[81] W. Jin, G. Zhang, H. Wu, L. Yang, W. Zhang, H. Chang, *Nanoscale* **2023**, *15*, 5371.
[82] B. Zhao, R. Ngaloy, S. Ghosh, S. Ershadrad, R. Gupta, K. Ali, A. M.. Hoque, B. Karpiak, D. Khokhriakov, C. Polley, B. Thiagarajan, A. Kalaboukhov, P. Svedlindh, B. Sanyal, S. P. Dash, *Adv. Mater.* **2023**, *35*, 2209113.
[83] L. Zhang, X. Huang, H. Dai, M. Wang, H. Cheng, L. Tong, Z. Li, X. Han, X. Wang, L. Ye, J. Han, *Adv. Mater.* **2020**, *32*, 2002032.
[84] C. Gong, P. Zhang, T. Norden, Q. Li, Z. Guo, A. Chaturvedi, A. Najafi, S. Lan, X. Liu, Y. Wang, S.-J. Gong, H. Zeng, H. Zhang, A. Petrou, X. Zhang, *Nat. Commun.* **2023**, *14*, 3839.
[85] X. Wang, J. Cao, Z. Lu, A. Cohen, H. Kitadai, T. Li, Q. Tan, M. Wilson, C. H. Lui, D. Smirnov, S. Sharifzadeh, X. Ling, *Nat. Mater.* **2021**, *20*, 964.
[86] C. F. Schippers, H. J. M. Swagten, M. H. D. Guimarães, *Phys. Rev. Mater.* **2020**, *4*, 084007.
[87] Q. Liu, L. Wang, Y. Fu, X. Zhang, L. Huang, H. Su, J. Lin, X. Chen, D. Yu, X. Cui, J.-W. Mei, J.-F. Dai, *Phys. Rev. B* **2021**, *103*, 235411.
[88] Q. Wang, Y. Zeng, K. Yuan, Q. Zeng, P. Gu, X. Xu, H. Wang, Z. Han, K. Nomura, W. Wang, E. Liu, Y. Hou, Y. Ye, *Nat. Electron.* **2023**, *6*, 119.
[89] M. Yue, H. Lambert, E. Pahon, R. Roche, S. Jemei, D. Hissel, *Renew. Sustain. Energy Rev.* **2021**, *146*, 111180.
[90] E. S. Hanley, J. Deane, B. Gallachóir, *Renew. Sustain. Energy Rev.* **2018**, *82*, 3027.
[91] Q. Shi, C. Zhu, D. Du, Y. Lin, *Chem. Soc. Rev.* **2019**, *48*, 3181.
[92] C. Li, J.-B. Baek, *ACS Omega* **2020**, *5*, 31.
[93] F. Lyu, Q. Wang, S. M. Choi, Y. Yin, *Small* **2019**, *15*, 1804201.
[94] X. Zhang, J. Hu, X. Cheng, K. A. Nartey, L. Zhang, *Electrochim. Acta* **2021**, *367*, 137536.
[95] W. Yaseen, N. Ullah, M. Xie, B. A. Yusuf, Y. Xu, C. Tong, J. Xie, *Surf. Interfaces* **2021**, *26*, 101361.
[96] X. Cao, T. Wang, L. Jiao, *Adv. Fiber Mater.* **2021**, *3*, 210.
[97] S. Bhattacharjee, S.-C. Lee, *J. Phys. Chem. C* **2018**, *122*, 894.
[98] Y. Zhang, C. Liang, J. Wu, H. Liu, B. Zhang, Z. Jiang, S. Li, P. Xu, *ACS Appl. Energy Mater.* **2020**, *3*, 10303.
[99] P. Dunne, J. M. D. Coey, *J. Phys. Chem. C* **2019**, *123*, 24181.
[100] X. Li, Z. Cheng, *Chem. Catal.* **2022**, *2*, 2140.
[101] M. F. Kaya, N. Demir, M. S. Albawabiji, M. Tas, *Int. J. Hydrog. Energy* **2017**, *42*, 17583.

[102] L. M. A. Monzon, K. Rode, M. Venkatesan, J. M. D. Coey, *Chem. Mater.* **2012**, *24*, 3878.
[103] W. Zhou, M. Chen, M. Guo, A. Hong, T. Yu, X. Luo, C. Yuan, W. Lei, S. Wang, *Nano Lett.* **2020**, *20*, 2923.
[104] T. Li, T. Jing, D. Rao, S. Mourdikoudis, Y. Zuo, M. Wang, *Inorg. Chem. Front.* **2022**, *9*, 6008.
[105] S. Anantharaj, S. R. Ede, K. Sakthikumar, K. Karthick, S. Mishra, S. Kundu, *ACS Catal.* **2016**, *6*, 8069.
[106] Q. Ma, C. Hu, K. Liu, S. F. Hung, D. Ou, H. M. Chen, G. Fu, N. Zheng, *Nano Energy* **2017**, *41*, 148.
[107] Y. Ping, R. J. Nielsen, W. A. Goddard, *J. Am. Chem. Soc.* **2017**, *139*, 149.
[108] Y. Zhao, J. Gu, Z. Chen, *Adv. Funct. Mater.* **2019**, *29*, 1904782.
[109] K. L. Ao, Y. Shao, I. N. Chan, X. Shi, Y. Kawazoe, M. Yang, K. W. Ng, H. Pan, *Int. J. Hydrogen Energy* **2020**, *45*, 16201.
[110] F. M. Oliveira, N. Antonatos, V. Mazánek, D. Sedmidubský, Z. Sofer, R. Gusmão, *FlatChem* **2022**, *32*, 100334.
[111] W. Huang, C. Peng, J. Tang, F. Diao, M. Nulati Yesibolati, H. Sun, C. Engelbrekt, J. Zhang, X. Xiao, K. S. Mølhave, *J. Energy Chem.* **2021**, *65*, 78.
[112] D. Zhu, J. Liu, L. Wang, Y. Du, Y. Zheng, K. Davey, S.-Z. Qiao, *Nanoscale* **2019**, *11*, 3599.
[113] X. Zhang, R. Lin, X. Meng, W. Li, F. Chen, J. Hou, *Inorg. Chem.* **2021**, *60*, 9987.
[114] E. Sadeghi, N. S. Peighambardoust, S. Chamani, U. Aydemir, *ACS Mater. Au* **2023**, *3*, 143.
[115] Q. Li, Y. Zhou, C. Chen, Q. Liu, J. Huo, H. Yi, *J. Electroanal. Chem.* **2021**, *895*, 115514.
[116] Y. Jeung, H. Roh, K. Yong, *Appl. Surf. Sci.* **2022**, *576*, 151720.
[117] N. Yao, T. Tan, F. Yang, G. Cheng, W. Luo, *Mater. Chem. Front.* **2018**, *2*, 1732.
[118] N. Joshi, G. Pransu, C. A. Conte-Junior, *Crit. Rev. Food Sci. Nutr.* **2022**, *46*, 17967.
[119] D. Chauhan, M. Ashfaq, N. Talreja, R. V. Managalraja, *J. Biomed. Res. Environ. Sci.* **2021**, *2*, 977.
[120] A. V. Papavasileiou, I. Panagiotopoulos, M. I. Prodromidis, *Electrochim. Acta* **2020**, *360*, 136981.
[121] G. Yang, F. Zhao, B. Zeng, *Electrochim. Acta* **2014**, *135*, 154.
[122] S. Luo, K. Elouarzaki, Z. J. Xu, *Angew. Chem., Int. Ed.* **2022**, *61*, e202203564.
[123] S. Tong, Z. Li, B. Qiu, Y. Zhao, Z. Zhang, *Sens. Actuators, B* **2018**, *258*, 789.
[124] Y. Zhu, X. Ma, X. Lv, L. Zhang, C. Li, N. Shi, J. Wang, *Microchim. Acta* **2022**, *189*, 345.
[125] P. Balasubramanian, S.-B. He, H.-H. Deng, H.-P. Peng, W. Chen, *Sens. Actuators, B* **2020**, *320*, 128374.
[126] Y. Shu, B. Li, J. Chen, Q. Xu, H. Pang, X. Hu, *ACS Appl. Mater. Interfaces* **2018**, *10*, 2360.
[127] R. Sukanya, R. Karthik, S. Mohandoss, M. Hasan, J.-J. Shim, Y. R. Lee, *J. Clean. Prod.* **2023**, *389*, 136059.
[128] L. Wang, Y. Zhao, Y. Tian, *J. Nanopart. Res.* **2015**, *17*, 393.
[129] S. E. A. Elashery, N. F. Attia, H. Oh, *Anal. Chim. Acta* **2022**, *1197*, 339518.
[130] S. Jin, G. Yang, H. Song, H. Cui, C. Wang, *ACS Appl. Mater. Interfaces* **2015**, *7*, 24932.
[131] Q. Liang, Y. Zheng, C. Du, Y. Luo, J. Zhang, B. Li, Y. Zong, Q. Yan, *Small Methods* **2017**, *1*, 1700304.
[132] W. Ma, L. Wang, Y. Li, M. Shi, H. Cui, *Adv. Powder Technol.* **2018**, *29*, 631.
[133] Y. Jiao, J. Pei, C. Yan, D. Chen, Y. Hu, G. Chen, *J. Mater. Chem. A* **2016**, *4*, 13344.
[134] Y. Li, Y.-L. Li, B. Sa, R. Ahuja, *Catal. Sci. Technol.* **2017**, *7*, 545.
[135] Y. Zhao, S. Zhang, R. Shi, G. I. N. Waterhouse, J. Tang, T. Zhang, *Mater. Today* **2020**, *34*, 78.
[136] J. Fu, J. Yu, C. Jiang, B. Cheng, *Adv. Energy Mater.* **2018**, *8*, 1701503.
[137] X. Han, T. Si, Q. Liu, F. Zhu, R. Li, X. Chen, J. Liu, H. Sun, J. Zhao, H. Ling, Q. Zhang, H. Wang, *Chem. Eng. J.* **2021**, *426*, 130824.
[138] A. Corma, H. Garcia, *J. Catal.* **2013**, *308*, 168.
[139] B. Han, X. Ou, Z. Deng, Y. Song, C. Tian, H. Deng, Y.-J. Xu, Z. Lin, *Angew. Chem., Int. Ed.* **2018**, *57*, 16811.
[140] H. Chang, Y. Zhou, S. Zhang, X. Zheng, Q. Xu, *Adv. Mater. Interfaces* **2021**, *8*, 2100205.
[141] C. Wang, X.-M. Liu, M. Zhang, Y. Geng, L. Zhao, Y.-G. Li, Z.-M. Su, *ACS Sustain. Chem. Eng.* **2019**, *7*, 14102.
[142] J. Shen, M. J. Kolb, A. J. Göttle, M. T. M. Koper, *J. Phys. Chem. C* **2016**, *120*, 15714.
[143] X. Chen, M. Cong, M. Tang, J. Liu, S. Chen, Y. Gao, *Inorg. Chem. Front.* **2022**, *9*, 4369.
[144] G. Wang, Z. Gao, G. Wan, S. Lin, P. Yang, Y. Qin, *Nano Res.* **2014**, *7*, 704.
[145] L. Sha, P. Gao, T. Wu, Y. Chen, *ACS Appl. Mater. Interfaces* **2017**, *9*, 40412.
[146] Z. Zhu, X. Sun, G. Li, H. Xue, H. Guo, X. Fan, X. Pan, J. He, *J. Magn. Magn. Mater.* **2015**, *377*, 95.
[147] V. Sunny, D. S. Kumar, P. Mohanan, M. R. Anantharaman, *Mater. Lett.* **2010**, *64*, 1130.
[148] J. Fang, W. Zha, M. Kang, S. Lu, L. Cui, S. Li, *J. Mater. Sci.* **2013**, *48*, 8060.
[149] N. Wu, H. Lv, J. Liu, Y. Liu, S. Wang, W. Liu, *Phys. Chem. Chem. Phys.* **2016**, *18*, 31542.
[150] J. Xu, N. Lu, M. Yuan, G. Sun, *Nano Res.* **2023**, *16*, 5676.
[151] X. Liang, C. Wang, M. Yu, Z. Yao, Y. Zhang, *J. Alloys Compd.* **2022**, *910*, 164844.
[152] D. Tahir, H. Heryanto, S. Ilyas, A. N. Fahri, R. Rahmat, M. H. Rahmi, Y. Taryana, S. G. Sukaryo, *J. Alloys Compd.* **2021**, *864*, 158780.
[153] D. Wanasinghe, F. Aslani, *Compos. Part B Eng.* **2019**, *176*, 107207.
[154] M. Liu, L. Wu, B. Fan, G. Tong, D. Chen, W. Wu, *Appl. Surf. Sci.* **2022**, *571*, 151273.
[155] J. Ge, Y. Cui, Y. Cai, J. Qian, L. Liu, F. Meng, F. Wang, *Compos. Part B Eng.* **2021**, *224*, 109172.
[156] F. Ma, Y. Qin, Y. Z. Li, *Appl. Phys. Lett.* **2010**, *96*, 202507.
[157] B. Zhao, X. Zhang, J. Deng, Z. Bai, L. Liang, Y. Li, R. Zhang, *Phys. Chem. Chem. Phys.* **2018**, *20*, 28623.
[158] C. Mu, X. Du, A. Nie, B. Wang, F. Wen, J. Xiang, K. Zhai, Z. Liu, *Appl. Phys. Lett.* **2019**, *115*, 043103.
[159] L.-S. Fu, J.-T. Jiang, C.-Y. Xu, L. Zhen, *CrystEngComm* **2012**, *14*, 6827.
[160] Y. Ji, Y. Chang, C. Mu, B. Wang, F. Wen, J. Xiang, K. Zhai, T. Xue, Z. Liu, *J. Mater. Sci.* **2021**, *56*, 16524.
[161] P. Zhao, M. Jian, Q. Zhang, R. Xu, R. Liu, X. Zhang, H. Liu, *J. Mater. Chem. A* **2019**, *7*, 16598.
[162] J. Ren, Z. Zhu, Y. Qiu, F. Yu, J. Ma, J. Zhao, *J. Hazard. Mater.* **2021**, *408*, 124846.
[163] A. Shahzad, K. Rasool, W. Miran, M. Nawaz, J. Jang, K. A. Mahmoud, D. S. Lee, *J. Hazard. Mater.* **2018**, *344*, 811.
[164] L. Wang, C. Shi, L. Wang, L. Pan, X. Zhang, J.-J. Zou, *Nanoscale* **2020**, *12*, 4790.
[165] J. T. Kim, C. W. Lee, H. J. Jung, H. J. Choi, A. Salman, S. Padmajan Sasikala, S. O. Kim, *ACS Nano* **2022**, *16*, 17687.
[166] D. Manos, F. Papadopoulou, A. Margellou, D. Petrakis, I. Konstantinou, *Catalysts* **2022**, *12*, 187.
[167] S. Saalinraj, K. C. Ajithprasad, *Mater. Today Proc* **2017**, *4*, 4372.
[168] H. Wang, Y. Wu, J. Zhang, G. Li, H. Huang, X. Zhang, Q. Jiang, *Mater. Lett.* **2015**, *160*, 537.
[169] G. M. Galvani, C. A. Zito, T. M. Perfecto, J. O. D. Malafatti, E. C. Paris, D. P. Volanti, *Mater. Chem. Phys.* **2022**, *290*, 126591.
[170] S. K. Hwang, S.-M. Kang, M. Rethinasabapathy, C. Roh, Y. S. Huh, *Chem. Eng. J.* **2020**, *397*, 125428.

[171] D. Wang, Y. Xu, D. Xiao, Q. Qiao, P. Yin, Z. Yang, J. Li, W. Winchester, Z. Wang, T. Hayat, *J. Hazard. Mater.* **2019**, *371*, 83.
[172] D. Wang, Y. Xu, L. Yang, F. Wang, A. M. Asiri, K. A. Alamry, *J. Mol. Liq.* **2018**, *258*, 327.
[173] X. Liu, Y. Xu, R. Jin, P. Yin, L. Sun, T. Liang, S. Gao, *J. Mol. Liq.* **2014**, *200*, 311.
[174] X. Liu, J. Li, X. Wang, C. Chen, X. Wang, *J. Nucl. Mater.* **2015**, *466*, 56.
[175] S. Yang, M. Hua, L. Shen, X. Han, M. Xu, L. Kuang, D. Hua, *J. Hazard. Mater.* **2018**, *354*, 191.
[176] S. D. Negedu, R. Tromer, C. C. Gowda, C. F. Woellner, F. E. Olu, A. K. Roy, P. Pandey, D. S. Galvao, P. M. Ajayan, P. Kumbhakar, C. S. Tiwary, *Nanoscale* **2022**, *14*, 7788.
[177] G. V. Naik, V. M. Shalaev, A. Boltasseva, *Adv. Mater.* **2013**, *25*, 3264.
[178] J. Chen, P. Albella, Z. Pirzadeh, P. Alonso-González, F. Huth, S. Bonetti, V. Bonanni, J. Åkerman, J. Nogués, P. Vavassori, A. Dmitriev, J. Aizpurua, R. Hillenbrand, *Small* **2011**, *7*, 2341.
[179] M. Jung, Y.-W. Choi, *Mater. Lett.* **2017**, *204*, 49.
[180] B. Li, T. Xing, M. Zhong, L. Huang, N. Lei, J. Zhang, J. Li, Z. Wei, *Nat. Commun.* **2017**, *8*, 1958.
[181] L. M. Martinez, J. A. Delgado, C. L. Saiz, A. Cosio, Y. Wu, D. Villagrán, K. Gandha, C. Karthik, I. C. Nlebedim, S. R. Singamaneni, *J. Appl. Phys.* **2018**, *124*, 153903.
[182] B. Xia, Y. Yang, J. Ma, K. Tao, D. Gao, *Appl. Phys. Express* **2017**, *10*, 093002.
[183] S. Fu, K. Kang, K. Shayan, A. Yoshimura, S. Dadras, X. Wang, L. Zhang, S. Chen, N. Liu, A. Jindal, X. Li, A. N. Pasupathy, A. N. Vamivakas, V. Meunier, S. Strauf, E.-H. Yang, *Nat. Commun.* **2020**, *11*, 2034.
[184] S. Y. Wang, T. S. Ko, C. C. Huang, D. Y. Lin, Y. S. Huang, *Jpn. J. Appl. Phys.* **2014**, *53*, 04EH07.
[185] K. Kang, S. Fu, K. Shayan, Y. Anthony, S. Dadras, X. Yuzan, F. Kazunori, M. Terrones, W. Zhang, S. Strauf, V. Meunier, A. N. Vamivakas, E.-H. Yang, *Nanotechnology* **2021**, *32*, 095708.
[186] L.-Y. Hu, L.-F. Yu, H. Yang, X. Xu, F. Wang, X.-H. Xu, *Rare Met.* **2021**, *40*, 2501.
[187] I. Nazir, R. Tomar, R. Poolla, Z. U. Haq, J. H. Malik, M. B. Zaman, *Mater. Res. Express* **2019**, *6*, 115032.
[188] S. Sun, Y. Yu, S. Sun, Q. Wang, T. Chen, J. Chen, Y. Zhang, W. Cui, *J. Supercond. Nov. Magn.* **2021**, *34*, 1477.
[189] Y. C. Cheng, Z. Y. Zhu, W. B. Mi, Z. B. Guo, U. Schwingenschlögl, *Phys. Rev. B* **2013**, *87*, 100401(R).
[190] B. Li, L. Huang, M. Zhong, N. Huo, Y. Li, S. Yang, C. Fan, J. Yang, W. Hu, Z. Wei, J. Li, *ACS Nano* **2015**, *9*, 1257.
[191] L. Xia, K. Pan, H. Wu, F. Wang, Y. Liu, Y. Xu, Z. Dong, B. Wei, S. Wei, *ACS Appl. Mater. Interfaces* **2022**, *14*, 22030.
[192] Z. Xiang, Z. Zhang, X. Xu, Q. Zhang, Q. Wang, C. Yuan, *Phys. Chem. Chem. Phys.* **2015**, *17*, 15822.
[193] Z. Hou, C. Yang, W. Zhang, C. Lu, F. Zhang, X. Zhuang, *RSC Adv.* **2016**, *6*, 82341.
[194] L. Shao, Y. Liu, L. Wang, X. Xia, X. Shen, *Appl. Surf. Sci.* **2020**, *502*, 143895.
[195] H. Wang, S. Sun, M. Ding, J. Cui, S. Liang, *Chemosphere* **2023**, *329*, 138643.
[196] S. R. Kadam, R. Bar-Ziv, M. Bar-Sadan, *New J. Chem.* **2022**, *46*, 20102.
[197] Y. Chen, F. Liu, F. Qiu, C. Lu, J. Kang, D. Zhao, S. Han, X. Zhuang, *Polymers* **2018**, *10*, 1339.
[198] Y. Han, M. Wang, Y. Dong, Z. Cheng, X. Li, X. Yan, Y. Zhang, J. Zhang, *J. Colloid Interface Sci.* **2023**, *644*, 42.
[199] H. Wei, J. Si, L. Zeng, S. Lyu, Z. Zhang, Y. Suo, Y. Hou, *Chin. Chem. Lett.* **2023**, *34*, 107144.
[200] X. Wang, Z. Wang, Y. Li, J. Wang, G. Zhang, *Appl. Catal. B Environ.* **2022**, *319*, 121895.
[201] D. Praveen Kumar, A. P. Rangappa, S. Kim, E. Kim, K. A. J. Reddy, M. Gopannagari, P. Bhavani, D. A Reddy, T. K. Kim, *Int. J. Hydrogen Energy* **2022**, *47*, 40218.
[202] A. Khampunbut, S. Kheawhom, W. Limphirat, P. Pattananuwat, *Electrochim. Acta* **2023**, *443*, 141979.
[203] A. Azor, M. L. Ruiz-Gonzalez, F. Gonell, C. Laberty-Robert, M. Parras, C. Sanchez, D. Portehault, J. M. González-Calbet, *Chem. Mater.* **2018**, *30*, 4986.
[204] T. L. Makarova, K.-H. Han, P. Esquinazi, R. R. Da Silva, Y. Kopelevich, I. B. Zakharova, B. Sundqvist, *Carbon* **2003**, *41*, 1575.
[205] P. Esquinazi, A. Setzer, R. Höhne, C. Semmelhack, Y. Kopelevich, D. Spemann, T. Butz, B. Kohlstrunk, M. Lösche, *Phys. Rev. B* **2002**, *66*, 024429.
[206] Y. Kopelevich, P. Esquinazi, *J. Low Temp. Phys.* **2007**, *146*, 629.
[207] T. Hotta, *Rep. Prog. Phys.* **2006**, *69*, 2061.
[208] R. Zhang, C. Lane, B. Singh, J. Nokelainen, B. Barbiellini, R. S. Markiewicz, A. Bansil, J. Sun, *Commun. Phys.* **2021**, *4*, 118.
[209] M. Pérez, J. Elías, M. Sosa, M. Vallejo, *Eur. J. Phys.* **2022**, *43*, 045401.
[210] M. Koshino, T. Ando, *Phys. Rev. B* **2007**, *75*, 235333.
[211] M. Sepioni, R. R. Nair, S. Rablen, J. Narayanan, F. Tuna, R. Winpenny, A. K. Geim, I. V. Grigorieva, *Phys. Rev. Lett.* **2010**, *105*, 207205.
[212] X. Li, J. Yang, *Natl. Sci. Rev.* **2016**, *3*, 365.
[213] Y. Wang, Y. Huang, Y. Song, X. Zhang, Y. Ma, J. Liang, Y. Chen, *Nano Lett.* **2009**, *9*, 220.
[214] Z. J. Yue, D. H. Seo, K. Ostrikov, X. L. Wang, *Appl. Phys. Lett.* **2014**, *104*, 092417.
[215] O. V. Yazyev, L. Helm, *Phys. Rev. B* **2007**, *75*, 125408.
[216] D. Lee, J. Seo, X. Zhu, J. M. Cole, H. Su, *Appl. Phys. Lett.* **2015**, *106*, 172402.
[217] A. Sinha, A. Ali, A. D. Thakur, *Mater. Today Proc.* **2021**, *46*, 6230.
[218] R. Strzelczyk, M. A. Augustyniak-Jablokow, R. Fedaruk, L. Majchrzycki, J. Zwolinska, O. Kazakova, *J. Magn. Magn. Mater.* **2022**, *544*, 168686.
[219] Q. Feng, N. Tang, F. Liu, Q. Cao, W. Zheng, W. Ren, X. Wan, Y. Du, *ACS Nano* **2013**, *7*, 6729.
[220] Z. Qiao, S. A. Yang, W. Feng, W.-K. Tse, J. Ding, Y. Yao, J. Wang, Q. Niu, *Phys. Rev. B* **2010**, *82*, 161414(R).
[221] J. B. S. Mendes, O. Alves Santos, T. Chagas, R. Magalhães-Paniago, T. J. A. Mori, J. Holanda, L. M. Meireles, R. G. Lacerda, A. Azevedo, S. M. Rezende, *Phys. Rev. B* **2019**, *99*, 214446.
[222] T. Uchihashi, *Supercond. Sci. Technol.* **2017**, *30*, 013002.
[223] M. Mogi, K. Yasuda, R. Fujimura, R. Yoshimi, N. Ogawa, A. Tsukazaki, M. Kawamura, K. S. Takahashi, M. Kawasaki, Y. Tokura, *Nat. Commun.* **2021**, *12*, 1404.
[224] T. Abtew, B.-C. Shih, S. Banerjee, P. Zhang, *Nanoscale* **2013**, *5*, 1902.
[225] G. Song, M. Ranjbar, D. R. Daughton, R. A. Kiehl, *Nano Lett.* **2019**, *19*, 7112.
[226] A. N. Yadav, A. K. Singh, P. Kumar, K. Singh, *Nanoscale Res. Lett.* **2020**, *15*, 166.
[227] J. C. Leutenantsmeyer, A. A. Kaverzin, M. Wojtaszek, B. J. Van Wees, *2D Mater.* **2017**, *4*, 014001.
[228] O. Céspedes, M. S. Ferreira, S. Sanvito, M. Kociak, J. M. D. Coey, *J. Phys. Condens. Matter* **2004**, *16*, L155.
[229] H.-C. Mertins, S. Valencia, W. Gudat, P. M. Oppeneer, O. Zaharko, H. Grimmer, *Europhys. Lett.* **2004**, *66*, 743.
[230] P. O. Lehtinen, A. S. Foster, A. Ayuela, A. Krasheninnikov, K. Nordlund, R. M. Nieminen, *Phys. Rev. Lett.* **2003**, *91*, 017202.
[231] M. Weser, Y. Rehder, K. Horn, M. Sicot, M. Fonin, A. B. Preobrajenski, E. N. Voloshina, E. Goering, Y.. S. Dedkov, *Appl. Phys. Lett.* **2010**, *96*, 012504.
[232] P. Hota, A. J. Akhtar, S. Bhattacharya, M. Miah, S. K. Saha, *Appl. Phys. Lett.* **2017**, *111*, 042402.
[233] W. Hu, C. Wang, H. Tan, H. Duan, G. Li, N. Li, Q. Ji, Y. Lu, Y. Wang, Z. Sun, F. Hu, W. Yan, *Nat. Commun.* **2021**, *12*, 1854.

[234] P. Blonski, J. Tucek, Z. Sofer, V. Mazánek, M. Petr, M. Pumera, M. Otyepka, R. Zboril, *J. Am. Chem. Soc.* **2017**, *139*, 3171.
[235] H. Verma, D. Seifu, S. P. Karna, H. Hong, M. S. Seehra, *AIP Adv.* **2018**, *8*, 025119.
[236] X. Liu, C. Z. Wang, M. Hupalo, W. C. Lu, M. C. Tringides, Y. X. Yao, K. M. Ho, *Phys. Chem. Chem. Phys.* **2012**, *14*, 9157.
[237] S. N. Panda, S. Majumder, S. Choudhury, A. Bhattacharya, S. Sinha, A. Barman, *Nanoscale* **2021**, *13*, 13709.
[238] T. K. Chau, S. J. Hong, H. Kang, D. Suh, *npj Quantum Mater.* **2022**, *7*, 27.
[239] W. Zhang, L. Zhang, P. K. J. Wong, J. Yuan, G. Vinai, P. Torelli, G. Van Der Laan, Y. P. Feng, A. T. S. Wee, *ACS Nano* **2019**, *13*, 8997.
[240] G. Vinai, C. Bigi, A. Rajan, M. D. Watson, T.-L. Lee, F. Mazzola, S. Modesti, S. Barua, M. Ciomaga Hatnean, G. Balakrishnan, P. D. C. King, P. Torelli, G. Rossi, G. Panaccione, *Phys. Rev. B* **2020**, *101*, 035404.
[241] W. Jie, Z. Yang, F. Zhang, G. Bai, C. W. Leung, J. Hao, *ACS Nano* **2017**, *11*, 6950.
[242] D. Odkhuu, T. Tsevelmaa, P. Taivansaikhan, N. Park, S. C. Hong, S. H. Rhim, *Phys. Rev. B* **2019**, *99*, 014419.
[243] J. Rastikian, S. Suffit, C. Barraud, A. Bellec, V. Repain, Y. Roussigné, M. Belmeguenai, S. Farhat, L. Le Laurent, C. Barreteau, S. M. Chérif, *Phys. Rev. Mater.* **2021**, *5*, 014004.
[244] S. F. A. Kettle, in *Physical Inorganic Chemistry*, Springer, Berlin, Heidelberg, Germany **1996**, p. 238.
[245] H. You, N. Ding, J. Chen, X. Yao, S. Dong, *ACS Appl. Electron. Mater.* **2022**, *4*, 3168.
[246] K. Sheng, H.-K. Yuan, Z.-Y. Wang, *Phys. Chem. Chem. Phys.* **2022**, *24*, 3865.
[247] B. Wang, X. Zhang, Y. Zhang, S. Yuan, Y. Guo, S. Dong, J. Wang, *Mater. Horiz.* **2020**, *7*, 1623.
[248] S. Periyasamy, J. Vinoth Kumar, S.-M. Chen, Y. Annamalai, R. Karthik, N. Erumaipatty Rajagounder, *ACS Appl. Mater. Interfaces* **2019**, *11*, 37172.
[249] P. Sundaresan, A. Krishnapandi, S.-M. Chen, *J. Taiwan Inst. Chem. Eng.* **2019**, *96*, 509.
[250] P. Sundaresan, P. Gnanaprakasam, S.-M. Chen, R. V. Mangalaraja, W. Lei, Q. Hao, *Ultrason. Sonochem.* **2019**, *58*, 104647.
[251] I. Cieslik, T. Bolek, M. J. Wozniak, A. Majchrowski, S. Hirano, A. Budzianowski, *Appl. Surf. Sci.* **2018**, *446*, 139.
[252] A. M. Tokmachev, D. V. Averyanov, A. N. Taldenkov, O. E. Parfenov, I. A. Karateev, I. S. Sokolov, V. G. Storchak, *Mater. Horiz.* **2019**, *6*, 1488.
[253] I. S. Sokolov, D. V. Averyanov, F. Wilhelm, A. Rogalev, O. E. Parfenov, A. N. Taldenkov, I. A. Karateev, A. M. Tokmachev, V. G. Storchak, *Nano Res.* **2022**, *15*, 408.
[254] I. S. Sokolov, D. V. Averyanov, O. E. Parfenov, A. N. Taldenkov, I. A. Karateev, A. M. Tokmachev, V. G. Storchak, *J. Alloys Compd.* **2021**, *884*, 161078.
[255] I. S. Sokolov, D. V. Averyanov, O. E. Parfenov, I. A. Karateev, A. N. Taldenkov, A. M. Tokmachev, V. G. Storchak, *Mater. Horiz.* **2020**, *7*, 1372.
[256] A. M. Tokmachev, D. V. Averyanov, O. E. Parfenov, A. N. Taldenkov, I. A. Karateev, I. S. Sokolov, O. A. Kondratev, V. G. Storchak, *Nat. Commun.* **2018**, *9*, 1672.
[257] D. V. Averyanov, I. S. Sokolov, A. N. Taldenkov, O. E. Parfenov, A. M. Tokmachev, V. G. Storchak, *Nanoscale* **2022**, *14*, 12377.
[258] D. V. Averyanov, I. S. Sokolov, A. N. Taldenkov, O. E. Parfenov, A. M. Tokmachev, V. G. Storchak, *Nano Res.* **2023**, *16*, 1500.
[259] S. Bobev, E. D. Bauer, J. D. Thompson, J. L. Sarrao, G. J. Miller, B. Eck, R. Dronskowski, *J. Solid State Chem.* **2004**, *177*, 3545.
[260] H. Tan, G. Shan, G. Pacchioni, *Phys. Chem. Chem. Phys.* **2021**, *23*, 25500.
[261] H. Li, H. Zhao, C. Li, B. Li, B. Tao, S. Gu, G. Wang, H. Chang, *Appl. Surf. Sci.* **2022**, *600*, 154105.
[262] D. Marani, L. P. R. Moraes, F. Gualandris, S. Sanna, D. Z. De Florio, V. Esposito, F. C. Fonseca, *CrystEngComm* **2018**, *20*, 1405.
[263] D. H. Kang, S. R. Dugasani, H.-Y. Park, J. Shim, B. Gnapareddy, J. Jeon, S. Lee, Y. Roh, S. H. Park, J.-H. Park, *Sci. Rep.* **2016**, *6*, 20333.
[264] X. J. Zhang, X. C. Wang, W. B. Mi, *Solid State Commun.* **2015**, *212*, 35.
[265] S. Rafiq, S. Awan, R.-K. Zheng, Z. Wen, M. Rani, D. Akinwande, S. Rizwan, *J. Magn. Magn. Mater.* **2020**, *497*, 165954.
[266] J. González, P. Sevilla, G. Gabarró-Riera, J. Jover, J. Echeverría, S. Fuertes, A. Arauzo, E. Bartolomé, E. C. Sañudo, *Angew. Chem., Int. Ed.* **2021**, *60*, 12001.
[267] Y. Cai, Y. Huang, W. Jia, Y. Zhang, X. Wang, Y. Guo, D. Jia, W. Pang, Z. Guo, L. Wang, *J. Mater. Chem. A* **2016**, *4*, 17782.
[268] Y.-L. Chen, C.-H. Shen, C.-W. Huang, C.-W. Kung, *Mol. Syst. Des. Eng.* **2022**, *8*, 330.
[269] T. Wu, J. Gao, J. Wang, S. Wang, Y. Bai, Y. Li, K. Li, X. Zhang, *Spectrochim. Acta – Part A Mol. Biomol. Spectrosc.* **2012**, *86*, 1.
[270] P. Feng, B. Shao, X. Wang, X. Yang, *Eur. J. Inorg. Chem.* **2017**, *2017*, 4861.
[271] Y. Huang, Y. Zhao, Y. Liu, R. Ye, L. Chen, G. Bai, S. Xu, *Chem. Eng. J.* **2021**, *411*, 128610.
[272] H. Zhao, G. Zhang, B. Yan, B. Ning, C. Wang, Y. Zhao, X. Shi, *Research* **2022**, *2022*, 9840970.
[273] P. Chen, X. Xu, D. Li, Z. Li, H. Wang, L. Pi, X. Zhou, T. Zhai, *Adv. Opt. Mater.* **2022**, *10*, 2102102.
[274] K. Li, T.-H. Chang, Q. Xie, Y. Cheng, H. Yang, J. Chen, P.-Y. Chen, *Adv. Electron. Mater.* **2019**, *5*, 1900040.
[275] X. Chen, Z.-Z. Lin, *J. Nanopart. Res.* **2018**, *20*, 129.
[276] S. W. Lee, S. K. Park, B. K. Min, J.-G. Kang, Y. Sohn, *Appl. Surf. Sci.* **2014**, *307*, 736.
[277] J. V. Kumar, B. Mutharani, S.-M. Chen, R. Rajakumaran, E. R. Nagarajan, *New J. Chem.* **2020**, *44*, 4285.
[278] E. Vivek, A. Arulraj, M. Khalid, I. V. Potheher, *J. Alloys Compd.* **2022**, *908*, 164541.
[279] X. Y. Wang, S. Y. Xiao, Z. W. Jiang, S. J. Zhen, C. Z. Huang, Q. Q. Liu, Y. F. Li, *Talanta* **2021**, *234*, 122625.
[280] R. Sun, D. Zhou, P. Lu, X. Jing, X. Zhuang, S. Liu, Y. Wang, X. Bai, W. Xu, H. Song, *Nano Energy* **2022**, *93*, 106815.
[281] X. Zheng, J. Zhong, M.-Y. Dong, Y. Wen, A.-Z. Chen, *RSC Adv.* **2022**, *12*, 34318.
[282] Z. Yang, M. Xiang, Z. Wu, W. Fan, J. Hui, C. Yu, S. Dong, H. Qin, *Mater. Today Chem.* **2022**, *26*, 101147.
[283] D. B. Bailmare, P. Tripathi, A. D. Deshmukh, B. K. Gupta, *Sci. Rep.* **2022**, *12*, 3084.
[284] A. Umar, R. Kumar, M. S. Akhtar, G. Kumar, S. H. Kim, *J. Colloid Interf. Sci.* **2015**, *454*, 61.
[285] S. Han, Y. Xie, Q. Xin, J. Lv, Y. Zhang, F. Wang, X. Fu, H. Li, L. Zhao, H. Ye, Y. Zhang, *J. Memb. Sci.* **2023**, *666*, 121126.
[286] G. Li, H. Zhang, Y. Li, S. Yin, X. Kan, W. Wei, H. Du, B. Ge, C. An, M. Tian, F. Yan, S. Yang, T. Zhai, L. Li, *Nano Res.* **2022**, *15*, 5469.
[287] R. Wang, Z. Wang, L. Zhang, Q. Wang, Z. Zhao, W. Huang, J. Shi, *ACS Energy Lett.* **2022**, *7*, 1980.

Anastasios Papavasileiou obtained his B.Sc. (2018) and M.Sc. (2020) in chemistry from the University of Ioannina in Greece, specializing in electrochemical sensing. Subsequently, as a research intern he visited Masaryk University in Brno, Czech Republic through the European mobility program, Erasmus+. Currently, he is a doctoral student at the University of Chemistry and Technology in Prague, accompanied by two scholarships. His main research interest lies in applied electrochemistry utilizing advanced technologies and novel materials, with a keen interest in 2D materials, magnetism, and 3D printing technology.

Melita Menelaou received her Diploma in Chemical Engineering (2004) and PhD degree (2009) from the Aristotle University of Thessaloniki (Greece). Menelaou was a member of respected research groups in Asia (Japan – Advanced Institute of Materials Research) and Europe (Czechia – Central European Institute of Technology-Brno University of Technology; Spain – University of Barcelona; Greece – School of Chemical Engineering/School of Chemistry, Aristotle University of Thessaloniki). Currently, she is working in the Department of Chemical Engineering at Cyprus University of Technology. Her work focuses on the synthesis, characterization and application of a wide range of materials including nanomaterials with technological and biomedical applications.

Kalyan Jyoti Sarkar received his Ph.D. degree from the Indian Institute of Technology Kharagpur, India in 2020. Currently he is working as a postdoctoral researcher at Sofer's Group, UCT Prague. Prior to joining the Sofer's Group in January 2022, he was a SERB National Postdoctoral Fellow at Indian Institute of Science Bangalore. He has also worked as a research associate-I in QuEST-DST project for six months at Indian Institute of Science Education and Research, Thiruvananthapuram (IISER TVM). His research focus is fabrication and characterization of 2D material-based devices for optoelectronics.

Zdenek Sofer is tenured professor at the University of Chemistry and Technology Prague since 2019. He received his PhD also at University of Chemistry and Technology Prague, Czech Republic, in 2008. During his PhD he spent one year in Forschungszentrum Julich (Peter Grünberg Institute, Germany) and also one postdoctoral stay at University Duisburg-Essen, Germany. Research interests of prof. Sofer concerning on 2D materials including graphene, layered chalcogenides and other 2D materials, its crystal growth, chemical modifications and derivatization. His research covers various applications of 2D materials including energy storage and conversion, electronic, catalysis and sensing devices. He is an associated editor of FlatChem journal. He has published over 600 articles, which received > 27 000 citations (h-index of 83).

Lakshminarayana Polavarapu is the principal investigator of the Materials chemistry and physics research group at the Centro De Investigaciones Biomédicas (CINBIO), University of Vigo. He obtained an MSc in Chemistry from the University of Hyderabad (India) and PhD from the National University of Singapore. After being a postdoctoral fellow at CIC biomaGUNE and University of Vigo in Spain, he joined the Chair for Photonics and Optoelectronics at the Ludwig-Maximilians-University of Munich (Germany) as an Alexander von Humboldt postdoctoral fellow and later continued as a junior group leader until May 2020. His research interests include shape-controlled synthesis and self-assembly of metal and semiconductor nanocrystals for exploring their optical properties and optoelectronic applications.

Stefanos Mourdikoudis is a chemical engineer who obtained his PhD degree in the Department of Physics, Aristotle University of Thessaloniki in Greece in 2009. Apart from his native country, he also worked in post-doctoral projects in France, Spain, the UK and the Czech Republic. Currently he is working at the Flemish Institute for Technological Research (VITO) in Belgium. His research interests include the colloidal and electrochemical synthesis and characterization of nanoscale particles of diverse compositions. Depending on their type, these particles are employed in a range of applications such as catalysis, electrocatalysis, environment and "bio"-fields.